

**APPLICATION AND DEVELOPMENT OF MICROSTRUCTURED
SOLID-STATE NEUTRON DETECTORS**

By

Adam D. Weltz

A Thesis Submitted to the Graduate
Faculty of Rensselaer Polytechnic Institute
in Partial Fulfillment of the
Requirements for the Degree of
DOCTOR OF PHILOSOPHY

Major Subject: NUCLEAR ENGINEERING AND SCIENCE

Approved by the Examining Committee:

Yaron Danon, Thesis Advisor

Wei Ji, Member

George Xu, Member

Ishwara Bhat, Member

Peter Caracappa, Member

Rensselaer Polytechnic Institute
Troy, New York

July 2017
(For Graduation August 2017)

© Copyright 2017

by

Adam D. Weltz

All Rights Reserved

CONTENTS

LIST OF TABLES	vi
LIST OF FIGURES	vii
ACKNOWLEDGMENT	xiv
ABSTRACT	xv
1. Introduction	1
1.1 Solid-State Neutron Detectors (SSNDs)	2
1.1.1 Thermal Neutron Detection with SSNDs	2
1.1.2 Fast Neutron Detection with SSNDs	4
1.1.3 Planar SSNDs	5
1.1.4 Microstructured SSNDs	7
1.1.5 Homogeneous SSNDs	9
2. Solid-State Detector Fabrication at RPI	11
2.1 Honeycomb SSND Fabrication	11
2.2 Trench Microstructure SSND Fabrication	14
3. Simulation and Optimization of SSNDs	23
3.1 Comparison and Optimization of Microstructured SSND Designs	25
3.1.1 Recommendations for the Future Development of SSNDs	34
3.2 Predicting Pulse Height Spectra Using MCNP	36
3.2.1 Simulating the Honeycomb SSND Pulse Height Spectra	37
3.2.2 Simulating the Trench SSND Pulse Height Spectra	46
3.3 Microstructure Customization for Versatile Detection Systems	52
3.4 Homogeneous SSND Simulation	53
4. Solid-State Detector Testing at RPI	56
4.1 Neutron Detection with Solid-State Devices	56
4.2 Development of Low-Noise Preamplifiers for RPI's SSNDs	57
4.3 Electronic Noise and the Low-Level Discriminator (LLD)	62

4.4	Determining the Detector Efficiency	63
4.4.1	Thermal Neutron Flux Measurements.....	67
4.4.1.1	Lithium Glass Scintillator	67
4.4.1.2	Gold Activation Foil	70
4.4.1.3	Indium Activation Foil.....	73
4.4.1.4	Thermal Neutron Flux Comparisons.....	76
4.5	Intrinsic Thermal Neutron Efficiency Measurements	79
4.6	Gamma Discrimination	82
4.7	Detector Scalability	83
5.	Applications of SSNDs.....	86
5.1	A Modular Directional and Spectral Neutron Detection System (DSNDS)	86
5.1.1	DSNDS Design Optimization	87
5.1.2	Experiments with Different Neutron Spectra.....	89
5.1.3	Determining the Source Spectrum	90
5.1.4	Determination of the Source Angle and Resolution.....	98
5.1.5	DSNDS Conclusions.....	102
5.2	A Real-Time Personal Neutron Dosimeter	102
5.2.1	Dosimeter Simulation and Design.....	104
5.2.2	Real-Time Dosimeter Conclusions and Future Work	109
5.3	Pulsed Neutron Detectors.....	109
6.	Conclusions.....	112
	REFERENCES.....	114
	Appendix A: Contour plots used to optimize the geometry of microstructured devices with various design and neutron-converting materials.	120
	Appendix B: Examples of MCNP6 inputs used to determine the optimal device microstructure corresponding to various neutron converting materials, discrimination levels (LLDs), and device depths.....	126

Appendix C: Example of an MCNP6 input used to simulate the pulse height spectrum of a 45 μm -deep honeycomb device ($D_H=3 \mu\text{m}$, $W_w=1 \mu\text{m}$) with 100 evenly-spaced energy bins..... 132

Appendix D: Example of an MCNP6 input used to simulate the pulse height spectrum of a 70 μm -deep trench device ($W_T=5 \mu\text{m}$, $W_w=3 \mu\text{m}$) with 100 evenly-spaced energy bins. 134

Appendix E: Individual MCNP inputs and factors used to create the simulated pulse height spectrum in Figure 3.12. 136

LIST OF TABLES

Table 2.1: Side-by-side comparison of the fabrication processes used to produce the aforementioned honeycomb and trench microstructured SSNDs.....	22
Table 3.1: Optimal microstructure dimensions corresponding to an isotropic thermal neutron source for various SSND designs and their associated thermal neutron efficiency ($E_n=0.0253$ eV) simulated with LLDs of 200 and 500 keV using MCNP6.1.	33
Table 4.1: Gamma energy and branching ratios associated with the decay of ^{116m}In according to ENDF/B-VII.1.....	74
Table 4.2: Calculated thermal neutron flux corresponding to the 8-cm position on 9/1/2015.	78
Table 4.3: Results of the intrinsic thermal neutron efficiency measurements performed with two amplifiers.	82
Table 4.4: Relative efficiency associated with scaling the individual 4-cm ² honeycomb devices to larger detection areas.	85
Table 5.1: Three source configurations characterized by the FNF: the fraction of neutrons above 1.0 eV.	92
Table 5.2: Simulated fast neutron factor (FNF) for three source configurations and the associated measured FWHM of the detector system’s normalized response and the internal-to-external detector ratios with and without the Cd decoupler.	94
Table 5.3: DSNDs response to a test neutron source configuration.....	96
Table 5.4: Comparison of Pb-shielded and bare ^{252}Cf source spectra and DSNDs-measured FWHM and Internal-to-External Ratio with the Cd decoupler.	98
Table 5.5: Tabulated results of the normalized, MCNP6.1-simulated internal detector responses used to determine the relative source angle using the linear interpolation of equation 1 and uncertainties corresponding to 3×10^7 emitted neutrons 1.15 m from the DSNDs.	101
Table 5.6. Comparison of the simulated real-time dosimeter response to the actual tallied dose.	108
Table E1: Individual MCNP inputs and factors used to create the simulated pulse height spectrum in Figure 3.12.....	142

LIST OF FIGURES

Figure 1.1: Total reaction cross-section of ^{10}B and ^6Li from ENDF VII.....	3
Figure 1.2: Cross-section for neutron elastic scattering with a hydrogen nucleus from ENDF VII.....	5
Figure 1.3: Diagram of a planar thermal SSND showing the energy deposition of a reaction produced by neutron absorption in a neutron-converting layer [9].	6
Figure 1.4: Diagram of a sandwiched planar SSND showing the energy deposition of a reaction produced by neutron absorption in a ^{10}B neutron-converting layer.....	7
Figure 1.5: Diagram of a fast SSND demonstrating the trajectory of a recoiled proton and scattered neutron caused by a proton recoil reaction in the hydrogenous neutron-converting material [14].....	9
Figure 2.1: Cross-sectional SEM image of a honeycomb device filled with enriched ^{10}B via CVD.	13
Figure 2.2: Zoomed in cross-sectional SEM image of a honeycomb device filled with enriched ^{10}B via CVD.....	13
Figure 2.3: Schematic of a honeycomb structured SSND [13].....	14
Figure 2.4: (Left) Original trench design. (Right) New trench design with increased strength allowing for longer trenches resulting in better nanoparticle filling.....	15
Figure 2.5: Schematic of the RPI-developed, trench microstructured SSND filled with enriched boron nanoparticles.	16
Figure 2.6: Cross-sectional SEM image of the boron nanoparticle-filled trench microstructure SSND with trench widths of $3.5\ \mu\text{m}$ and Si wall widths of $2\ \mu\text{m}$	17
Figure 2.7: Schematic of a boron nanoparticle-filled microstructured trench SSND.....	17
Figure 2.8: Example of an EPD cell used to deposit nanoparticles into the trench microstructures of a SSND.	18
Figure 2.9: SEM imaged of a trench microstructured SSND filled with enriched B_4C nanoparticles via EPD.....	19
Figure 2.10: Large vacuum chamber used for the vacuum-assisted filling of the microstructured trench SSNDs.	20

Figure 2.11: SEM image of a trench microstructured SSND filled with ^{10}B nanoparticles via vacuum-assisted filling. The trenches are 2.5-3.5 μm wide, 65 μm deep, and are etched using TMAH.	20
Figure 2.12: Zoomed in image of a trench microstructured SSND filled with ^{10}B nanoparticles via vacuum-assisted filling with an effective density of $\sim 0.6 \text{ g/cm}^3$	21
Figure 3.1: Top-view schematic of the repeated structures used to simulate the honeycomb microstructured SSNDs with MCNP6.1.	27
Figure 3.2: Top-view schematic of the repeated microstructure used to simulate the trench microstructured SSNDs.	27
Figure 3.3: Top-view schematic of the repeated microstructure used to simulate the parallelogram microstructured SSNDs.	28
Figure 3.4: Contour plot showing the simulated thermal neutron efficiency as a function of the hexagonal diameter and silicon wall thickness of a 45 μm -deep honeycomb device filled via CVD of boron ($\rho=2.35 \text{ g/cm}^3$) and an LLD of 200 keV.	30
Figure 3.5: Contour plot showing the simulated thermal neutron efficiency as a function of the parallelogram width and silicon wall thickness of a 45 μm -deep parallelogram device filled via CVD of B_4C ($\rho=2.52 \text{ g/cm}^3$) and an LLD of 200 keV.	31
Figure 3.6: Contour plot showing the simulated thermal neutron efficiency as a function of the trench width and silicon wall thickness of a 45 μm -deep trench device filled via CVD of BN ($\rho=2.1 \text{ g/cm}^3$) and an LLD of 500 keV.	32
Figure 3.7: Cross-sectional view (left) and top view (right) of an MCNP-simulated honeycomb device used to model the neutron pulse height spectrum.	38
Figure 3.8: Cross-sectional view (left) and top view (right) of a honeycomb device taken with a microscope.	39
Figure 3.9: Experimentally-collected neutron pulse height spectrum of a honeycomb device. The measurement was performed with a moderated ^{252}Cf source using a custom preamplifier.	40
Figure 3.10: MCNP-simulated pulse height spectra for enriched ^{10}B -filled honeycomb devices with variable hexagonal sizes and a fill factor of 100%.	41
Figure 3.11: MCNP-simulated pulse height spectra for enriched ^{10}B -filled honeycomb devices with variable hexagonal sizes and a fill factor of 55%.	42

Figure 3.12: Comparison of an experimentally collected and an aggregate, simulated neutron pulse height spectrum of a honeycomb SSND demonstrating good agreement.	44
Figure 3.13: Cross-sectional view (left) and top view (right) of the simulated honeycomb device using tapered cylinders in order to predict the shape of a honeycomb device pulse height spectrum.	45
Figure 3.14: Comparison of an experimentally collected honeycomb neutron pulse height spectrum and the MCNP-simulated pulse height spectrum of a single SSND with tapered cylinders in a hexagonal lattice.	46
Figure 3.15: Labeled experimental pulse height spectra collected with the trench microstructured SSNDs T52 (Area=2.5 x 2.5 mm ²). This measurement was collected with zero bias, a custom preamplifier, an ORTEC shaping amplifier with a gain of 8 and an integration time of 12 μs.	47
Figure 3.16: MCNP-simulated thermal neutron pulse height spectra corresponding to a trench microstructured device with variable trench thicknesses (4-6 μm), a pitch of 8 μm, and a nanoparticle density of 0.6 g/cm ³ .	48
Figure 3.17: MCNP-simulated thermal neutron pulse height spectra corresponding to a trench microstructured device with variable trench thicknesses (4-6 μm), a pitch of 8 μm, and a nanoparticle density of 0.8 g/cm ³ .	49
Figure 3.18: Comparison of an experimentally collected pulse height spectrum of trench device T52 and an MCNP-simulated neutron pulse height spectrum created from of an aggregate of simulations using least squares regression.	50
Figure 3.19: Comparison of an experimentally collected neutron pulse height spectrum (device T52) and the MCNP-simulated pulse height spectrum of a single device with tapered trenches.	51
Figure 3.20: Simulated pulse height tally of an hBN slab with a thickness of 10 μm and ideal charge collection.	54
Figure 3.21: Simulated pulse height tally of an hBN slab with a thickness of 10 μm broadened by a 1 MeV Gaussian.	55
Figure 4.1: Capacitance vs. bias voltage for a 6.25 mm ² honeycomb SSND developed at RPI.	58
Figure 4.2: Schematic of a 1-cm ² SSND mounted on a copper substrate.	59

Figure 4.3: Leakage current as a function of bias voltage for a 1-cm ² honeycomb SSND.	59
Figure 4.4: Photograph of a 4-cm ² honeycomb SSND.	60
Figure 4.5: Diagram of a 4-cm ² honeycomb detector comprised of individual 6.25 mm ² devices.....	60
Figure 4.6: Top view of the RPI custom electronics, including one preamplifier, one shaping amplifier, and one discriminator built on printed circuit boards.	61
Figure 4.7: Side view of the housing for the RPI custom electronics showing the 8 BNC inputs.....	62
Figure 4.8: Background and neutron response of a SSND with an LLD set and labeled corresponding to a SNR of 1000.....	63
Figure 4.9: Diagram of the HDPE housing used to both store the ²⁵² Cf source (center hole) and provide a moderated neutron flux when placed in the exposure hole [14].	64
Figure 4.10: MCNP simulation of the neutron spectrum at the exposure face of the moderated ²⁵² Cf neutron source in RPI's Calibrated Neutron Laboratory.	65
Figure 4.11: Total cross-section for ¹¹³ Cd according to ENDF-VII demonstrating the precipitous drop off at 0.4-0.5 eV.....	66
Figure 4.12: (Left) Li glass scintillator surrounded by enriched B ₄ C blocks. (Right) Experimental setup used to measure the thermal neutron flux at the 8-cm position using the Li glass detector.	68
Figure 4.13: Pulse height spectra collected with the bare and Cd-covered Li glass scintillator for 300 seconds at the 8-cm position.	69
Figure 4.14: Total cross-section for ¹⁹⁷ Au according to ENDF-VII.....	71
Figure 4.15: Au foil activated at 8-cm position measured with NaI(Tl) scintillator at a distance of 5 cm.	72
Figure 4.16: LaBr pulse height spectrum collected with an activated In foil and background.....	75
Figure 4.17: Gamma spectroscopy of the 2.49g indium foil activated at the 8-cm position collected with a LaBr scintillator for 5,000 seconds 3.5 cm from the foil.	76
Figure 4.18: Detector responses (bare, Cd-covered, and background) of the best 1-cm ² honeycomb SSND at the 8-cm ² position.	80

Figure 4.19: Detector responses (bare, Cd-covered, and background) of the best 1-cm ² honeycomb SSND at the 8-cm ² position corresponding to the customized and commercial preamplifiers.	81
Figure 4.20: Response of a 4-cm ² honeycomb device exposed to a calibrated ¹³⁷ Cs source compared to the response to a moderated ²⁵² Cf neutron source and the device background.	83
Figure 4.21: Pulse height spectra for honeycomb SSNDs with surface areas of 4, 8, 12, and 16-cm ² exposed to a moderated ²⁵² Cf neutron source.....	84
Figure 5.1: a) Front view of the system showing the external ring of detectors mounted on 5.08 cm (2”) thick center HDPE disk, b) Top view of the system showing 4 internal and 4 external detectors.	87
Figure 5.2: MCNP-simulated detector responses used to optimize the system’s dimensions. a) was used to determine the internal detector location (r=11.5 cm), b) the cylindrical height (15 cm), and c) the cylindrical radius (15cm).....	88
Figure 5.3: Experimental configuration used to represent laboratory experiments where the ²⁵² Cf source was aligned with the 0° detectors of the DSNDs in one of four different source configurations: bare, moderated (5.08 cm HDPE), lightly moderated (1.27 cm HDPE), or reflected.	89
Figure 5.4: MCNP-simulated neutron flux per source neutron incident on the DSNDs corresponding to three ²⁵² Cf source configurations.	91
Figure 5.5: Experimental and MCNP-simulated distribution of the relative count rates of the internal ring of detectors corresponding to three source spectra.	92
Figure 5.6: Empirical relationship between (a) the measured FWHM and FNF and (b) the measured Internal-to-External ratio and FNF.	94
Figure 5.7: MCNP-simulated neutron flux per source neutron incident on the DSNDs corresponding to the bare source configuration and the test source configuration in which a ²⁵² Cf source was moderated by 0.5” of HDPE.....	95
Figure 5.8: Experimental and simulated distribution of the relative count rates of the internal ring of detectors corresponding to the test source configuration.....	96

Figure 5.9: MCNP-simulated neutron flux per source neutron incident on the DSNDs corresponding to the ^{252}Cf source shielded with 5 cm of Pb, which is compared to the bare ^{252}Cf neutron spectrum.....	97
Figure 5.10: MCNP simulations demonstrating the sensitivity of the DSNDs to a 22.5° shift in the source angle with error bars corresponding to the ^{252}Cf source emitting 3×10^7 neutrons at the 1.15 m position for: a) the bare ^{252}Cf source and b) the ^{252}Cf source moderated by 5 cm of HDPE.....	100
Figure 5.11: The neutron flux-to-dose equivalent conversion factors from ICRP Publications 21 (1973) and ICRP 74 (1996).....	104
Figure 5.12: Top-view diagram of the simulated real-time personal neutron dosimeter using a fast and thermal microstructured SSND.....	105
Figure 5.13. Simulated energy-dependent responses of the two detectors comprising the real-time dosimeter.	106
Figure 5.14. Simulated spectra of three sources used to calibrate the real-time personal neutron dosimeter.....	107
Figure 5.15. Response of the simulated real-time dosimeter compared to the ideal rem response according to ICRP 74.....	108
Figure 5.16: First SiC-Ag SSND used to measure neutrons from high-intensity pulsed neutron sources.	109
Figure 5.17: SiC-Ag detector response to two activation measurements taken with the RPI LINAC at $F=180$ Hz, $I=5$ μA	111
Figure A.1: Contour plot showing the simulated thermal neutron efficiency as a function of the hexagonal diameter and silicon wall thickness of a 45 μm -deep honeycomb device filled via CVD of boron ($\rho=2.35$ g/cm^3) and an LLD of 200 keV (left) and 500 keV (right).	120
Figure A.2: Contour plot showing the simulated thermal neutron efficiency as a function of the hexagonal diameter and silicon wall thickness of a 45 μm -deep honeycomb device with CVD boron carbide ($\rho=2.52$ g/cm^3) and an LLD of 200 keV (left) and 500 keV (right).	120
Figure A.3: Contour plot showing the simulated thermal neutron efficiency as a function of the hexagonal diameter and silicon wall thickness of a 45 μm -deep honeycomb device	

filled via CVD of boron nitride ($\rho=2.1 \text{ g/cm}^3$) and an LLD of 200 keV (left) and 500 keV (right).	121
Figure A.4: Contour plot showing the simulated thermal neutron efficiency as a function of the parallelogram width and silicon wall thickness of a 45 μm -deep parallelogram device filled via CVD of boron ($\rho=2.35 \text{ g/cm}^3$) and an LLD of 200 keV (left) and 500 keV (right).	121
Figure A.5: Contour plot showing the simulated thermal neutron efficiency as a function of the parallelogram width and silicon wall thickness of a 45 μm -deep parallelogram device filled via CVD of B_4C ($\rho=2.52 \text{ g/cm}^3$) and an LLD of 200 keV (left) and 500 keV (right).	122
Figure A.6: Contour plot showing the simulated thermal neutron efficiency as a function of the parallelogram width and silicon wall thickness of a 45 μm -deep parallelogram device filled via CVD of BN ($\rho=2.1 \text{ g/cm}^3$) and an LLD of 200 keV (left) and 500 keV (right).	122
Figure A.7: Contour plot showing the simulated thermal neutron efficiency as a function of the trench width and silicon wall thickness of a 45 μm -deep trench device filled via CVD of boron ($\rho=2.35 \text{ g/cm}^3$) and an LLD of 200 keV (left) and 500 keV (right).	123
Figure A.8: Contour plot showing the simulated thermal neutron efficiency as a function of the trench width and silicon wall thickness of a 45 μm -deep trench device filled via CVD of B_4C ($\rho=2.52 \text{ g/cm}^3$) and an LLD of 200 keV (left) and 500 keV (right).	123
Figure A.9: Contour plot showing the simulated thermal neutron efficiency as a function of the trench width and silicon wall thickness of a 45 μm -deep trench device filled via CVD of BN ($\rho=2.1 \text{ g/cm}^3$) and an LLD of 200 keV (left) and 500 keV (right).	124
Figure A.10: Contour plot showing the simulated thermal neutron efficiency as a function of the trench width and silicon wall thickness of a 70 μm -deep trench device filled with boron nanoparticles ($\rho=0.7 \text{ g/cm}^3$) and an LLD of 200 keV (left) and 500 keV (right).	124
Figure A.11: Contour plot showing the simulated thermal neutron efficiency as a function of the trench width and silicon wall thickness of a 70 μm -deep trench device filled with B_4C nanoparticles ($\rho=0.7 \text{ g/cm}^3$) and an LLD of 200 keV (left) and 500 keV (right). .	125

ACKNOWLEDGMENT

RPI's Mechanical, Aerospace, and Nuclear Engineering (MANE) Department remains supportive of student researchers like myself. Many wonderful and talented people within and outside of the department directly and indirectly helped with this project. First, I would like to express gratitude to Dr. Yaron Danon for his expert guidance and backing. Similarly, Dr. Ishwara Bhat, Dr. George Xu, and Dr. Peter Caracappa provided guidance on this project and beyond. This work would not be possible without Dr. Ishwara Bhat, Dr. Rajendra Dahal, and Dr. James Lu. Fellow students Dr. Jacky Huang, Kawser Ahmed, Jia Woei Wu, and Erik English, who were a pleasure to work with and added significantly to this work. Lastly, I'd like to thank my parents—Jim and Dana Weltz—along with my brother—James Weltz—for their support and encouragement along the way.

This work was funded by The U.S. Department of Homeland Security (DHS) Domestic Nuclear Defense Office (DNDO) in order to develop low-cost solid-state neutron detectors under contracts NSF/ECCS-1348269 and 2013-DN-077-ER001.

ABSTRACT

Neutron detectors are useful for a number of applications, including the identification of nuclear weapons, radiation dosimetry, and nuclear reactor monitoring, among others. Microstructured solid-state neutron detectors (SSNDs) developed at RPI have the potential to reinvent a variety of neutron detection systems due to their compact size, zero bias requirement, competitive thermal neutron detection efficiency (up to 29%), low gamma sensitivity (below the PNNL recommendation of 10^{-6} corresponding to a 10 mR/hr gamma exposure), and scalability to large surface areas with a single preamplifier (<20% loss in relative efficiency from 1 to 16 cm²). These microstructured SSNDs have semiconducting substrate etched with a repeated, three-dimensional microstructure of high aspect ratio holes filled with ¹⁰B. MCNP simulations optimized the dimensions of each microstructure geometry for each detector application, improving the overall performance. This thesis outlines the development of multiple, novel neutron detection applications using microstructured SSNDs developed at RPI. The Directional and Spectral Neutron Detection System (DSNDS) is a modular and portable system that uses rings of microstructured SSNDs embedded in polyethylene in order to gather real-time information about the directionality and spectrum of an unidentified neutron source. This system can be used to identify the presence of diverted special nuclear material (SNM), determine its position, and gather spectral information in real-time. The compact and scalable zero-bias SSNDs allow for customization and modularity of the detector array, which provides design flexibility and enhanced portability. Additionally, a real-time personal neutron dosimeter is a wearable device that uses a combination of fast and thermal microstructured SSNDs in order to determine an individual's neutron dose rate. This system demonstrates that neutron detection systems utilizing microstructured SSNDs are applicable for personal neutron dosimetry. The development of these systems using the compact, zero-bias microstructured SSNDs lays the groundwork for a new generation of neutron detection tools, outlines the challenges and design considerations associated with the implementation of these devices, and demonstrates the value that these detectors bring to the future of neutron detection systems.

1. Introduction

Current neutron detection technology—e.g. boron trifluoride (BF_3) and He^3 proportional counters—is well established and exceedingly efficient but has limitations, so there is interest to develop new neutron detection technology to supplement current capabilities. Neutron detection systems are relied upon for a variety of efforts, including homeland security, nuclear material accountability, and radiological protection. Neutron detection is particularly useful for identifying the presence of special nuclear material (SNM), which is defined as plutonium and uranium enriched in ^{233}U or ^{235}U and is the fissile component of nuclear weapons [1]. Hence, The Department of Homeland Security's (DHS) Domestic Nuclear Defense Office (DNDO) funds an initiative to support the development of new neutron detection technologies, which can be used to develop a network of neutron detection systems with the goal of preventing the diversion of SNM. Currently implemented systems of neutron detectors—such as radiation portal monitors (RPMs), neutron spectrometers and dosimeters (e.g. Bonner spheres), and neutron coincidence counters—rely on gas-filled thermal neutron detectors (i.e. ^3He and BF_3 proportional counters). ^3He proportional counters are the gold standard for thermal neutron detection due to their high thermal neutron efficiency and impeccable gamma insensitivity. A ^3He tube with a diameter of 2.5 cm and fill pressure of 2.5 atmospheres can achieve a thermal neutron detection efficiency above 77% and can operate in a gamma-ray field up to 10 Roentgen (R)/hour [2]. However, the material costs associated with ^3He production are exceedingly high, and there have been periods of time when the limited supply of ^3He was not able to meet the demand for such neutron detectors. Therefore, the development of a new generation of neutron detection applications—including a widespread network of neutron detection systems for homeland security efforts—would be hindered by a reliance on ^3He . BF_3 proportional counters are another proven neutron detection technology; however, the toxicity of the fill gas limits the applicability of these detectors. Additionally, both ^3He and BF_3 proportional counters rely on the use of pressurized gas, which limits their geometry to bulky cylinders. These cylindrical detectors require a rather large bias voltage (2-3 kV, depending on the fill pressure), which limits their portability due to accompanying high voltage power supplies. A central wire delivers the voltage across the tube; vibrations in the wire cause significant

noise in the detector signal, making these detectors microphonic and limiting their viability to stationary applications. For these reasons, solid-state neutron detectors have been developed at RPI and other institutions in order to replace these gas-filled neutron detectors. The goal of this work is to demonstrate the performance and applicability of new microstructured SSNDs for novel applications of neutron detection which improve upon neutron detection systems which utilize gas-filled detectors.

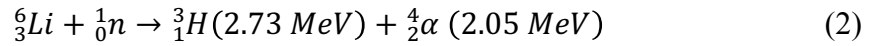
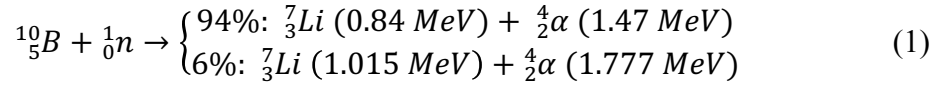
1.1 Solid-State Neutron Detectors (SSNDs)

Solid-state radiation detectors are termed for their use of semiconducting materials. A solid-state device detects a radiation event when ionizing radiation interacts in the semiconductor, producing electron-hole pairs. The movement of these charged particles across the depletion region of the solid-state device to the contacted anode or cathode allows for the detection of individual radiation events via a measurable charge pulse. SSNDs implement a semiconductor substrate; however, neutrons do not directly ionize typical semiconducting substrates (e.g. p- or n-type silicon). Thus, an additional component is required in order to convert incident neutrons into ionizing radiation. SSNDs that employ two distinct components (a neutron-converter and a semiconducting substrate) are called heterogeneous SSNDs. Typically, a neutron-converting material—e.g. ${}^6\text{Li}$, ${}^{10}\text{B}$, or a hydrogenous material—is positioned adjacent to the semiconductor. The neutron-converting layers convert the neutral, non-ionizing neutrons into energetic, charged particles via neutron absorption (for thermal neutron detection) or proton recoil reactions (for fast neutron detection). If the daughter products escape the neutron-converting region with sufficient energy, they can deposit their residual energy in the charge-collecting semiconductor. An event is recorded if the deposited charge is enough to be distinguished from the electronic noise level. This is the fundamental and simplistic mechanism for neutron detection using heterogeneous solid-state devices.

1.1.1 Thermal Neutron Detection with SSNDs

Most SSNDs use a neutron-converting material with a high thermal neutron absorption cross-section (e.g. ${}^{10}\text{B}$ or ${}^6\text{Li}$). These materials primarily detect neutrons in the thermal energy range (<0.5 eV). These isotopes have large thermal neutron ($E=0.0253$ eV)

absorption cross-sections—3840 and 941 barns, respectively. The neutron absorption reactions of these isotopes can be seen in equations (1) and (2):



Neutron moderators typically accompany thermal neutron detectors, which allow for the detection of fast neutrons once they undergo numerous scattering interactions in the moderator—a process called neutron moderation or thermalization. The moderation process reduces the neutron flux that is incident on the detector, which reduces the achievable absolute detection efficiency. However, the large thermal neutron cross-sections of the aforementioned isotopes make moderated thermal neutron detectors viable for the indirect detection of fast neutrons. The total energy-dependent cross-section of the aforementioned thermal neutron-converting isotopes— ${}^{10}\text{B}$ and ${}^6\text{Li}$ —can be seen in Figure 1.1.

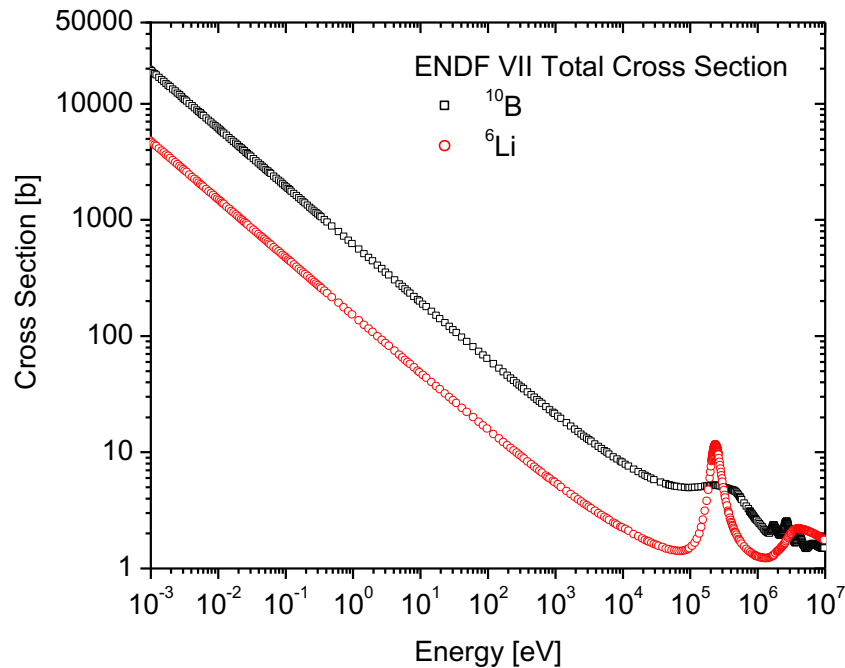


Figure 1.1: Total reaction cross-section of ${}^{10}\text{B}$ and ${}^6\text{Li}$ from ENDF VII.

Thermal neutron detection is achieved in SSNDs under the following conditions. First, a moderated neutron impinges on and is absorbed by the neutron-converting region (^{10}B or ^6Li). Next, one (or both) of the energetic, daughter ions produced in the converting material escapes this region, reaching the semiconductor with a fraction of its initial energy. This charged particle produces electron-hole pairs proportional to its residual energy in the semiconductor layer. The charge is conducted across the depletion layer, reaching the respective contact. The detector signal is amplified using standard nuclear instrumentation, i.e. a charge preamplifier, shaping amplifier, and analog-to-digital converter (ADC). These backend electronics can be used to produce a histogram of pulse amplitudes, called a pulse height spectrum (PHS). Events above the electronic noise level and gamma signal are counted as neutrons.

1.1.2 Fast Neutron Detection with SSNDs

SSNDs have been developed with the ability to directly detect fast neutrons as well. These devices use the same principles as the aforementioned SSNDs, but they rely on a different neutron-converting reaction. Solid-state fast neutron detectors implement a hydrogenous neutron-converting material (e.g. parylene or paraffin). Individual hydrogen atoms of the fast neutron-converting material can undergo proton recoil reactions in the presence of fast neutrons. When an energetic neutron elastically scatters with a hydrogen nucleus (proton), it transfers a fraction of its initial kinetic energy to the proton, seen by equation (3):

$$E_{loss} = E_n * \left(1 - \frac{\left(1 + \left(\frac{M-1}{M+1} \right)^2 \right) + \left(1 - \left(\frac{M-1}{M+1} \right)^2 \right) * \cos(\theta)}{2} \right) \quad (3)$$

Where E_{loss} is the energy transferred to the recoil nucleus (proton), E_n is the initial energy of the neutron, and θ is the scattering angle of the neutron in the center-of-mass system. The nuclear cross-section for elastic neutron scattering on ^1H is seen in Figure 1.2. The cross-section is significantly less than the thermal neutron absorption cross-sections of typical thermal neutron-converters. Since the detection efficiency is proportional to the

cross-section of the neutron-converter, solid-state fast neutron detectors are limited to significantly lower intrinsic neutron efficiency than their thermal counterparts. However, despite their low efficiency, neutron detectors that discriminate fast neutrons from thermal neutrons have uses for specific applications like neutron spectroscopy and neutron dosimetry.

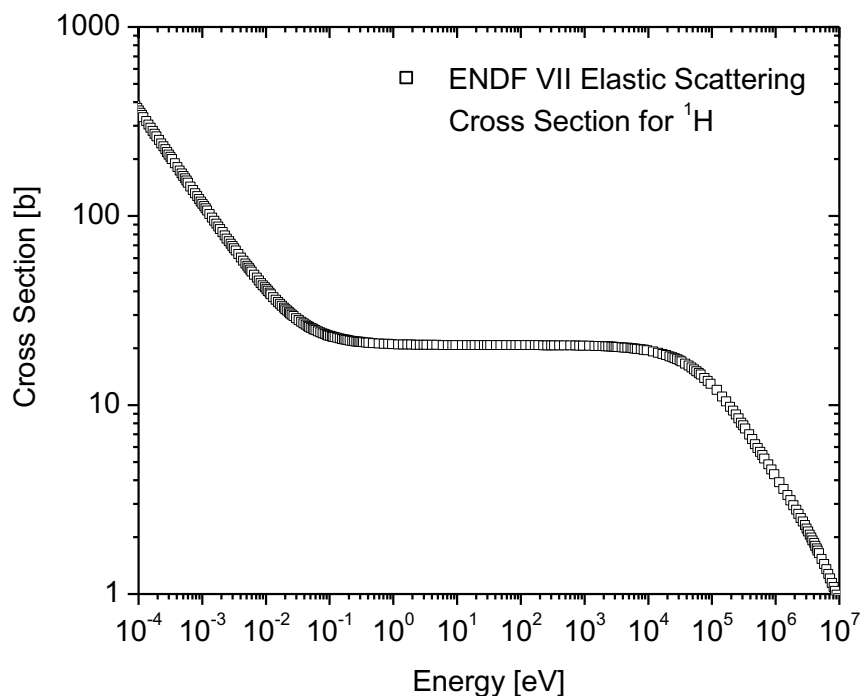


Figure 1.2: Cross-section for neutron elastic scattering with a hydrogen nucleus from ENDF VII.

1.1.3 Planar SSNDs

The first generation of heterogeneous SSNDs can be described as planar devices. This first type of SSND involves the juxtaposition of a thin neutron-conversion layer mounted on a semiconducting base [3], [4]. Many of iterations of these devices have been developed over the past decades [5]-[8]. A simple diagram of a planar solid-state thermal neutron detector can be seen in Figure 1.3. In the figure, an incident thermal neutron is absorbed in a neutron-converting region (pink). The resulting reaction products have the chance to escape the neutron-converter and deposit their energy in the semiconducting substrate, which is contacted on the front- and backside.

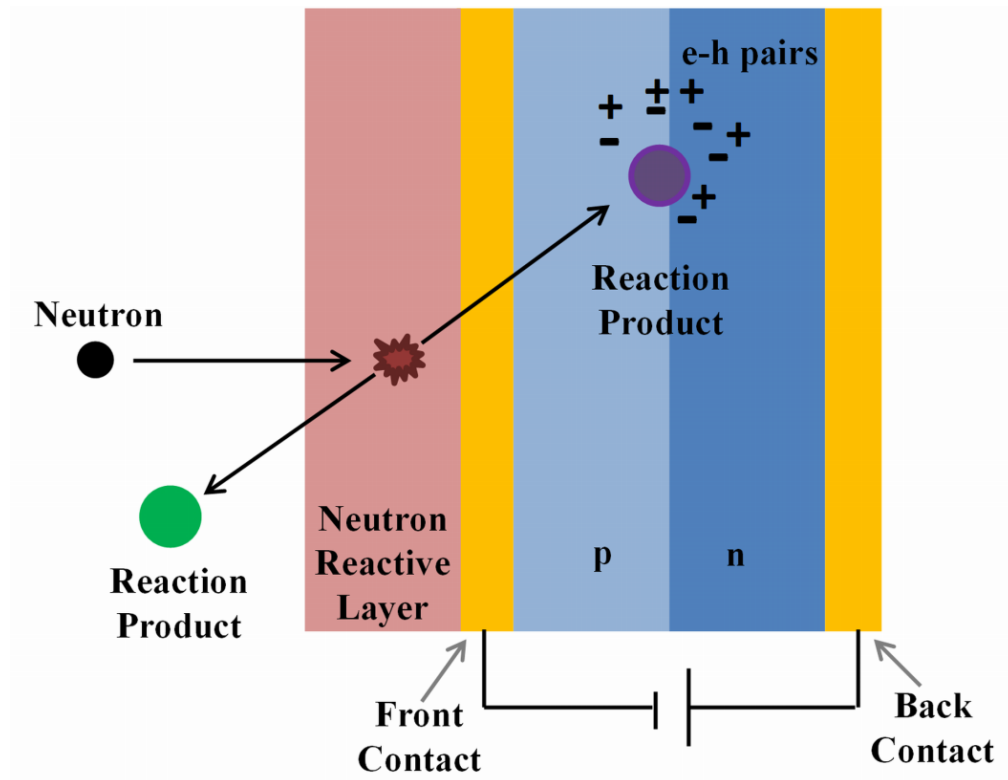


Figure 1.3: Diagram of a planar thermal SSND showing the energy deposition of a reaction produced by neutron absorption in a neutron-converting layer [9].

Since impinging neutrons produce daughter ions within the neutron-conversion layer, the thickness of this layer is limited by the range of the daughter ions. In other words, if the neutron-converting material is too thick, it is less likely that the reaction products will escape to the semiconducting region with sufficient energy to produce a signal above the noise level. This thickness can be optimized for a given neutron-converter and noise level using Monte Carlo simulations. Typically, these neutron-converting layers are a few microns thick, which is approximately the charged particle range in boron. However, the thin layer of neutron-converter limits the probability of neutron interaction and, therefore, the neutron efficiency. One way to improve the detection efficiency is to sandwich the neutron-converting layer with semiconductors, as shown in Figure 1.4 [10]. Additionally, individual planar SSNDs can be stacked by alternating layers of neutron-converting material and semiconducting bases in order to improve the intrinsic neutron efficiency.

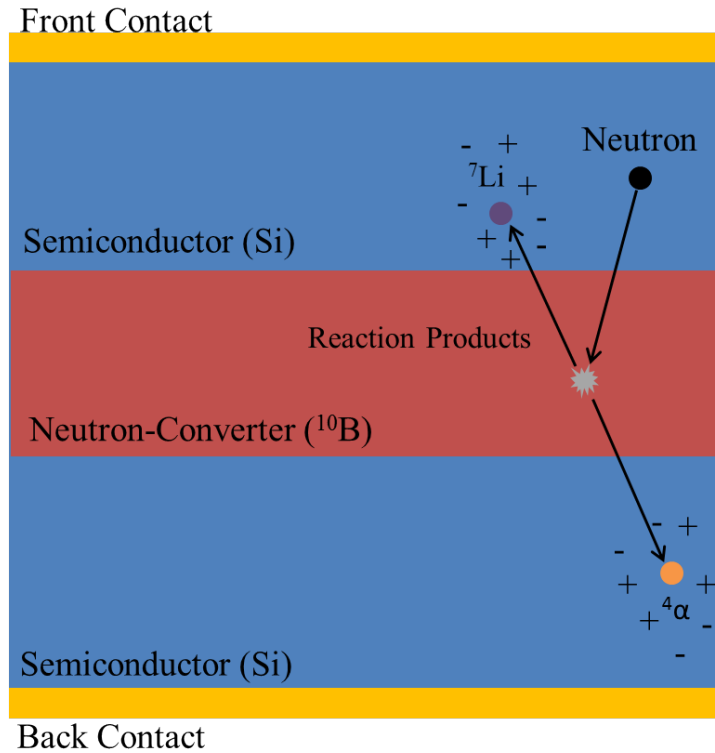


Figure 1.4: Diagram of a sandwiched planar SSND showing the energy deposition of a reaction produced by neutron absorption in a ^{10}B neutron-converting layer.

1.1.4 Microstructured SSNDs

More recently, microstructured SSNDs have been developed by several groups [11]-[13]. These devices utilize a semiconducting substrate—e.g. p- or n-type Si—which is etched with a repeated microstructure. The etching process can be performed by multiple methods, which are outlined in the subsequent section: Solid-State Detector Fabrication at RPI. Various microstructures have been used for such devices, including hexagonal holes, long and narrow trenches, repeated parallelogram holes, square holes, and cylindrical holes. The first set of successful microstructured devices produced at RPI had a honeycomb microstructure, which was produced by etching an array of hexagonal holes in the Si substrate. The etched microstructures are subsequently filled with the neutron-converting material, e.g. boron enriched in ^{10}B or lithium enriched in ^6Li . The deposition process was performed by chemical vapor deposition (CVD), but future devices were produced and tested which utilized electrophoretic deposition (EPD) and nanoparticle

deposition. This microstructured design allows for higher neutron efficiency than their planar SSND counterparts due to the increased amount of neutron-converting material and the augmented surface area separating the neutron-converter and the semiconductor. Otherwise, the process of detecting incident neutrons is similar to the aforementioned planar SSNDs, involving the conversion of a neutron into energetic, charged particles that escape the neutron-converting region and deposit their residual energy in the surrounding semiconducting substrate.

A diagram of a solid-state fast neutron detector with a hydrogenous neutron-converting material can be seen in Figure 1.5 [14]. This diagram depicts a cross-sectional view of two parylene-filled trenches with a trench depth, X_c , a trench width, W_c , and a silicon wall thickness, W_w . The angle of the scattered neutron is denoted by ϑ_n and the angle of the recoiled proton is denoted by ϑ_p . The path length of the recoiled proton in the neutron-converting region is C_{pl} , and the path length of the proton in the semiconductor—which leads to the production and conduction of electron-hole pairs—is denoted by S_{pl} . Similarly, a diagram of a thermal microstructured SSND can be seen in Figure 2.3. This device has the aforementioned honeycomb microstructure filled with enriched ^{10}B via CVD.

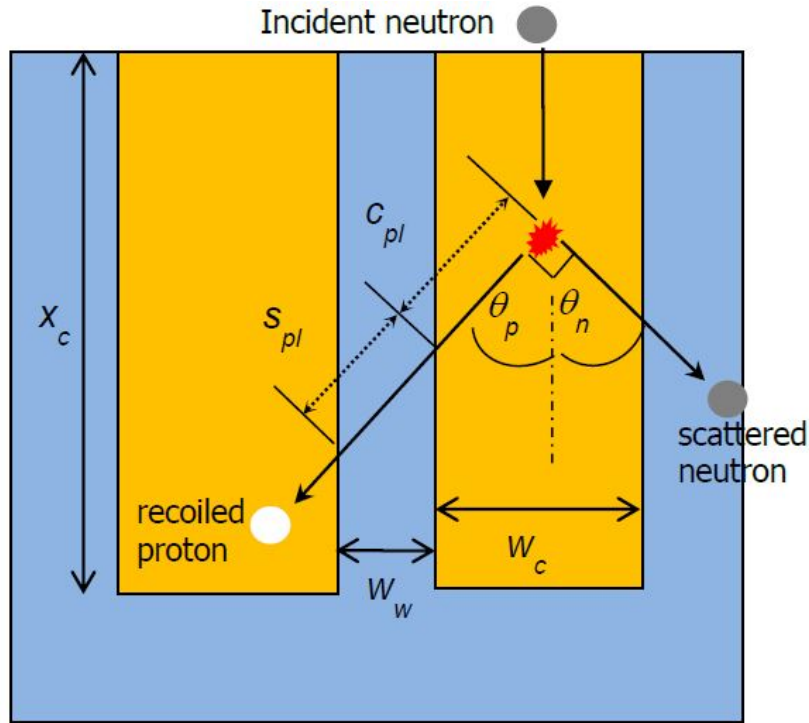


Figure 1.5: Diagram of a fast SSND demonstrating the trajectory of a recoiled proton and scattered neutron caused by a proton recoil reaction in the hydrogenous neutron-converting material [14].

1.1.5 Homogeneous SSNDs

A SSND is considered homogeneous if the semiconducting material is the same as the neutron-converting material. Therefore, semiconductors that are candidates for the fabrication of homogeneous SSNDs must contain a neutron-absorbing isotope (e.g. ${}^6\text{Li}$ or ${}^{10}\text{B}$). Since the neutron-converting material is part of the semiconductor, the reaction products of neutron absorption are born in the semiconductor. Therefore, every neutron-conversion results in some charge deposition in the semiconductor, so there is a potential for higher intrinsic neutron efficiency. Additionally, full charge collection is possible in a homogeneous SSND since the daughter ions do not need to escape the non-conductive, neutron-converting region.

A number of boron-based semiconductors have been investigated for the purpose of neutron detection. An early example involved the use of alpha-rhombohedral boron,

boron carbide (B_4C), and pyrolytic boron nitride (BN) [15]-[19]. However, the amorphous and/or polycrystalline structure of the semiconductor limits the performance of a device for neutron detection because the crystalline quality of the semiconducting film has a significant impact on the device's charge collection [20]. Therefore, the development of homogeneous SSNDs for thermal neutron detection relies on the development of high-quality semiconductors containing a neutron-converting material. So far, the full potential of homogeneous SSNDs has not been realized.

More recently, hexagonal boron nitride (hBN) has demonstrated promise as a material for the development of homogeneous SSNDs. Fundamental research with the goal of developing hBN crystals as neutron detectors has been performed by a number of groups [21]-[24]. Subsequently, neutron detectors have been developed with free-standing hBN thin films [25]-[26]. Furthermore, metal-semiconductor-metal (MSM) neutron detectors have been developed with hBN epitaxial layers [20]. A number of homogeneous hBN devices were tested and fabricated at RPI during the scope of this research, including the aforementioned free-standing hBN thin films, hBN grown on sapphire, hBN on Si, and MSM hBN devices [25]. These devices have demonstrated the ability to detect neutrons, but the inability to grow large, high-quality single crystals of hBN hinders these homogeneous SSNDs from reaching their theoretical capabilities as thermal neutron detectors [27]. The performance and properties of these hBN devices developed at RPI will be discussed in subsequent sections.

2. Solid-State Detector Fabrication at RPI

During the scope of this research, hundreds of individual microstructured devices were fabricated and tested at RPI. These devices had a range of microstructure patterns, neutron converting materials, semiconductor substrates, etching processes, and filling methods. The fabrication processes and the challenges associated with the most promising designs are outlined in this section.

The first iteration of microstructured SSNDs produced at RPI had a honeycomb microstructure design. Individual devices have an area of $2.5 \times 2.5\text{mm}^2$, 15 of which were connected in parallel to produce $\sim 1\text{cm}^2$ detectors, with one $2.5 \times 2.5\text{mm}^2$ pad used to connect the signal output. Four 1cm^2 detectors were connected in series to produce the 4cm^2 detectors that were used to develop and test the novel applications presented in this thesis. These honeycomb devices demonstrate good thermal neutron detection efficiency, adequate gamma discrimination, scalability to large areas, and robustness to radiation damage [28]. However, the production of these devices requires expensive techniques and equipment. Therefore, the goal of this research—and a significant contribution of the work presented in this thesis—was the design, fabrication, and testing of a more cost-effective detector design. A second successful iteration of devices fabricated at RPI had a trench microstructure filled with enriched boron nanoparticles. The use of a trench microstructure allows for wet chemical etching to replace deep reactive ion etching, and the use of boron nanoparticles eliminated the need for chemical vapor deposition. Both of these tradeoffs facilitate the production of microstructured SSNDs at a lower cost. Additionally, homogeneous SSNDs were fabricated by growing hBN on sapphire and Si substrates. These devices were grown using free-standing crystals and metal-semiconductor-metal (MSM) designs, which will be discussed in the subsequent sections. Lastly, parylene-filled honeycomb devices were fabricated in order to develop a microstructured SSND for fast neutrons.

2.1 Honeycomb SSND Fabrication

The honeycomb devices were fabricated at RPI within RPI's Micro and Nano Fabrication Clean Room using a 4-inch (1 0 0) moderately-doped n-Si wafer substrate with a resistivity

of $\sim 0.5 \Omega\text{-cm}$. In short, a honeycomb microstructure was etched into the substrate, and the hexagonal holes were subsequently filled with enriched ^{10}B . The hexagonal holes were etched to a depth of $45 \mu\text{m}$ in an active Si region with a thickness down to $60 \mu\text{m}$. Each device was $2.5 \times 2.5 \text{mm}^2$, and 15 were connected in parallel in order to create a $\sim 1 \text{cm}^2$ device.

More specifically, the recipe used to produce the honeycomb devices begins with the epitaxial growth of a $1\text{-}\mu\text{m}$ layer of heavily doped p-Si on the n-Si substrate. Next, etching the substrate using reactive ion etching (RIE) with sulfur hexafluoride (SF_6) and oxygen (O_2) plasmas formed the device areas. A layer of silicon dioxide (SiO_2) was used to passivate the exposed sidewalls. The honeycomb microstructure of the device was produced by etching a repeated lattice of hexagonal holes with high aspect ratios. These holes have a diameter of approximately $3\mu\text{m}$ and a depth of about $45\mu\text{m}$ and were etched using photolithography, dry etching, and deep reactive ion etching (DRIE) of the Si substrate using the Bosch process [29]. A continuous $\text{p}^+\text{-n}$ junction was formed over the device surface by depositing a thin layer of enriched boron and exposing it to 800°C for 10 minutes using a low-pressure chemical vapor deposition (LPCVD) system. The formation of this continuous $\text{p}^+\text{-n}$ junction is crucial in order to achieve low noise levels and, therefore, higher detection efficiency. The hexagonal holes were filled with enriched boron using LPCVD with a diborane (B_2H_6) gas precursor diluted to 1% in hydrogen (H_2). The boron filling of the microstructures first deposits along the sidewalls, typically plugging the neck before completely filling the holes. A fill factor of $\sim 85\%$ was estimated from SEM images. Boron is subsequently removed from the contact areas, and finally the sputtering of aluminum (Al) and titanium (Ti) contacts completed the device fabrication process [13]. The contour and aspect ratio of a typical honeycomb device can be seen by the scanning electron microscope (SEM) images in Figure 2.1 and Figure 2.2. A schematic of a typical device produced by these processes can be seen in Figure 2.3 [13]-[14].

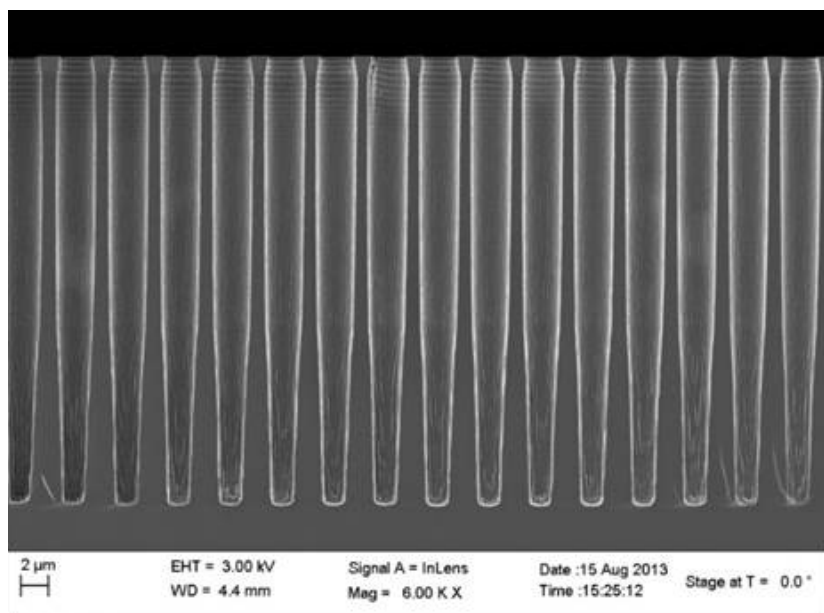


Figure 2.1: Cross-sectional SEM image of a honeycomb device filled with enriched ^{10}B via CVD.

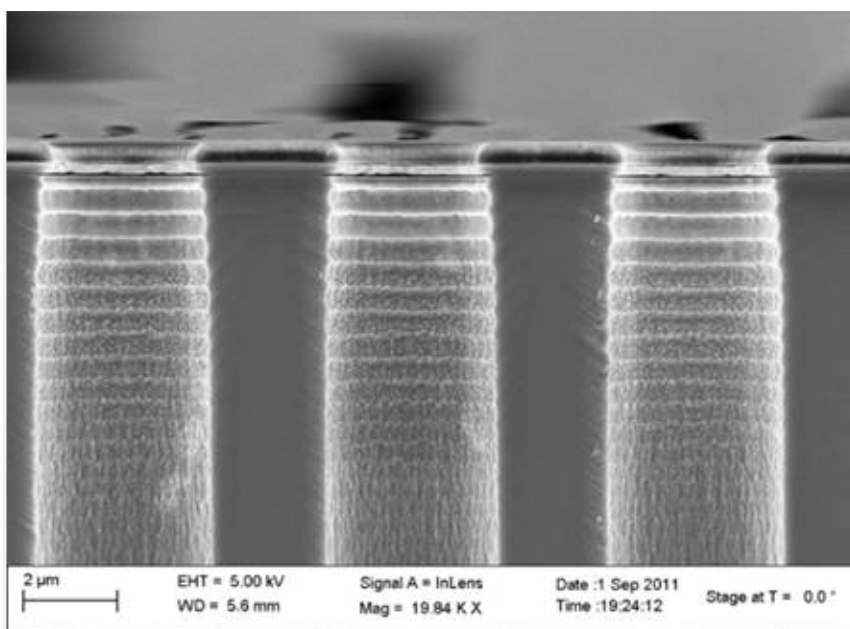


Figure 2.2: Zoomed in cross-sectional SEM image of a honeycomb device filled with enriched ^{10}B via CVD.

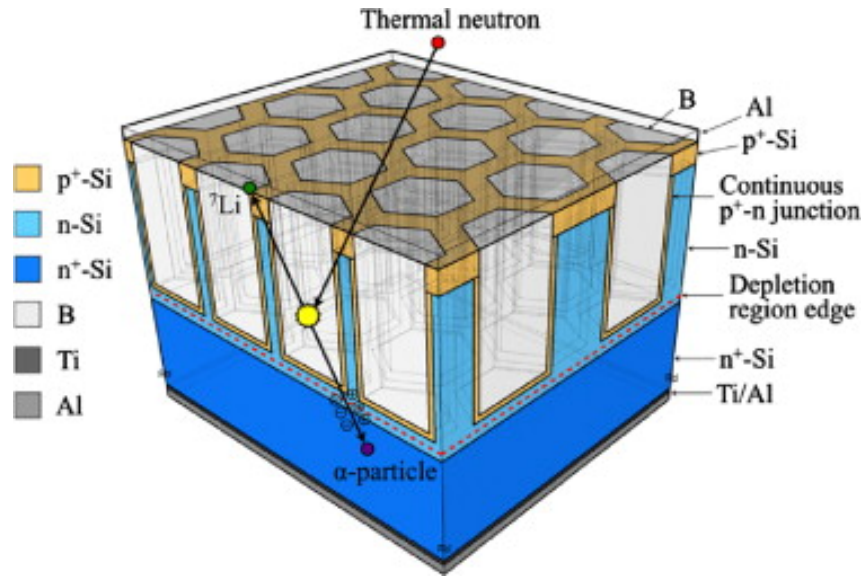


Figure 2.3: Schematic of a honeycomb structured SSND [13].

Overall, the fabrication of these honeycomb microstructured SSNDs was successful and well-documented. These devices perform well, demonstrating high thermal neutron detection efficiency (up to 28.3%), low gamma-sensitivity, scalability to larger areas due to the extremely low leakage current, and robustness [13]. However, the high-cost and complicated fabrication processes associated with the honeycomb devices leaves room for improvement. The development of newer generations of microstructured SSNDs at RPI aimed to reduce the costs and simplify the fabrication processes with a minimal reduction in performance. These newer microstructured SSNDs were compared to the original honeycomb devices, which served as a benchmark for success.

2.2 Trench Microstructure SSND Fabrication

A second iteration of devices was designed in order to reduce the costs associated with the fabrication processes required to produce the aforementioned honeycomb devices. These new devices utilize a trench microstructure, which can be produced via wet chemical etching using TMAH or KOH as the reactive agent. The resulting deep trenches were filled with either enriched boron or B₄C nanoparticles from various vendors. Eventually, pure boron nanoparticles (96% ¹⁰B) were chosen as the neutron converting material. Since boron nanoparticles have a higher boron density than B₄C nanoparticles, devices filled with the former material result in slightly higher detection efficiencies.

These trench microstructure devices were originally produced using a 4-inch (110) n-type Si wafer with a resistivity of 20-80 Ω -cm. Subsequently, a 4-inch (110) wafer with lesser resistivity (between 3-10 Ω -cm) and a thickness of 550 μ m was used, as this change resulted in enhanced charge collection. The front side of the wafer was doped with boron using an activated boron source at a temperature of 1000°C in order to produce a \sim 1 μ m-thick p^+ layer. The backside was subsequently doped in order to form a 1 μ m-thick n^+ layer. The backside was doped with $POCl_3$ at 950°C in order to produce a n^+ layer. Photolithography and RIE were used to isolate the individual devices. A 1.5 μ m-thick layer of SiO_2 was passivated on the sidewalls of the Si, and a 200 nm-thick layer of low stress silicon nitride was deposited on each side of the wafer as a mask for the subsequent trench etching. The trenches were etched using either TMAH or KOH etching. Devices with trench widths varying from 3.5-8.0 μ m and trench depths between 60-120 μ m were etched, depending on the individual design. Multiple trench designs were used; Figure 2.4 depicts two microstructure trench designs. The new design shown in Figure 2.4 (Right) has improved strength, which allowed for longer trenches. These longer trenches resulted in a better nanoparticle fill factor and were less prone to cracking. Devices with this new design were produced with different trench widths and depths.

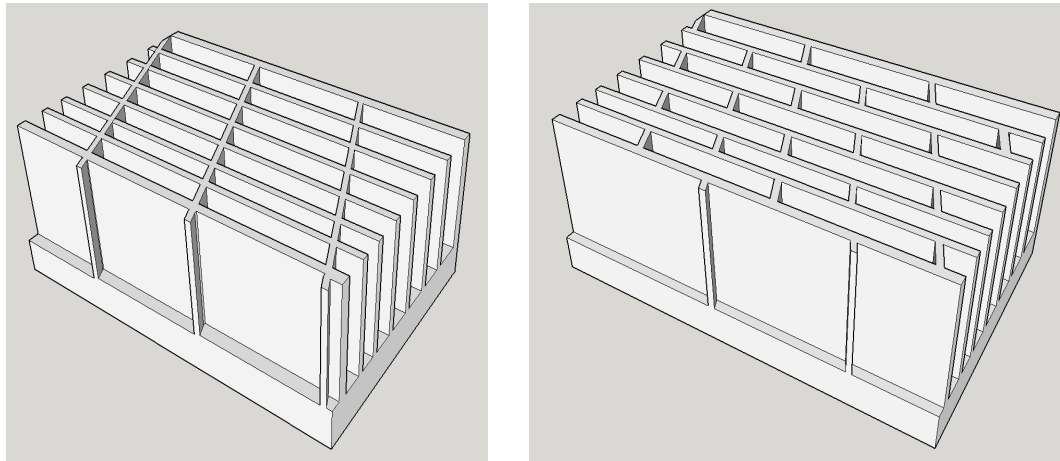


Figure 2.4: (Left) Original trench design. (Right) New trench design with increased strength allowing for longer trenches resulting in better nanoparticle filling.

Next, the continuous $p^+ - n$ junction was formed using the boron source at 1000°C . Again, the formation of the continuous junction is essential in order to reduce the device leakage current and noise level. Subsequently, Ti and Al were sputtered onto the backside of the device in order to produce the electrical contacts. Enriched boron nanoparticles (96% ^{10}B) were used to fill the trenches. One of two filling methods developed at RPI were used for the deposition: vacuum assisted filling and electrophoretic deposition. Lastly, the front side contact was created by sputtering 300 nm of Al using a 1-mm^2 shadow mask. The 4-inch wafer was diced into individual 1-cm^2 devices, which were mounted on a copper plate. A schematic of the device can be seen in Figure 2.5, and an SEM imaged of the filled trenches can be seen in Figure 2.6. Similarly, a 3-D schematic of a boron nanoparticle-filled trench microstructured SSND can be seen in [30].

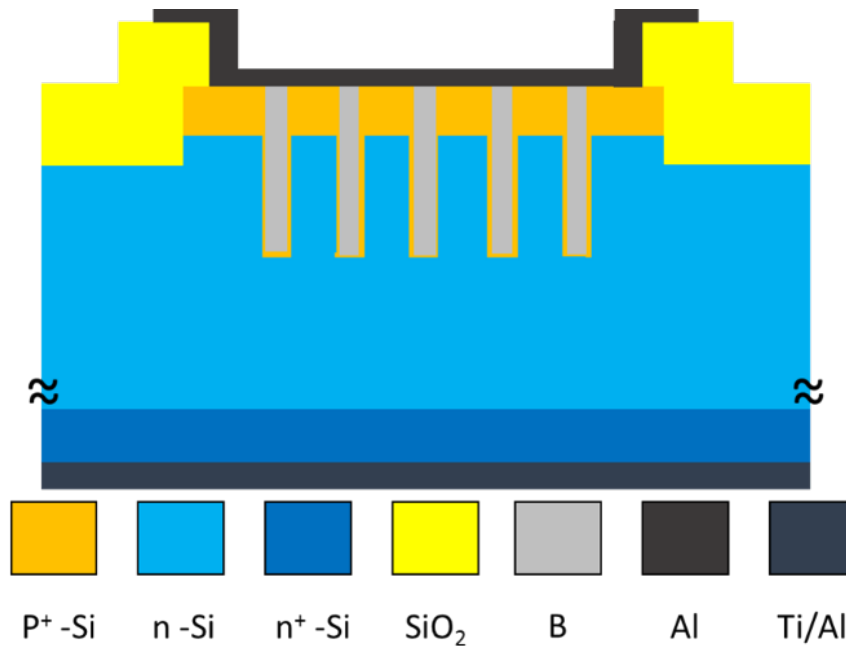


Figure 2.5: Schematic of the RPI-developed, trench microstructured SSND filled with enriched boron nanoparticles.

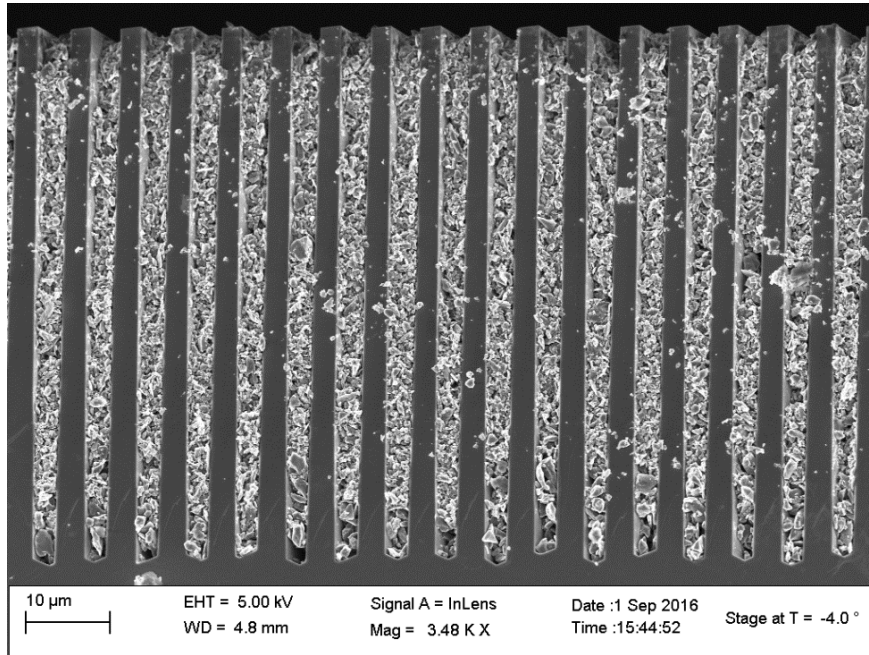


Figure 2.6: Cross-sectional SEM image of the boron nanoparticle-filled trench microstructure SSND with trench widths of $3.5\ \mu\text{m}$ and Si wall widths of $2\ \mu\text{m}$.

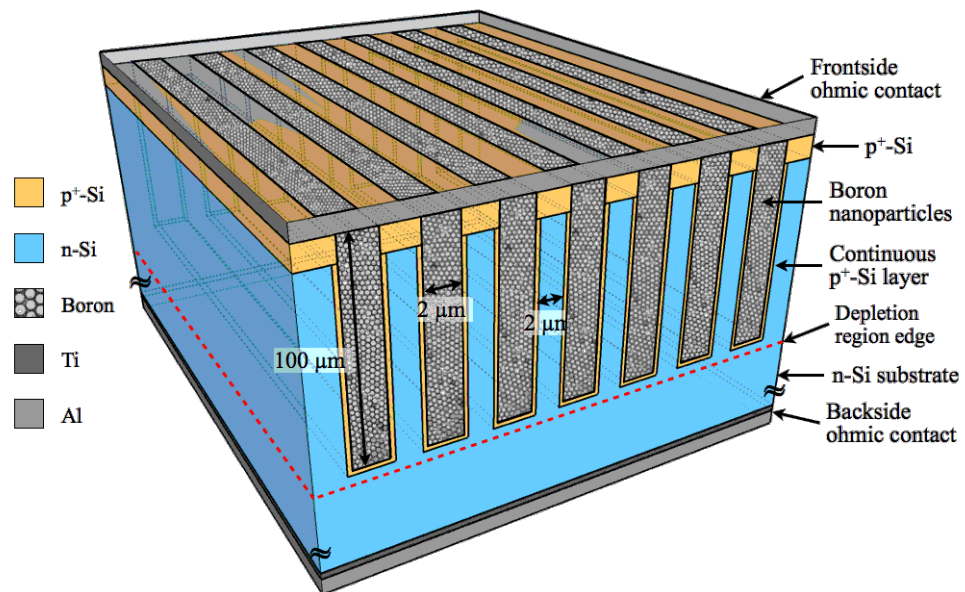


Figure 2.7: Schematic of a boron nanoparticle-filled microstructured trench SSND.

Again, two methods were used to insert these nanoparticles into the microstructured trenches. Both methods began by dissolving the nanoparticles in acetone or isopropyl

alcohol. The first successful method is termed electrophoretic deposition (EPD) and involved applying a modulating external electric field around a properly patterned wafer surface. An example of a cell used for this EPD can be seen in Figure 2.8.

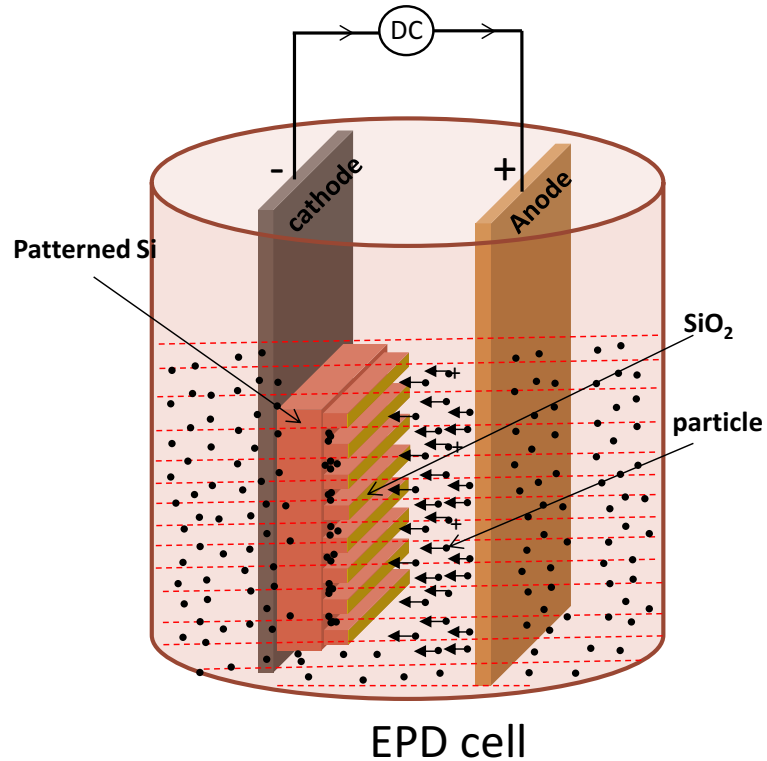


Figure 2.8: Example of an EPD cell used to deposit nanoparticles into the trench microstructures of a SSND.

Overall, this EPD of nanoparticles was successful, and a number of devices were produced and tested using this method. However, some trenches were not completely filled using this method. Additionally, good results were difficult to reproduce consistently with this method. Figure 2.9 shows an SEM image of a trench device filled with B₄C nanoparticles.

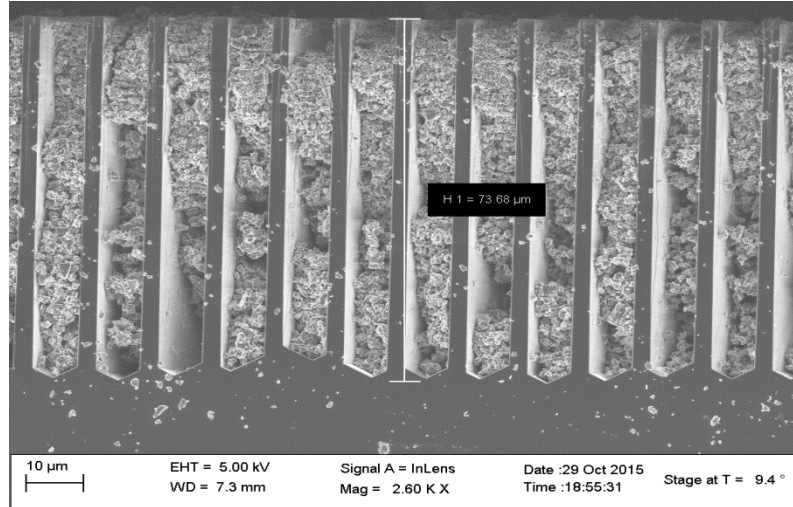


Figure 2.9: SEM imaged of a trench microstructured SSND filled with enriched B₄C nanoparticles via EPD.

Since the EPD resulted in lackluster and relatively inconsistent filling, a vacuum assisted filling process was developed. A large vacuum chamber with feedthroughs, which was able to handle an entire 4-inch wafer, was utilized for this procedure (Figure 2.10). The device was covered with the nanoparticle slurry, placed in the vacuum chamber, and the internal pressure in the chamber as varied. This alternating vacuum resulted in a nanoparticle fill that had a better fill factor and significantly better reproducibility than the EPD method. Figure 2.11 and Figure 2.12 show SEM images of a trench microstructured SSND filled with ¹⁰B via the aforementioned vacuum-assisted process.

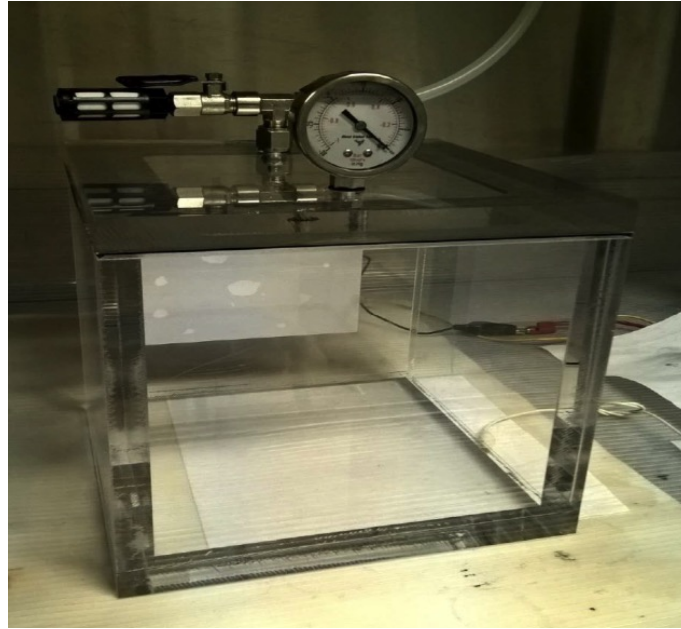


Figure 2.10: Large vacuum chamber used for the vacuum-assisted filling of the microstructured trench SSNDs.

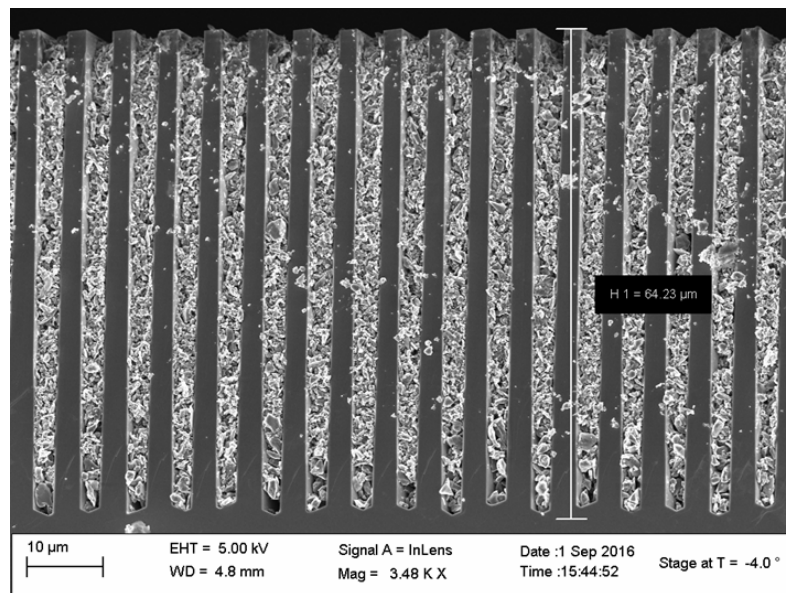


Figure 2.11: SEM image of a trench microstructured SSND filled with ^{10}B nanoparticles via vacuum-assisted filling. The trenches are 2.5-3.5 μm wide, 65 μm deep, and are etched using TMAH.

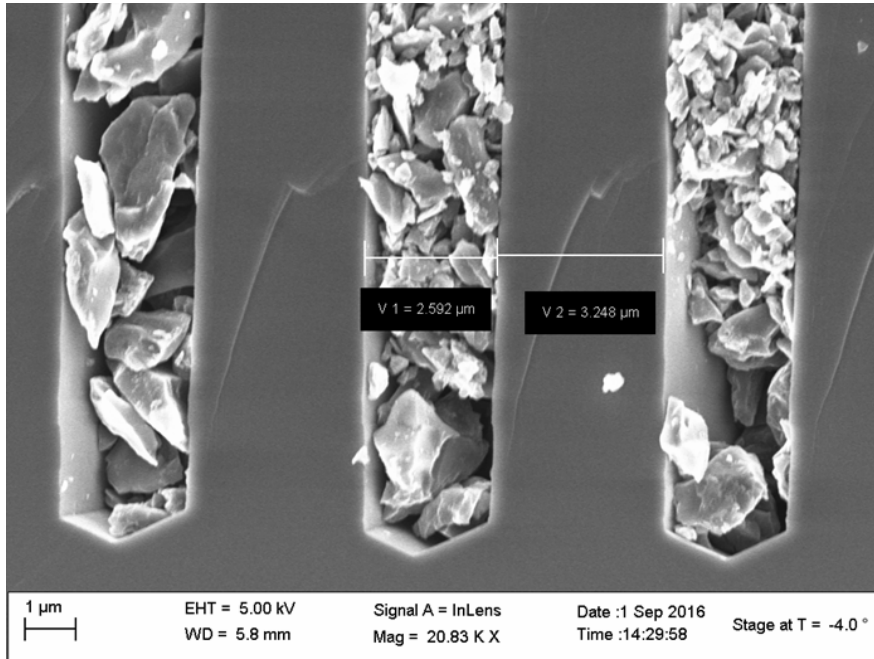


Figure 2.12: Zoomed in image of a trench microstructured SSND filled with ^{10}B nanoparticles via vacuum-assisted filling with an effective density of $\sim 0.6 \text{ g/cm}^3$.

Overall, the processing and development of the trench devices is more accessible, less costly, and simpler than the aforementioned honeycomb devices. For example, the following list demonstrates the simpler fabrication processes associated with the trench microstructured SSNDs:

- Two less lithography processes are required for device isolation and boron etching.
- Furnace diffusion can be used for the continuous p^+ and n^+ formation.
- Batch fabrication is possible and there is no post-annealing requirement, as opposed to ion implantation.
- Slightly larger Si walls allow for single diffusion of the front side p^+ and continuous p^+ layer.
- There is no requirement for mesa etching due to the more planar structure.
- Metallization can be performed before the boron filling. Therefore, the complete device can be fabricated before the filling process.

Additionally, the wet chemical etching can produce trenches that are significantly deeper ($>100 \mu\text{m}$) than the honeycomb microstructures formed via DRIE. The use of deeper

trenches help to achieve a higher neutron detection efficiency, despite the reduced density of the neutron converting nanoparticles [30]. The vacuum-assisted nanoparticle filling involves low-maintenance tools and can be performed at room temperature. The costs associated with this filling process are significantly less, as enriched ^{10}B nanoparticles cost approximately \$48/gram, while B_2H_6 gas used for LPCVD costs around \$2,500/gram. Table 2.1 shows a side-by-side comparison of the fabrication processes of the two aforementioned microstructured devices.

Table 2.1: Side-by-side comparison of the fabrication processes used to produce the aforementioned honeycomb and trench microstructured SSNDs.

	Honeycomb detectors	Trench detectors
Si Wafer	(100) epi wafer	(110) bulk wafer
$\text{p}^+\text{-n-n}^+$ preparation	Ion implantation and annealing	Furnace diffusion (p+ is formed during continuous p)
Device isolation	Required	Not required
Field oxide passivation	Required	Required
Etch	Dry etch (DRIE)	Wet etch (KOH, TMAH)
Continuous $\text{p}^+\text{-n}$	Required (LPCVD)	Required (Furnace)
Boron filling (tool)	^{10}B (LPCVD)	^{10}B nanoparticles (vacuum box)
Boron etch	Required	Not required
Metallization	Required	Required

3. Simulation and Optimization of SSNDs

The strategically selected microstructure devices that were considered as candidates for the future direction of microstructured SSND development at RPI were fabricated using the aforementioned Si substrates and include: honeycomb, trench, and parallelogram microstructures filled with boron, boron carbide, and boron nitride via CVD. Additionally, deeper trench microstructures filled with boron and boron carbide (B_4C) nanoparticles filled via an alternating vacuum process were considered. The eleven combinations of these microstructure designs and neutron-converting materials were each simulated using Monte Carlo N-Particle Code (MCNP) 6.1 [31]. The simulations provide insight into the behavior and charge deposition of the daughter particles (7Li and ${}^4\alpha$) in the Si charge-collecting region due to ${}^{10}B$ neutron absorption and subsequent escape from the neutron-converting region.

These simulations also proved useful for the determination of the optimal microstructure sizing for each microstructure geometry, fill material and density, noise level, and microstructure depth. The optimal microstructure sizing for each device was determined by creating a large set of simulations for each of the eleven devices. For instance, a honeycomb device filled with boron using CVD was simulated with incremental hexagonal diameters and Si wall thicknesses, while the other parameters that affect the efficiency—i.e. microstructure depth, neutron converter density, and device noise level—were held constant. The intrinsic thermal neutron efficiency of each simulated device was determined, and the results were used to determine the geometrical parameters which result in the optimal detection efficiency. Color contour plots were used to graphically represent how the simulated efficiency changes with the variable microstructure sizing. These plots were used in order to determine the optimal microstructure sizing for each device design, which was necessary in order to maximize the device performance. Therefore, this information was used to guide the detector design and fabrication process. It is worth mentioning here that the microstructure geometry is not the only factor affecting the device efficiency, but it provides a starting point for the design phase. Other factors affecting the efficiency—e.g. the method of producing the depletion region, the device

capacitance, leakage current, device depth (thickness), neutron converter density, and ^{10}B enrichment—will be considered later.

Once the optimal geometry of each of the eleven aforementioned devices was determined via MCNP simulation, the relative performance—i.e. intrinsic thermal neutron detection efficiency—of the optimized devices was compared to one another. For example, it was determined that devices with a honeycomb microstructure generally result in higher efficiency than a device parallelogram microstructure. Additionally, a device filled with boron via CVD results in a higher efficiency than the same device filled with boron nitride. These results were used to provide a recommendation and guide for the future direction of SSND development at RPI. Additionally, the relative costs and required equipment associated with the various processes corresponding to the various device designs were considered. Lastly, physical constraints were considered; for example, trench microstructures with Si walls $\leq 1\ \mu\text{m}$ were mechanically unstable. It is also worth noting that the deeper trench devices filled with nanoparticles have higher gamma sensitivity due to a thicker parasitic Si substrate. While these considerations are all significant, the following MCNP simulations ignore the physical constraints and simply compare the simulated intrinsic thermal neutron efficiencies.

MCNP simulations were also used in order to directly compare the simulated efficiencies to the actual, experimentally measured intrinsic thermal neutron efficiencies of the fabricated devices. A realistic simulation of the experimental setup—including the moderated ^{252}Cf fission neutron source—was used to estimate the intrinsic thermal neutron efficiency of the devices. Discrepancies between the simulated and experimentally measured intrinsic thermal neutron efficiencies demonstrate that there is room for improvement of the device performance, e.g. noise level and charge collection. Conversely, general agreement between the measurement and simulation demonstrates that the device is performing near the theoretical maximum for a given noise level, device thickness, microstructure geometry, etc. Additionally, general agreement between the simulations and experimental measurements provides confidence that the simulations are accurately modeling the charged particle transport in the devices and provides a sanity

check for the experimental method used to measure the intrinsic thermal neutron efficiency, which is described in detail in subsequent sections.

The same realistic MCNP simulations were used to predict the shape of the pulse height spectra generated by the charge deposition and charge collection in the silicon device. These simulated pulse height spectra were compared to the experimentally-collected spectra of the corresponding device. Again, agreement between the simulated and experimental pulse height spectra serves as a sanity check, providing some evidence that the devices are modeled accurately and the underlying energy mechanisms of charged particle production and deposition are well understood and modeled accurately.

3.1 Comparison and Optimization of Microstructured SSND Designs

As mentioned in the previous section, MCNP simulations were used in order to optimize the geometry of the various microstructure SSNDs investigated and fabricated at RPI. Eleven devices were simulated in total: CVD of boron, boron carbide, and boron nitride in a honeycomb, parallelogram, and parallel trench microstructure and deposition of boron and boron carbide nanoparticles in a deeper, wider trench microstructured device. A set of simulations was prepared for each device (e.g. honeycomb, trench, etc.) with variable microstructure sizes, while the device thickness, neutron converting material, corresponding density, and estimated noise level (LLD) were held constant in order to isolate the impact that the microstructure sizing plays on the efficiency. Each individual MCNP output file provided the data needed to determine the simulated intrinsic thermal neutron efficiency, which was plotted as a function of the microstructure size on a color contour plot. Examples are shown in Figure 3.4, Figure 3.5, and Figure 3.6. The microstructure size of the honeycomb microstructure was defined by the hexagonal diameter in μm and Si wall width μm . Similarly, the side length of the filled parallelogram and the Si wall width described the size of the parallelogram microstructure, and the trench sizing was described by the trench width and the adjacent Si wall width. The resulting color contour plots depict the relationship between the efficiency and the microstructure sizes for a given device design. These plots provided a useful visual guide for the strategic design and fabrication of the microstructured devices.

Each MCNP6 input file was created using a repeated lattice of the corresponding microstructure embedded in a Si substrate ($\rho=2.329 \text{ g/cm}^3$) with an area of $0.2 \times 0.2 \text{ cm}^2$. The microstructured devices filled via CVD have an etched microstructure depth of $45 \text{ }\mu\text{m}$ in a $60 \text{ }\mu\text{m}$ -deep Si substrate, which reflects the current fabrication and filling capabilities. The trench microstructured devices filled with nanoparticles have an etched depth of $70 \text{ }\mu\text{m}$ in a $200 \text{ }\mu\text{m}$ -deep Si substrate. The microstructures were filled with the corresponding neutron-converting materials. Devices filled via CVD were assumed to have the nominal density—(2.35 g/cm^3 for boron, 2.52 g/cm^3 for boron carbide, and 2.1 g/cm^3 for boron nitride). The incomplete filling of the honeycomb and parallelogram microstructures was modeled by including a hollow cylindrical volume in the center of the microstructure. For example, an 85% fill factor was created by introducing a central cylinder with 15% of the volume. The $70 \text{ }\mu\text{m}$ -deep trench devices filled with nanoparticles were modeled as completely and homogeneously filled. The uniform B and B_4C nanoparticle density was determined to be 0.7 g/cm^3 . This nanoparticle density was determined by measuring the mass of a device before and—subsequently—after the filling process. The nanoparticle density was calculated to be $\sim 0.7 \text{ g/cm}^3$ by dividing the mass difference—assumed to be from the deposited nanoparticles—by the total volume of the trenches, shown by equation (4).

$$\rho_{nanoparticles} \left[\frac{g}{cm^3} \right] = \frac{Nanoparticle \ Mass \ [g]}{Trench \ Volume \ [cm^3]} \quad (4)$$

As previously mentioned, a fill factor of 85% was modeled for the CVD devices by introducing a cylindrical void in the center of each filled microstructure. A zoomed-in, top-view diagram of a simulated honeycomb device with a fill factor of approximately 85% is shown in Figure 3.1, where D_H is the diameter of the hexagonal holes and W_W is the width of the Si walls. Additionally, a schematic of a simulated trench device with a homogeneous and uniform deposition is shown in Figure 3.2, where W_T is the width of the trench filled with the neutron-converting material and W_W is the width of the Si walls.

Lastly, a schematic of a simulated parallelogram device is shown in Figure 3.3, where W_p is the width of the filled parallelogram.

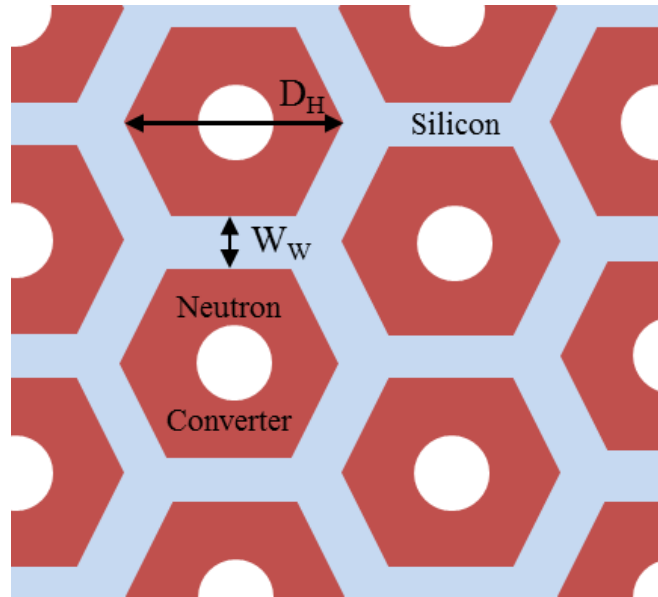


Figure 3.1: Top-view schematic of the repeated structures used to simulate the honeycomb microstructured SSNDs with MCNP6.1.

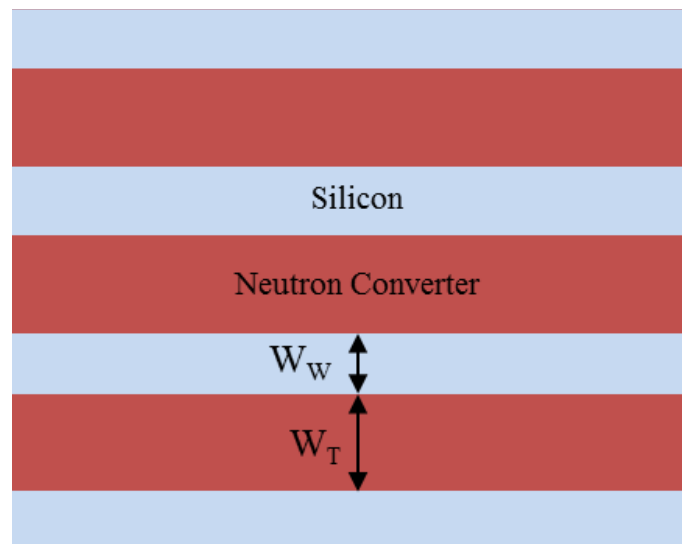


Figure 3.2: Top-view schematic of the repeated microstructure used to simulate the trench microstructured SSNDs.

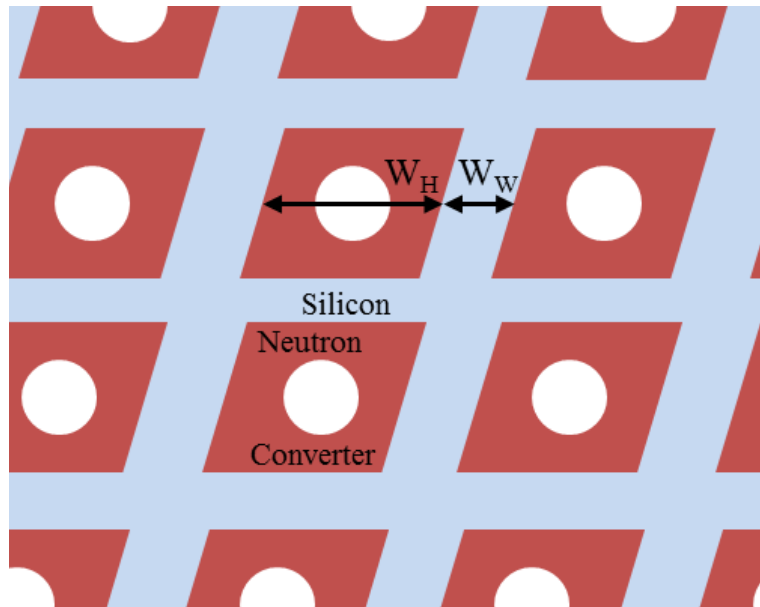


Figure 3.3: Top-view schematic of the repeated microstructure used to simulate the parallelgram microstructured SSNDs.

For each simulation used to determine the optimal microstructure geometry, an isotropic thermal neutron point source ($E=0.0253$ eV) was centered above the top face of the device. Some neutrons resulted in a $^{10}\text{B}(n,\alpha)^7\text{Li}$ reaction, producing energetic charged particles which had a chance to escape the boron region reaching the charge-collecting Si. A pulse height (F8) tally of the alpha particles and Li ions in the Si substrate was collected in order to record events that would produce a pulse above the intrinsic noise level. Simulations were performed with an assumed noise level (lower level discriminator [LLD]) of 200 and 500 keV, consecutively.

In the aforementioned simulations, a neutron event is counted under the following conditions: a thermal neutron (in this case $E_n=0.0253$ eV) impinges upon and is absorbed by a ^{10}B nucleus in the neutron-converting material. The resulting alpha particle and/or Li ion escape(s) the neutron converting region, reaching the Si substrate with a fraction of its initial energy. If the charge particle(s) deposit enough energy in this region to be distinguished from the electronic noise—200 or 500 keV (depending on the LLD)—a count is recorded. A surface flux (F2) tally was collected on the top face of the device in order to track the number of neutrons that pass through the device. A cosine card was

used to discriminate the neutrons which are reflected back towards the tallied surface, and the tally was multiplied by the surface area in order to determine simulated thermal neutron flux. The simulated thermal neutron intrinsic efficiency ($E_n=0.0253$ eV) of the device was calculated as the ratio of thermal neutrons which lead to events above the pre-determined noise level (LLD) divided by the number of non-reflected thermal neutrons passing through the detector. Two large sets of simulations were performed for each of the eleven aforementioned devices with variable geometric parameters, one with an LLD of 200 keV and a second with an LLD of 500 keV. Each simulation was run until 1×10^5 histories were completed, providing relative uncertainties of the intrinsic thermal neutron efficiency $< 1\%$. Three examples of MCNP inputs (one honeycomb, one parallelogram, and one trench microstructure input) which were used to simulate the devices' detection efficiency can be found in Appendix B. The first input corresponds to a boron-filled ($\rho=2.35$ g/cm³) honeycomb microstructure with a hexagon diameter of 3.0 μm , a Si wall width of 1.0 μm , a boron fill factor of 0.85—modeled as a voided cylinder in the center of the hexagonal prism, a depth of 45 μm , and an LLD of 200 keV. The second input represents a B₄C-filled ($\rho=2.52$ g/cm³) parallelogram microstructure with a parallelogram width of 3.0 μm , a Si wall width of 1.0 μm , a fill factor of 0.85, a depth of 45 μm , and an LLD of 200 keV. The third input corresponds to a boron nanoparticle-filled ($\rho=0.7$ g/cm³) trench microstructure with a trench width of 2.5 μm , a Si wall width of 1.0 μm , and an LLD of 200 keV. The nanoparticle fill is modeled as a homogenous medium with an effective density consistent with laboratory measurements.

The resulting MCNP outputs were used to create color contour plots, which illustrate how the intrinsic thermal neutron efficiency behaves as a function of the microstructure and Si wall sizes at two different noise levels. For instance, a color contour plot corresponding to a honeycomb device filled with boron (93% ¹⁰B) via CVD with a fill factor of 85% and an LLD of 200 keV was produced by varying the hexagonal diameter from 1.0 μm to 4.5 μm by increments of 0.25 μm . The Si wall thickness was varied from 1.0 μm to 2.5 μm by 0.25 μm increments (Figure 3.4). Similarly, a contour plot corresponding to a parallelogram device filled with B₄C via CVD with a fill factor of 85% and an LLD of 200 keV was produced by varying the parallelogram sides from 1.0 μm to 5.0 μm by

increments of 0.25 μm . The Si wall thickness was varied from 1.0 μm to 4.0 μm by 0.25 μm increments (Figure 3.5). Additionally, a contour plot corresponding to a trench device filled with BN via CVD with an LLD of 500 keV was produced by varying the trench width from 1.0 μm to 5.0 μm by increments of 0.25 μm . Similarly, the Si wall thickness was varied from 1.0 μm to 4.0 μm by 0.25 μm increments (Figure 3.6). The complete set of contour plots can be seen in Appendix A. It is important to note that these intrinsic thermal neutron efficiencies were simulated with a monoenergetic neutron source with an energy of 0.0253 eV. Therefore, these simulations predict the device efficiency at 0.0253, which is approximately 20% higher than the thermal averaged intrinsic neutron detection efficiency, due to the $1/v$ cross-section of ^{10}B .

45 μm Honeycomb, CVD of 93% ^{10}B ($\rho=2.35\text{ g/cm}^3$), LLD 200 keV

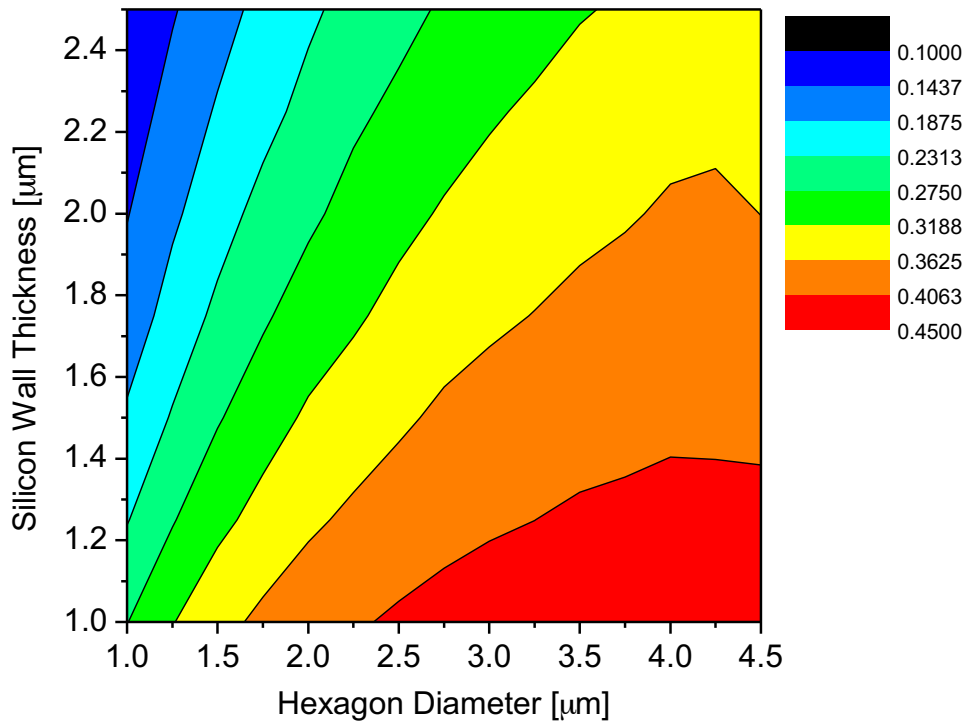


Figure 3.4: Contour plot showing the simulated thermal neutron efficiency as a function of the hexagonal diameter and silicon wall thickness of a 45 μm -deep honeycomb device filled via CVD of boron ($\rho=2.35\text{ g/cm}^3$) and an LLD of 200 keV.

45 μm Parallelograms, CVD of 93% $^{10}\text{B}_4\text{C}$ ($\rho=2.52\text{ g/cm}^3$), LLD 200 keV

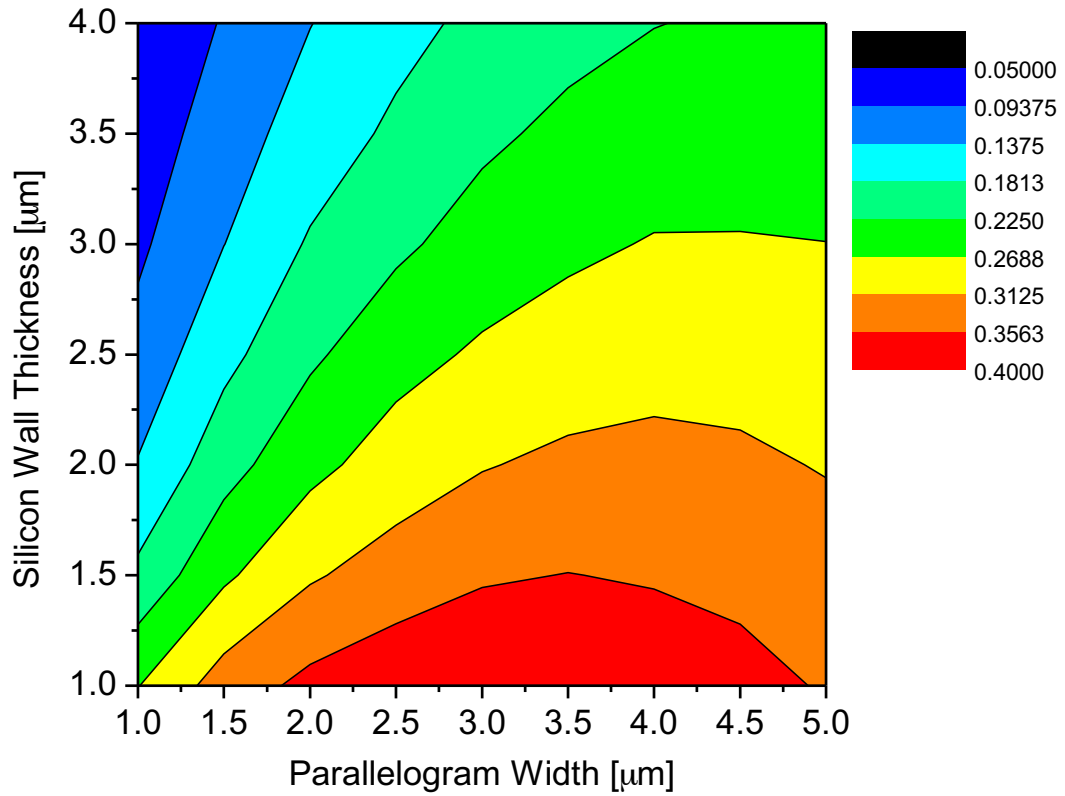


Figure 3.5: Contour plot showing the simulated thermal neutron efficiency as a function of the parallelogram width and silicon wall thickness of a 45 μm -deep parallelogram device filled via CVD of B_4C ($\rho=2.52\text{ g/cm}^3$) and an LLD of 200 keV.

45 μm Trenches, CVD of 93% ^{10}B ($\rho=2.1\text{ g/cm}^3$), LLD 500 keV

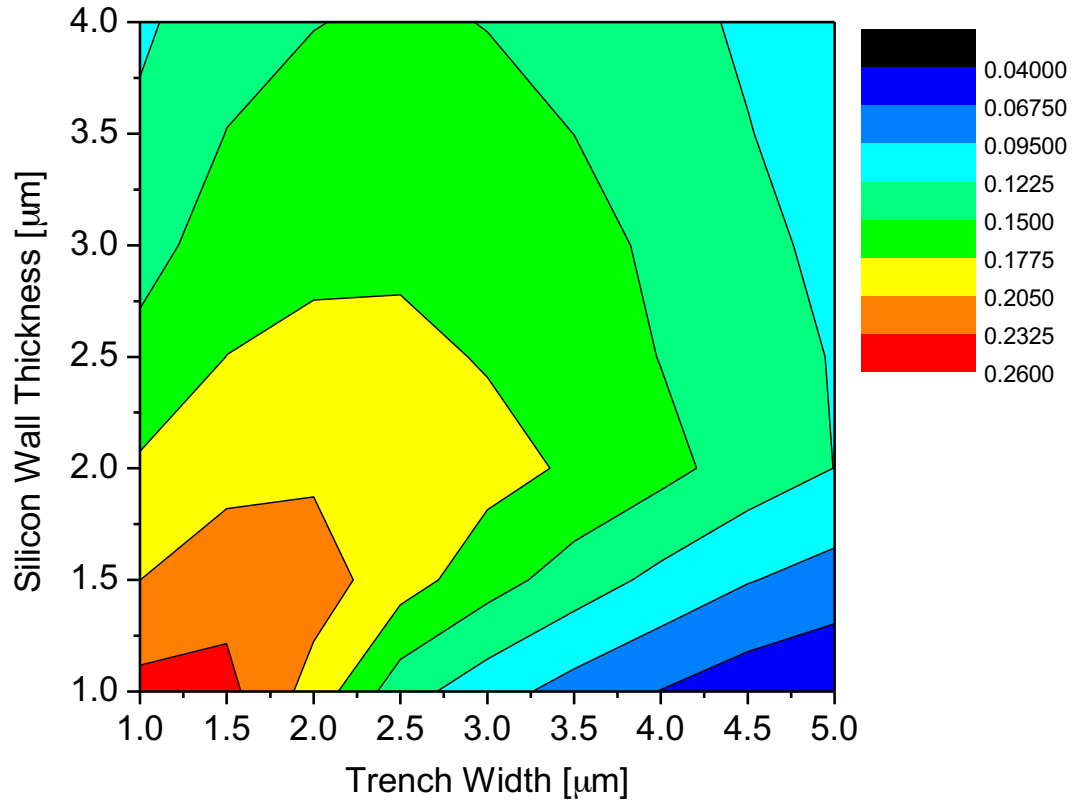


Figure 3.6: Contour plot showing the simulated thermal neutron efficiency as a function of the trench width and silicon wall thickness of a 45 μm -deep trench device filled via CVD of BN ($\rho=2.1\text{ g/cm}^3$) and an LLD of 500 keV.

The optimal efficiency of each microstructure device stems from the balance between maximizing the quantity of neutron-converting material in the device while having enough silicon for the charge particles to deposit substantial energy. For example, a trench device with thicker boron-filled trenches will absorb more neutrons due to the increased amount of ^{10}B , but fewer charged particles produced by the ^{10}B absorption reactions will escape to the Si region with enough energy to result in a detectable count. Conversely, thinner boron-filled microstructures will result in fewer neutron absorption reactions, but the charged particles that are produced will have a higher probability to escape this region and deposit enough energy in the Si region to exceed the LLD. Additionally, devices with narrower (or less dense) boron-filled microstructures will produce pulse height spectra shifted to higher energy. Therefore, the optimal, boron-filled microstructure size is a

tradeoff. Additionally, the optimal microstructure sizing tends to change as the noise level changes. For instance, if one desires a large area device with a single channel of electronics, the signal-to-noise ratio will be higher than that of a smaller device. This necessitates a higher LLD in order to reject the noise, which will lead the optimal microstructure sizing to change. In this case, thicker Si walls and narrower boron-filled microstructures are preferred. The optimal microstructure geometry can always be determined via simulation if the noise level can be predicted.

The contour plots in Appendix A were used in order to select the optimized microstructure sizing for each of the eleven devices. Table 3.1 shows the optimal dimensions for each microstructure design (with noise levels of 200 and 500 keV) and the corresponding simulated thermal neutron efficiency (corresponding to $E_n=0.0253$ eV), which were used to compare the relative performance of the aforementioned device designs. Note that the reported simulated intrinsic thermal neutron efficiency reflects the theoretical maximum efficiency achievable with an actual device. These MCNP simulations do not account for incomplete charge collection or the possibility that individual holes have a fill factor below 85%.

Table 3.1: Optimal microstructure dimensions corresponding to an isotropic thermal neutron source for various SSND designs and their associated thermal neutron efficiency ($E_n=0.0253$ eV) simulated with LLDs of 200 and 500 keV using MCNP6.1.

Microstructure	Depth [um]	Neutron-Converter and density	Optimal Microstructure and Efficiency with 200 keV LLD [%]	Optimal Microstructure and Efficiency with 500 keV LLD [%]
Honeycomb	45	CVD Boron (2.35 g/cm ³)	3.75 μm Diam. 1 μm Wall 43.4%	2.25 μm Diam. 1 μm Wall 37.3%
Honeycomb	45	CVD B ₄ C (2.52 g/gm ³)	4.25 μm Diam. 1 μm Wall 40.1%	2.25 μm Diam. 1 μm Wall 33.3%

Honeycomb	45	CVD BN (2.1 g/cm ³)	6 μm Diam. 1 μm Wall 21.2%	3.5 μm Diam. 1 μm Wall 17.1%
Parallelogram	45	CVD Boron (2.35 g/cm ³)	3 μm Width 1 μm Wall 40.7%	2 μm Width 1 μm Wall 36.7%
Parallelogram	45	CVD B ₄ C (2.52 g/cm ³)	3.5 μm Width 1 μm Wall 39.4%	2 μm Width 1 μm Wall 32.7%
Parallelogram	45	CVD BN (2.1 g/cm ³)	4.5 μm Width 1 μm Wall 27.3%	2.5 μm Width 1 μm Wall 21.7%
Trench	45	CVD Boron (2.35 g/cm ³)	1 μm Trench, 1 μm Wall 40.7%	1 μm Trench, 1 μm Wall 38.2%
Trench	45	CVD B ₄ C (2.52 g/cm ³)	1 μm Trench, 1 μm Wall 37.6%	1 μm Trench 1 μm Wall 35.1%
Trench	45	CVD BN (2.1 g/cm ³)	2 μm Trench 1 μm Wall 26.7%	1 μm Trench 1 μm Wall 24.1%
Trench	70	Boron Nanoparticles (0.7 g/cm ³)	2.5 μm Trench 1 μm Wall 34.7%	2.5 μm Trench 1 μm Wall 33.2%
Trench	70	B ₄ C Nanoparticles (0.7 g/cm ³)	3 μm Trench 1 μm Wall 30.3%	2.5 μm Trench 1 μm Wall 28.9%

3.1.1 Recommendations for the Future Development of SSNDs

The data in Table 3.1 provide a lot of useful information for the future design of microstructured SSNDs at RPI. Firstly, microstructured devices filled via CVD of enriched ¹⁰B_N results in a significantly lower efficiency than the CVD of enriched ¹⁰B₄C or enriched boron. This is expected because nitrogen atoms, which make up half of the atomic abundance in BN, do not contribute to the conversion of neutrons into ionizing particles; they do—however—contribute to the attenuation of the daughter products

produced by ^{10}B neutron absorption. Similarly, carbon atoms make up 1/5 of the atomic abundance in B_4C but do not contribute to the neutron-conversion process. As expected, B_4C -filled devices have a higher efficiency than BN-filled devices but have a slightly lower efficiency than devices filled with pure boron. These results also make sense when the efficiency is compared to the boron densities of these three materials. CVD boron results in a boron density of 2.35 g/cm^3 , CVD B_4C ($\rho=2.52 \text{ g/cm}^3$) results in a boron density of 1.99 g/cm^3 , and CVD BN ($\rho=2.1 \text{ g/cm}^3$) results in a boron density of 0.94 g/cm^3 . Therefore, BN has limited promise as a neutron-converting within microstructured SSNDs due to its relatively low boron density. Instead, pure boron should be used, which can be substituted for B_4C with a small loss in efficiency.

Additionally, the honeycomb microstructure leads to a slightly higher efficiency than the parallelogram and trench microstructure. Since the parallelogram and honeycomb designs use similar fabrication techniques, the honeycomb pattern is preferred for the future development of SSNDs. Since the performance of these simulations, it was determined that trench microstructures filled via CVD are prone to cracking. The CVD process tends to stress the long and narrow Si walls, which tends to break them. Therefore, thicker walls (approximately $> 2 \text{ }\mu\text{m}$) are required for trench microstructures filled via CVD, which limits the detection efficiency. For this reason, the honeycomb devices are preferred if CVD is chosen as the deposition method.

Although the deeper ($\sim 70 \text{ }\mu\text{m}$) trench devices filled with boron (and B_4C) nanoparticles achieve a lower efficiency than the CVD honeycomb devices, these devices show promise for the future development of inexpensive SSNDs. The deep trench microstructures are etched via wet chemical processes, which are more cost effective and significantly simpler than the photolithography processing required to etch the honeycomb and parallelogram structures. Additionally, the vacuum filling process used to inset the nanoparticles into the trenches with a width $> 3.5 \text{ }\mu\text{m}$ was demonstrated sufficiently and consistently on a simple laboratory bench. This filling method—compared to CVD—is a significantly more cost effective. The nanoparticle filling process also imparts less stress upon the thin Si walls than CVD.

A detailed fabrication process used to create microstructured trench devices filled with nanoparticles was outlined on page 14. Since the fabrication process corresponding to these nanoparticle-filled trench microstructure SSNDs is simple, cost-effective, repeatable, and results in a competitive intrinsic thermal neutron efficiency, this device type was recommended for the future development of microstructured SSNDs at RPI. Hence, a number of nanoparticle-filled trench microstructure devices were fabricated and tested at RPI with variable trench depths, widths, and wet chemical etching methods.

3.2 Predicting Pulse Height Spectra Using MCNP

During microstructured SSNDs testing, data is collected in the form of a pulse height spectrum—which is a histogram of pulse heights. The individual pulse heights are proportional to the amount of charge deposited by individual events. The shape of the pulse height spectrum is highly dependent on the microstructure geometry, microstructure sizing, device capacitance, the preamplifier used, the integration time of the shaping amplifier, and the overall quality of the charge collection.

MCNP simulations were performed in order to model the pulse height spectra of two microstructured SSND types: the honeycomb device filled with boron via CVD and the deep trench device filled with boron nanoparticles. These simulations are similar to the previous simulations used to determine the detection efficiency, which simply tallied the number of pulses above the predetermined LLD. Simulating a pulse height spectrum—on the other hand—requires tallying the charged particle deposition in the Si region with small, incremental energy bins. Therefore, the F8 tally used to track individual events was broken down into 100 equally spaced energy bins from zero to 3.5 MeV. An example of an MCNP input used to simulate the pulse height spectrum of an enriched boron-filled honeycomb device with 3 μm hexagonal holes, 1 μm Si walls, and a fill factor of 85% is shown in Appendix C. Similarly, an MCNP input used to simulate the pulse height spectrum of an enriched boron nanoparticle-filled trench device with 5 μm hexagonal holes, 3 μm Si walls, and a fill density of 0.7 g/cm³ is shown in Appendix D. These simulations incorporated a moderated ²⁵²Cf fission neutron source instead of the monoenergetic 0.0253 eV neutron source used in the previous simulations. This neutron

spectrum—which more accurately represented the experimental conditions—was modeled as an evaporation spectrum shown by equation 5.

$$p(E) = CE \exp\left(-\frac{E}{0.033 \times 10^{-6} \text{ MeV}}\right) \quad (5)$$

This spectrum was determined by simulating the ^{252}Cf fission neutron source within the moderator housing, tallying the neutron spectrum at the detector location, and fitting an exponential curve to the data. Using this evaporation spectrum in equation 5—as opposed to modeling the fission neutrons and moderation process—significantly reduced the simulation time. This neutron spectrum was simulated as an isotropic point source above the device. The charged particle deposition in the Si region was tallied in the bin corresponding to the energy deposited. A histogram of these events was created in order to produce a simulated pulse height spectrum corresponding to the appropriate device.

The simulated pulse height spectra of the honeycomb device demonstrated good agreement with the experimentally collected pulse height spectra. However, the agreement between the simulated and experimental spectra of the trench device shows poorer agreement; there were a number of challenges associated with this modeling that will be discussed in the subsequent sections. Overall, these comparisons demonstrate that the MCNP simulations are accurately modeling the nuclear reactions and charged particle deposition in the detectors. The ability to simulate the pulse height spectra also demonstrates that the phenomenon leading to individual detection events are well understood.

3.2.1 Simulating the Honeycomb SSND Pulse Height Spectra

One of the challenges associated with the simulation of the pulse height spectra corresponding to the aforementioned honeycomb SSNDs was modeling the subtle contour and shape of the high aspect ratio microstructures, as well as the conformity of the neutron converter filling. MCNP inputs are created using simple geometric shapes, so the simulations utilize ideal geometries with etched angles normal (perpendicular) to the face. In reality, the etching process can etch the sidewalls—especially when the microstructures

are deeper—resulting in microstructures that have a subtle contour. Additionally, the boron filling process is not necessarily homogeneous. In fact, necking at the top of some holes can lead to clogging before the filling process is complete. A cross-sectional and top-view representing a simulated honeycomb microstructured device with a hexagonal diameter of $3\mu\text{m}$, a Si wall thickness of $1\mu\text{m}$, and a fill factor of 85% can be seen in Figure 3.7. The blue region represents air outside of the device, the red region is the charge-collecting Si substrate, the green region represents the boron, and the white region is the central void modeling the incomplete fill. These snapshots from Visual Editor can be compared to SEM images of an actual honeycomb device in Figure 3.8. The cross-sectional image on the left-hand side of Figure 3.8 depicts the contour of the deep hexagonal holes and the necking at the top. From this image, it is difficult to determine the fill factor within the holes.

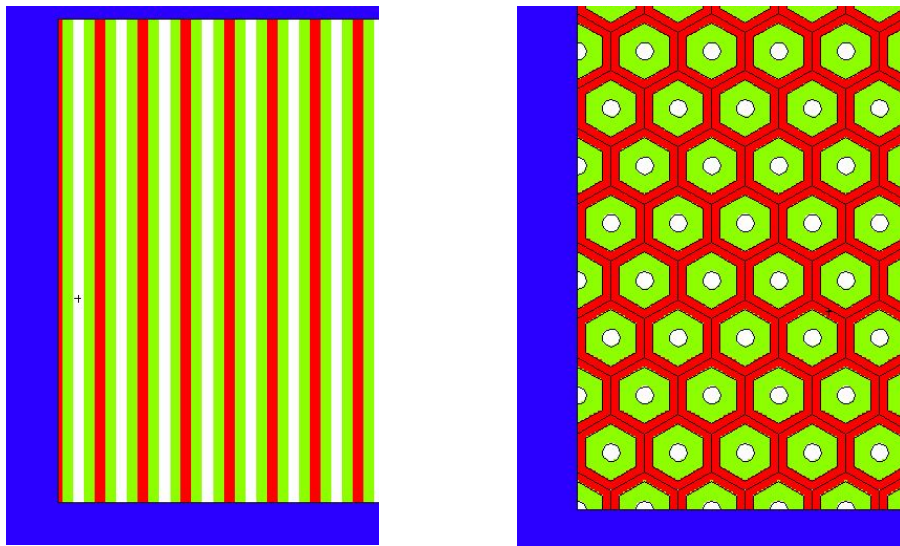


Figure 3.7: Cross-sectional view (left) and top view (right) of an MCNP-simulated honeycomb device used to model the neutron pulse height spectrum.

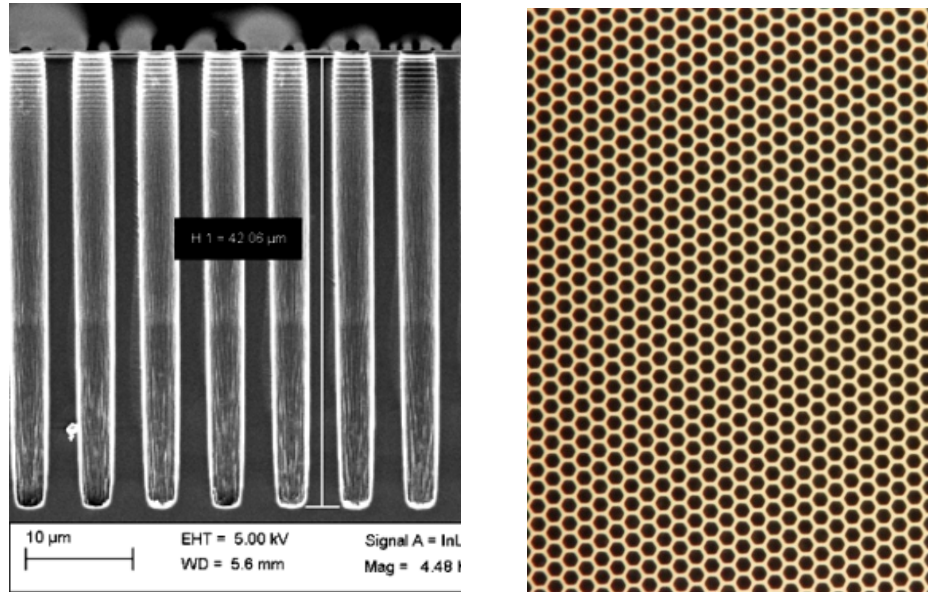


Figure 3.8: Cross-sectional view (left) and top view (right) of a honeycomb device taken with a microscope.

Figure 3.9 depicts the normalized experimental neutron pulse height spectrum of a honeycomb device with the microstructure geometry shown in Figure 3.8. This honeycomb device has a nominal hexagonal diameter of $3.0 \mu\text{m}$ and Si walls of $1 \mu\text{m}$.

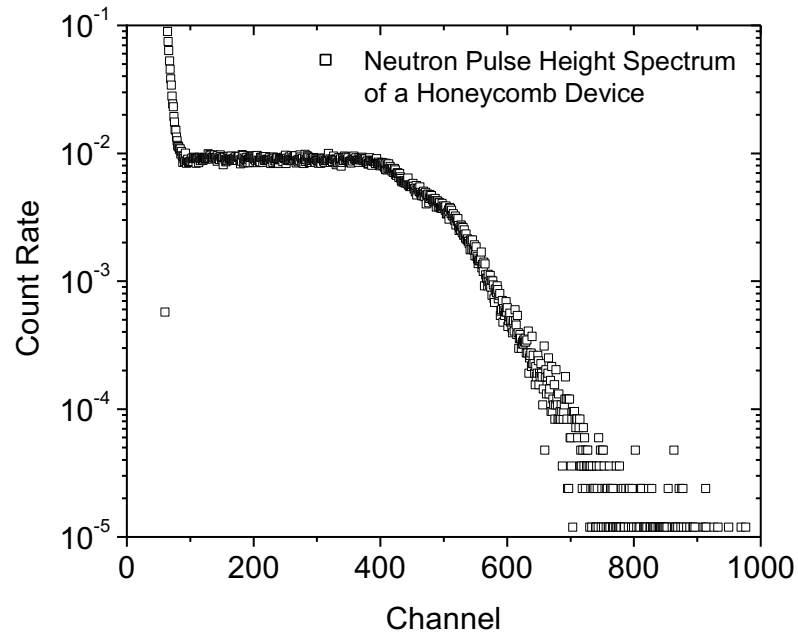


Figure 3.9: Experimentally-collected neutron pulse height spectrum of a honeycomb device. The measurement was performed with a moderated ^{252}Cf source using a custom preamplifier.

Since the MCNP simulations are composed of a repeated lattice with hundreds of thousands of holes, modeling realistic geometries quickly becomes complicated. Additionally, MCNP is unable to model the curved contour of the etched microstructures and deposited boron. Therefore, multiple simulations with incremental hexagonal diameters were used. Since pulse height spectra are produced by tallying the amplitude of individual events, the creation of an aggregate pulse height spectrum by summing the individual and incremental device geometries seems like a good approximation and substitute for a single simulation that incorporates the subtle contour and tapered geometry of the etched microstructures.

Each simulation assumed a constant unit cell pitch—defined as the hexagonal diameter plus the Si wall width—of $4\ \mu\text{m}$. The diameter of the hexagonal hole was varied from $1\ \mu\text{m}$ (with a Si wall of $3\ \mu\text{m}$) to a hole diameter of $3\ \mu\text{m}$ (with a Si wall of $1\ \mu\text{m}$) by increments of $0.25\ \mu\text{m}$. Additionally, each simulation was performed with a fill factor of

40%, 55%, 70%, 85%, and 100%. A pulse height spectrum was tallied for each of the 45 simulated honeycomb device combinations. Figure 3.10 and Figure 3.11 show select MCNP-simulated pulse height spectra corresponding to honeycomb devices with variable microstructure dimensions and a fill factor of 100% and 55%, respectively. These spectra have significantly different shapes, and—as mentioned previously—detectors with narrower hexagonal holes and wider Si walls have pulse height spectra that are shift higher in energy. Again, these sets of simulations were performed in order to mimic the subtle contour of the microstructures using simulations with simplified geometries.

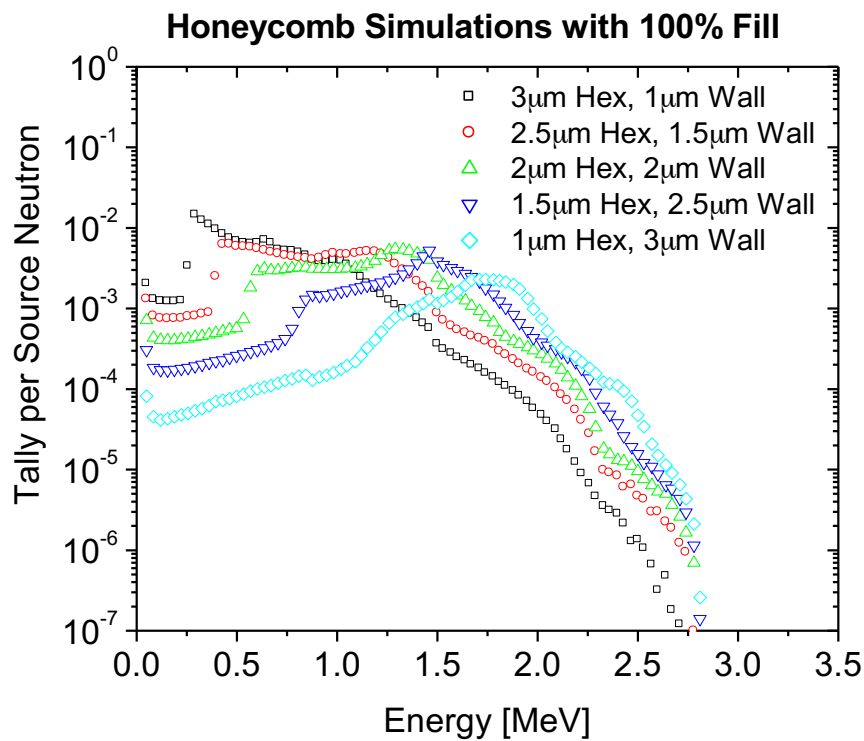


Figure 3.10: MCNP-simulated pulse height spectra for enriched ¹⁰B-filled honeycomb devices with variable hexagonal sizes and a fill factor of 100%.

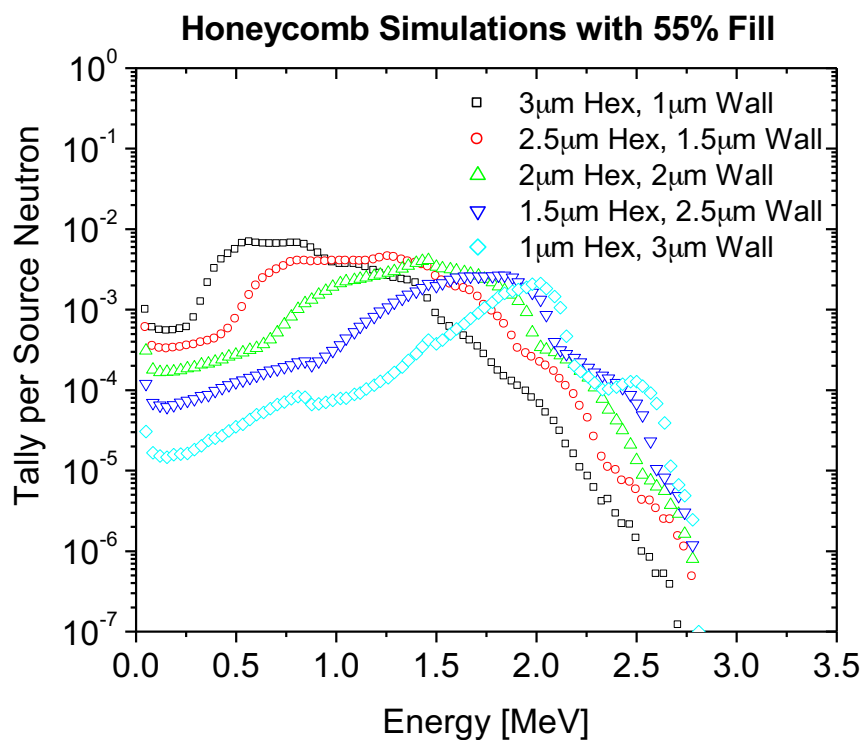


Figure 3.11: MCNP-simulated pulse height spectra for enriched ^{10}B -filled honeycomb devices with variable hexagonal sizes and a fill factor of 55%.

A representative pulse height spectrum was created by combining these individual simulated responses in order to represent the response of a device with a realistic microstructure geometry. Multiple steps were taken in order to compare the shape of the experimentally collected pulse height spectrum (shown in Figure 3.9) with the combination of the 30 aforementioned simulations. First, the x-axis of the experimental spectrum (channel number) was calibrated to energy [MeV]. This calibration was performed by lining up the identifiable peaks of the simulated and experimental spectra corresponding to individual daughter products of ^{10}B neutron absorption. This calibration factor is dependent on the MCA settings and the gain of the preamplifier and shaping amplifier. Additionally, the magnitude of the experimental spectrum (y-axis) was arbitrarily normalized to the simulated spectra. Next, a least square regression was performed on the 30 simulated spectra in order to find the best match with the

experimentally collected pulse height spectrum. The regression provided a coefficient for each simulated pulse height spectrum. The sum of the coefficients was normalized to unity, and an effective pulse height spectrum was created by summing the individual spectra, weighted by the associated coefficients. The table in Appendix E shows the coefficients for each of the 30 simulations used to create the simulated spectrum. These coefficients will be revisited later, as they will help to develop a single MCNP simulation with tapered microstructures, despite the previously mentioned difficulties.

The resulting spectrum represents a device with hexagonal holes that vary in both width and the conformity of the boron deposition based on the aforementioned coefficients shown in Appendix E. This aggregation of simulations was compared to an experimentally-collected pulse height spectrum of a honeycomb device when exposed to a moderated neutron source. As expected, the combination of the incremental simulated responses with variable fill factors results in significantly better agreement with the experimental pulse height spectra than a single microstructure simulation. Figure 3.12 shows the resulting excellent agreement between the experimental neutron pulse height spectra and the aforementioned simulated spectra.

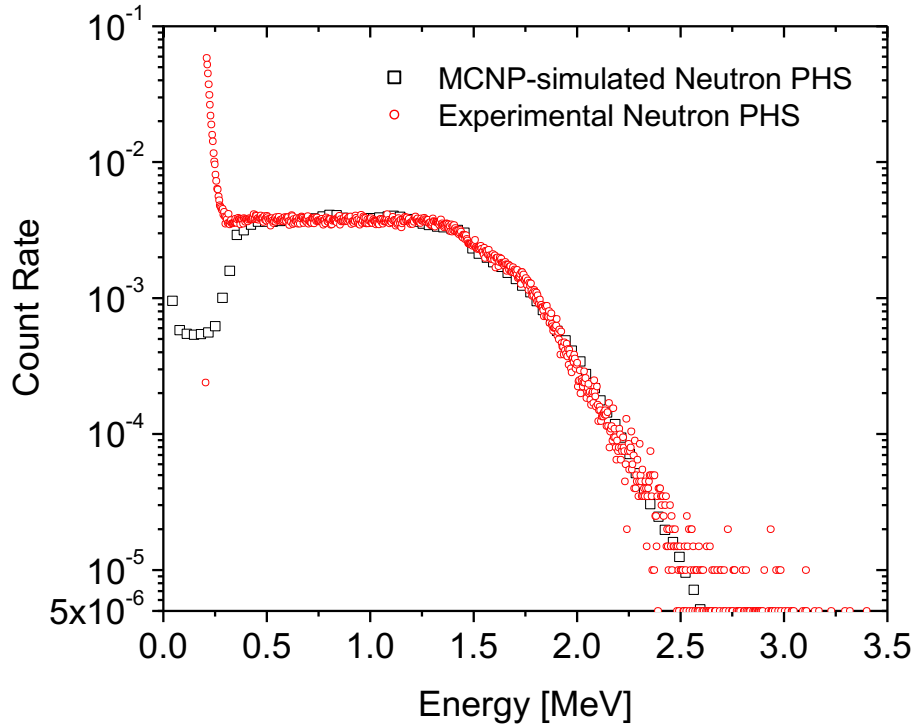


Figure 3.12: Comparison of an experimentally collected and an aggregate, simulated neutron pulse height spectrum of a honeycomb SSND demonstrating good agreement.

The disagreement at low energies ($E < 0.3$ MeV) arises from electronic noise in the experimental spectrum that is not modeled in the simulations. Additionally, the discrepancies corresponding to large pulse heights ($E > 2.5$ MeV) is due to the pile up of multiple pulses that effectively arrive simultaneously during experimental data collection. Since the MCNP simulations are performed one neutron at a time, there is no pulse pileup in the simulated pulse height spectra. Otherwise, the summation of the normalized simulated spectra demonstrates excellent agreement with the normalized experimentally collect pulse height spectrum.

Despite the assertion that combining multiple simulations in order to produce a pulse height spectrum is an acceptable method, the creation of a single simulation to represent the honeycomb device is understandably preferred. Due to the limited macrobody geometries available in MCNP, this simulation used tapered cylindrical holes in a hexagonal lattice to substitute the honeycomb microstructure. This is a reasonable

substitute since the etched hexagonal holes of the fabricated devices are rounded due to imperfect photolithography. The simulated geometry of the representative honeycomb microstructure was determined using the SEM image of the etched device (shown in Figure 2.1) and aforementioned coefficients—which were determined via least squares regression in Appendix E—as a guide. For example, SEM image shows that the holes don't begin to taper (become narrower) until a depth $>20\text{-}25\ \mu\text{m}$. This is also reflected by the coefficients in Appendix E; the simulations with a hexagonal diameter of $3\ \mu\text{m}$ are weighted more significantly than the simulations with narrower holes. After studying the SEM images and coefficients, a single simulation was created to model the pulse height spectrum of a honeycomb device. The hole depth was $45\ \mu\text{m}$, the diameter at the top of the device was set to $3.25\ \mu\text{m}$, and the hole diameter at the bottom of the device was $1.5\ \mu\text{m}$. A central void with a diameter of $0.98\ \mu\text{m}$ was modeled at the center of each hole to simulate the incomplete boron filling. The same isotropic thermal neutron source and pulse height tally was simulated above the center of the device. Two diagrams (a cross-sectional and top view) of the MCNP-simulated device can be seen in Figure 3.13. The green region is the deposited boron, the red region is the Si substrate, and the white region is void.

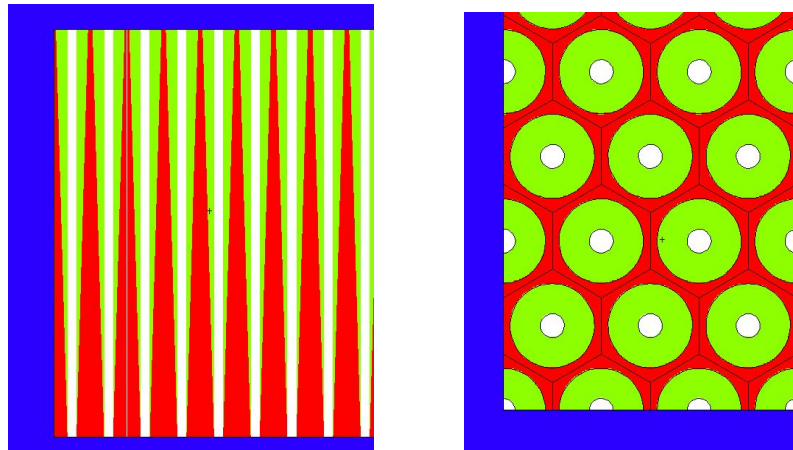


Figure 3.13: Cross-sectional view (left) and top view (right) of the simulated honeycomb device using tapered cylinders in order to predict the shape of a honeycomb device pulse height spectrum.

The resulting tallied pulse height spectrum provides good agreement with the experimental spectrum; this comparison can be seen in Figure 3.14. The discrepancy at

lower energies between 0.3 and 0.5 MeV is likely caused by the simplified geometries coded in the MCNP input, which don't perfectly model reality. Overall, these successful comparisons between experimental and simulated pulse height spectra of the honeycomb devices demonstrate that the underlying phenomenon are well understood and are accurately modeled by the MCNP simulations. Therefore, MCNP simulations were used as benchmarks for experimental measurements throughout the scope of this project.

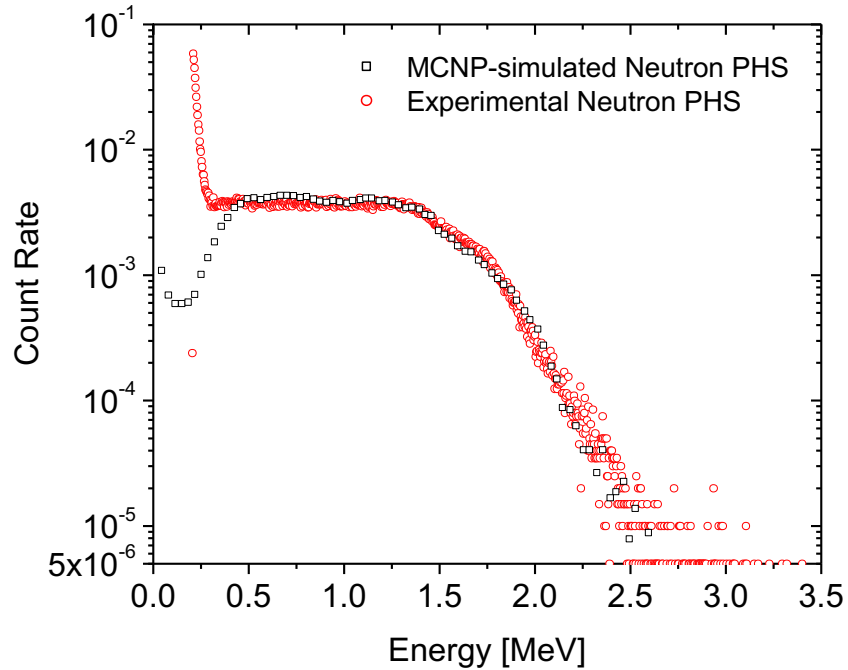


Figure 3.14: Comparison of an experimentally collected honeycomb neutron pulse height spectrum and the MCNP-simulated pulse height spectrum of a single SSND with tapered cylinders in a hexagonal lattice.

3.2.2 Simulating the Trench SSND Pulse Height Spectra

Similarly, MCNP simulations were used in order to predict the shape of a pulse height spectrum collected with the nanoparticle-filled trench microstructure SSNDs. As mentioned, the geometry and sizing of the microstructure affects the distribution of pulse heights produced via charged particle collection in the Si. Therefore, it is expected that these trench devices will result in different pulse height spectra than their honeycomb counterparts. In fact, since the nanoparticle deposition results in a lower fill density than CVD, the trench pulse height spectra shows interesting characteristics that can be related

to the individual alpha and Li ion energies produced by ^{10}B absorption. Figure 3.15 shows a pulse height spectrum corresponding to a background measurement and a moderated neutron measurement, which was labeled in order to connect the identifiable characteristics of the pulse height spectrum to the individual daughter products of the ^{10}B neutron absorption reactions. This device—named T52—was fabricated with a trench width of approximately $5\ \mu\text{m}$, Si walls of $3\ \mu\text{m}$, a depth of $65\text{-}70\ \mu\text{m}$, and an active area of $2.5\times 2.5\text{mm}^2$.

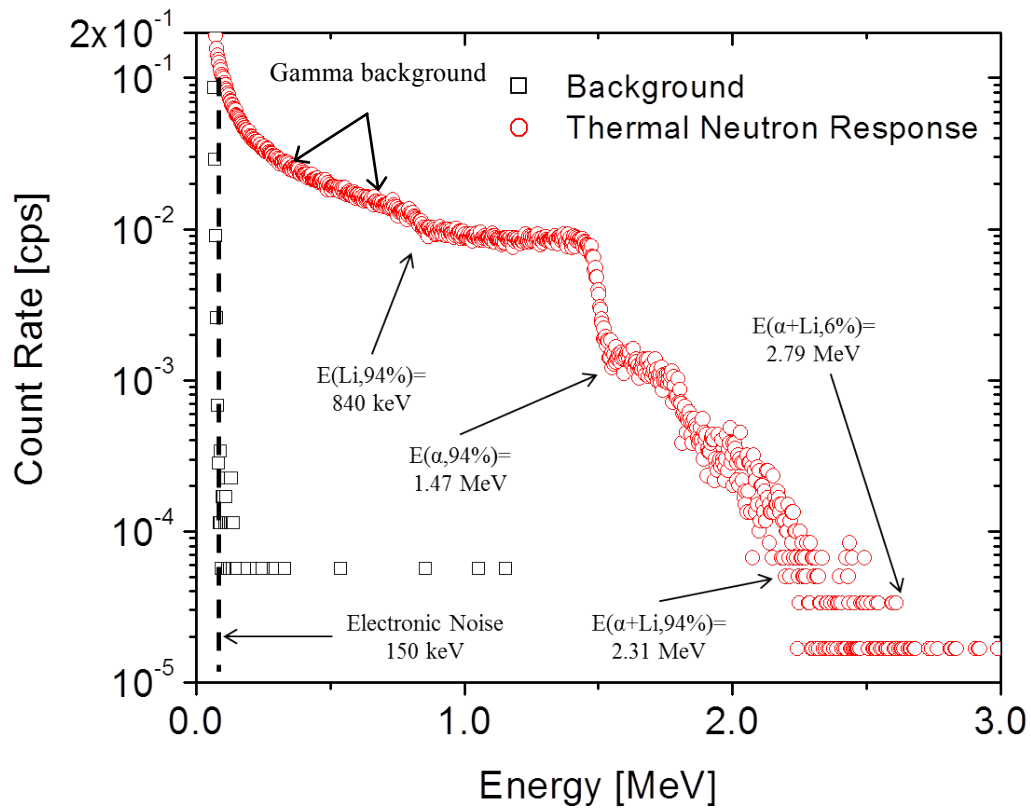


Figure 3.15: Labeled experimental pulse height spectra collected with the trench microstructured SSNDs T52 (Area= $2.5 \times 2.5\ \text{mm}^2$). This measurement was collected with zero bias, a custom preamplifier, an ORTEC shaping amplifier with a gain of 8 and an integration time of $12\ \mu\text{s}$.

Again, an SEM image of a trench device filled with enriched boron nanoparticles can be seen in Figure 2.6. The heterogeneity of the fill makes it difficult for the aforementioned, elementary MCNP simulations to predict the shape of the pulse height spectrum.

Nonetheless, a set of MCNP inputs was created in a similar manner as the previous honeycomb simulations. The trench microstructure simulations use the same isotropic thermal neutron source spectrum, device area, and detector tallies. The microstructured trench simulations were created by varying the trench width and the Si wall width, while maintaining a constant pitch (trench + Si wall width) of 8 μm . The fill density of the 96% enriched ^{10}B nanoparticles was varied from 0.6 μm to 0.9 μm by 0.1 μm in order to attempt to account for heterogeneity of the fill. Select simulated neutron pulse height spectra corresponding trench widths of 4-6 μm with a homogeneous fill density of 0.6 g/cm^3 can be seen in Figure 3.16. Similarly, pulse height spectra corresponding to the same trench widths (4-6 μm) with a fill density of 0.8 g/cm^3 can be seen in Figure 3.17.

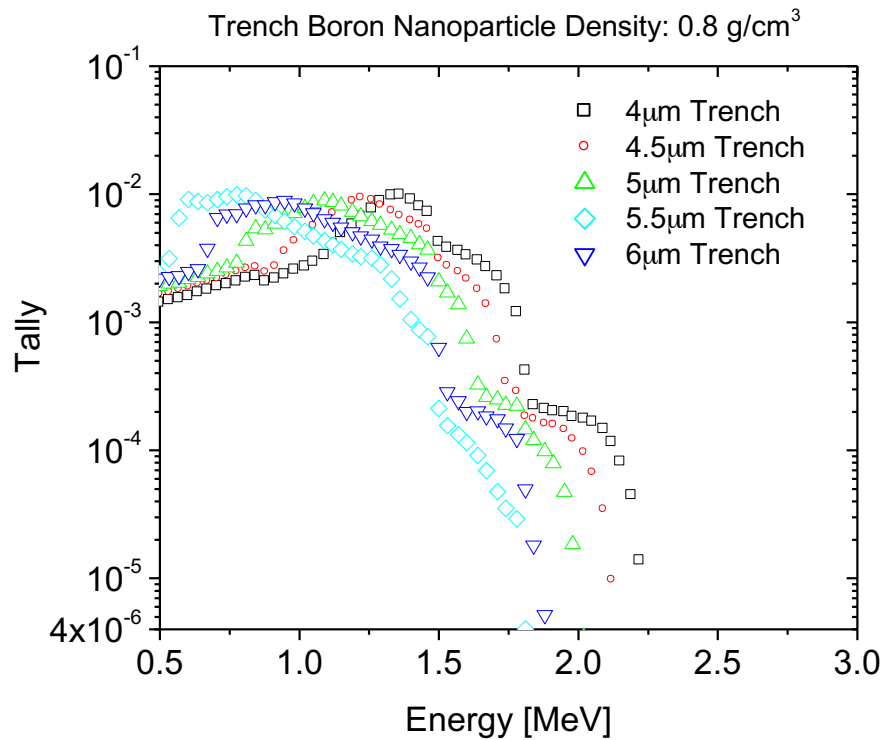


Figure 3.16: MCNP-simulated thermal neutron pulse height spectra corresponding to a trench microstructured device with variable trench thicknesses (4-6 μm), a pitch of 8 μm , and a nanoparticle density of 0.6 g/cm^3 .

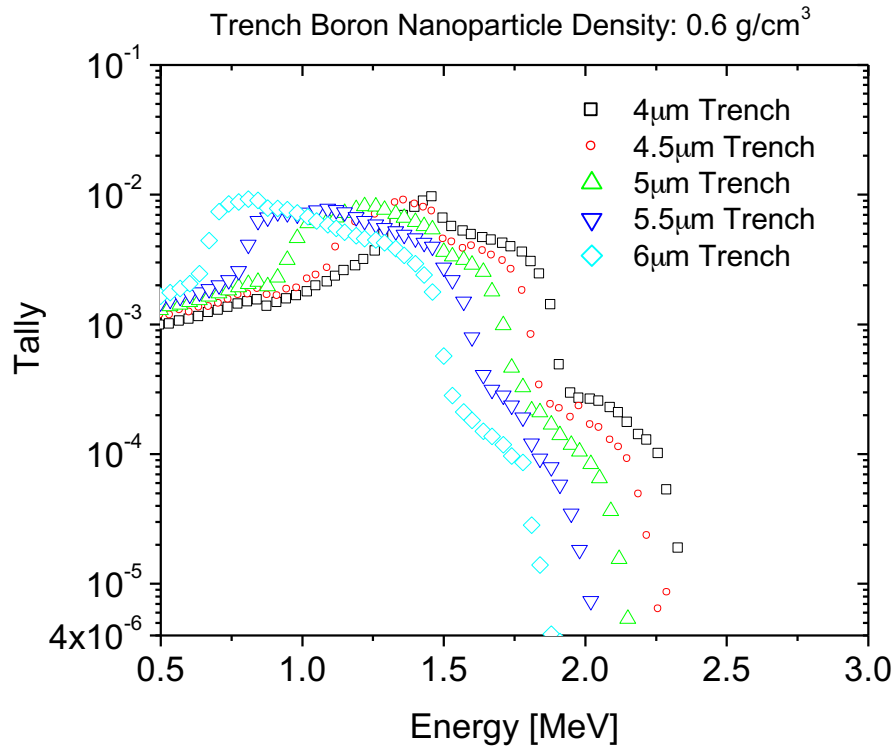


Figure 3.17: MCNP-simulated thermal neutron pulse height spectra corresponding to a trench microstructured device with variable trench thicknesses (4-6 μm), a pitch of 8 μm , and a nanoparticle density of 0.8 g/cm^3 .

The individual simulations—a selection of which are shown in Figure 3.16 and Figure 3.17—show some of the same features as the experiment spectrum in Figure 3.15; however, one can tell that these individual simulations demonstrate poor agreement with the experimental spectrum before they are even directly compared. Since the actual trench device has slightly tapered microstructures and a very heterogeneous fill, a linear combination of these responses with different trench widths and fill densities was created in order to improve the agreement with the experimental pulse height spectrum. The low energy region ($E < 1$ MeV) was ignored for this fit, since the experimental spectrum has electronic noise and—more significantly—gamma background in this region. The best agreement that was obtained using a combination of MCNP simulations with trench widths from 4-6 μm , a pitch of 8 μm , and a density of 0.6-0.9 g/cm^3 can be seen in Figure

3.18. The MCNP-simulated PHS certainly does not match the experimental PHS perfectly, but there are similarities. The limited agreement is likely due to the limitations of the MCNP simulations; for example, the simulations cannot model the boron nanoparticle fill realistically as a heterogeneous medium.

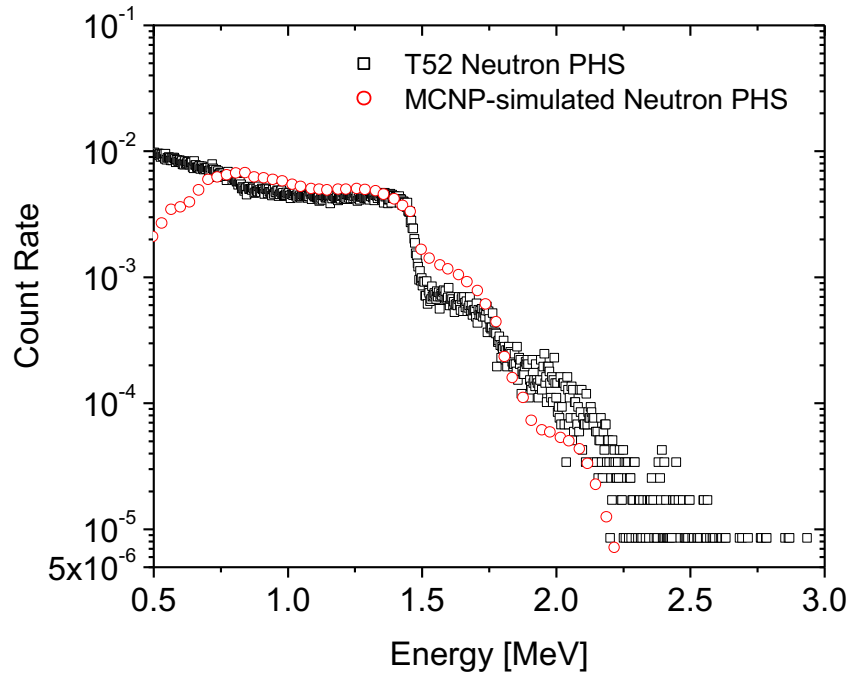


Figure 3.18: Comparison of an experimentally collected pulse height spectrum of trench device T52 and an MCNP-simulated neutron pulse height spectrum created from of an aggregate of simulations using least squares regression.

Lastly, a single MCNP simulation was used to model the pulse height spectrum of device T52. The simulation was created using tapered trenches with a minimum width of $5 \mu\text{m}$ ($3 \mu\text{m}$ Si walls), a maximum width of $6 \mu\text{m}$ ($2 \mu\text{m}$ Si walls), and a depth of $70 \mu\text{m}$. Again, the isotropic thermal neutron source was centered above the top of the device, and the charged particle deposition in the Si region was collected using an F8 tally. The boron nanoparticles were modeled as a heterogeneous fill with a density of 0.7 g/cm^3 . The resulting comparison can be seen in Figure 3.19.

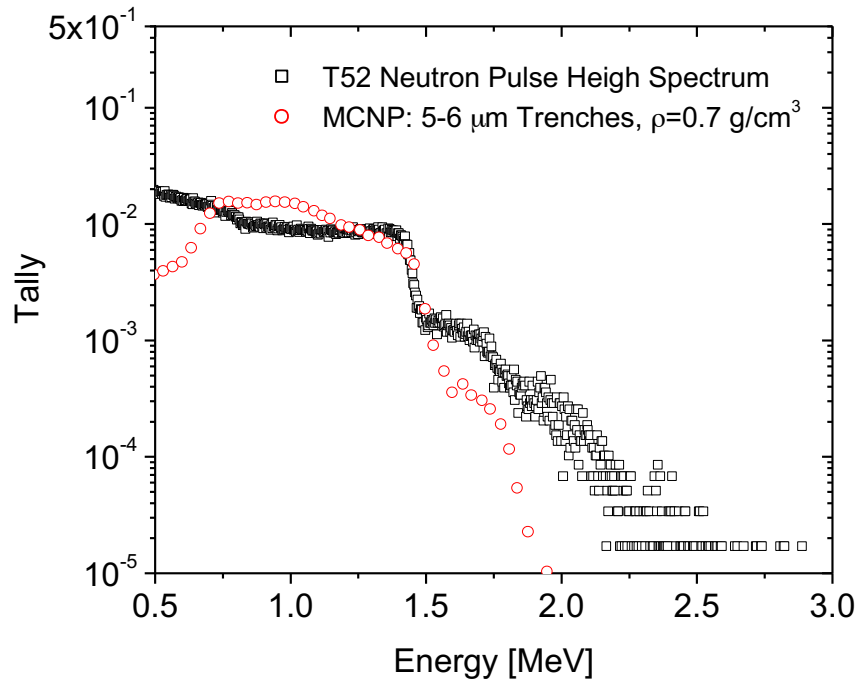


Figure 3.19: Comparison of an experimentally collected neutron pulse height spectrum (device T52) and the MCNP-simulated pulse height spectrum of a single device with tapered trenches.

First of all, the lack of agreement at lower energy ($E < 0.75$ MeV) primarily comes from the electronic noise and the elevated gamma response of the trench device T52. Since the trench devices are deeper than their honeycomb counterparts, the layer of parasitic Si is also thicker. The thicker layer of sensitive Si substrate increases the response to these unwanted gammas. In fact, the active Si substrate of device T52 is approximately $200 \mu\text{m}$ thick, which is approximately three times that of the honeycomb devices. Fabricators are confident that these trench devices can be thinned down at the end of the fabrication process, which would significantly reduce the gamma sensitivity.

Overall, the MCNP-simulated pulse height spectrum of the nanoparticle-filled trench device has significantly worse agreement with the experimental spectrum than the honeycomb devices filled via CVD. The poor agreement at intermediate and higher energies ($E > 0.75$ MeV) is likely due to the heterogeneous nature of the boron nanoparticle

filling. Unlike the simulations, the nanoparticle-filled trenches are not homogeneous. This heterogeneous nature of the neutron converting material is likely having a significant effect on the attenuation of the charged particles produced in this region, which would affect the shape of the pulse height spectrum. For example, Figure 2.6 shows that some trenches are more completely filled than others. Similarly, each trench has some regions with a high density of boron nanoparticles and other regions with a low effective density of nanoparticles. Unfortunately, MCNP doesn't allow for the same region (cell) to have variable density, so the trenches are modeled with a single, homogeneous density. The simplicity of the simulations plays a role in the ability to achieve good agreement. This hypothesis is strengthened by the ability to achieve better agreement with the devices filled via CVD because this method of filling results in a denser, more homogeneous layer of neutron converting material. If a simulation were able to realistically model the nanoparticle distribution within the trenches, the agreement would likely be improved significantly.

3.3 Microstructure Customization for Versatile Detection Systems

The benchmarked MCNP simulations provide information about the pulse height shape and relative efficiencies of various microstructure designs. This information was used in order to optimize the design of many devices. A primary consideration for the microstructure design is the detector system's noise level. The detector noise level is measured once the device is fabricated, connected to the appropriate nuclear instrumentation, and measured on an analog or digital readout. Since connecting more devices in series increases the device capacitance leading to a degraded signal-to-noise ratio, the noise level of the device will generally be proportional to the detector area. Therefore, neutron detector applications requiring large area detectors will need a higher LLD. Note, custom preamplifiers can reduce this impact and the magnitude of amplification does not affect the noise level because the radiation signal will increase by the same factor. Additionally, elevated gamma fields (>100 mR/hr) can elevate the background level, requiring a higher LLD. These factors affect the LLD necessary to discriminate unwanted events from neutron interactions, which unavoidably cuts a fraction of neutron events. The simulations of the SSND pulse height spectra demonstrate

the distribution of pulse heights for various microstructure geometries. Referencing Figure 3.10 and Figure 3.11, notice that the microstructures with thicker honeycomb holes have more low-energy pulses, and microstructures with thinner holes (and thicker walls) have more high-energy pulses, relatively speaking. Therefore, the microstructure geometry can be optimized for various noise levels (LLDs). Optimizing device microstructures for higher LLDs allows for detectors to be scaled to larger areas. This reduces the number of nuclear instrumentation channels and the overall system cost.

The honeycomb and trench microstructure detectors demonstrated low noise levels (~ 200 keV) with appropriate amplifiers and a small area configuration (< 4 cm²). Again, this noise level depends on the solid-state wafer properties, device fabrication procedures, detector area, preamplifier properties, etc. Scaling the honeycomb and trench SSNDs to larger areas (4-16 cm²) resulted in noise levels closer to 500 keV. The detector microstructures were optimized for these two detector noise levels (200 and 500 keV), which make the detector performance more competitive. The simulated detector efficiencies used to optimize the detectors for various detector applications (areas) are shown in Appendix A.

3.4 Homogeneous SSND Simulation

Hexagonal boron nitride devices were also simulated using MCNP6.1 in order to compare the simulated pulse height tally to hBN device responses. Since homogeneous devices utilize the same material, e.g. hBN, as the neutron-converting material and charge-collecting medium, there is potential for complete charge deposition and collection of the two daughter ions produced by ¹⁰B capture (Equation (1)). Therefore, individual pulses collected by a homogeneous SSND can have higher amplitude, reducing the negative impact of elevated electronic noise on the detector efficiency. Hypothetically, peaks in the pulse height spectrum corresponding with the energy of the thermal neutron absorption reactions would be resolvable if the solid-state substrate has substantial thickness and ideal charge collection. A MCNP simulation of a slab of hBN (10 μ m x 80 μ m x 2 mm) was performed in order to simulate the pulse height spectrum of such a device with an ideal

charge collection (Figure 3.20). The structure of the simulated pulse height spectrum is labeled with the corresponding daughter products (see Equation (1)).

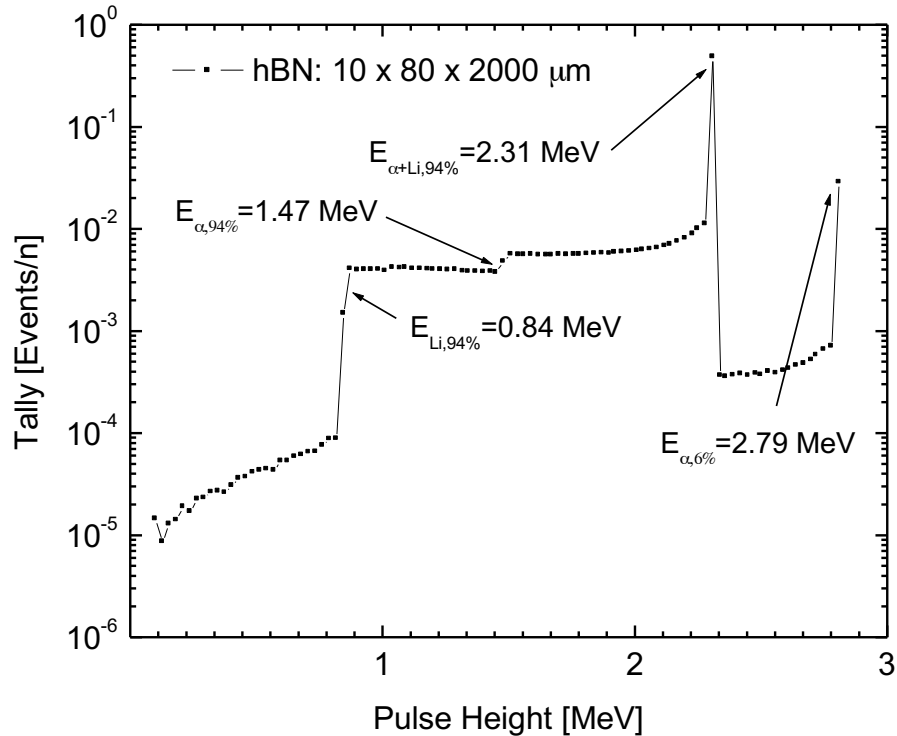


Figure 3.20: Simulated pulse height tally of an hBN slab with a thickness of 10 μm and ideal charge collection.

In reality, growing high-quality hBN crystals is a very difficult challenge, and charge collection far from ideal. In fact, it is hypothesized that significant charge trapping in the hBN crystals due to imperfections has a significant, negative impact on the charge collection. Additionally, each SSND has a finite device capacitance and resistance. Therefore, the amplitude of each event will be affected by the area of the device, the localization of the charge deposition, and the intrinsic device properties—i.e. resistance and capacitance. Devices must be fabricated carefully and precisely because charge conducting on a slightly rough surface can lead to charge trapping. The overall effect is a spreading of the pulse height spectrum, which is modeled by performing a Gaussian broadening to the simulated pulse height tally. In many hBN crystals, charge collection is poor at achievable electric field levels. A simulated pulse height tally in Figure 3.20 was broadened with a 1 MeV Gaussian and is shown in Figure 3.21 in order to

rudimentarily simulate the incomplete charge collection. This simulated pulse height spectrum does not include electronic noise or gamma response, which will significantly raise the counts in the low energy region (>1 MeV).

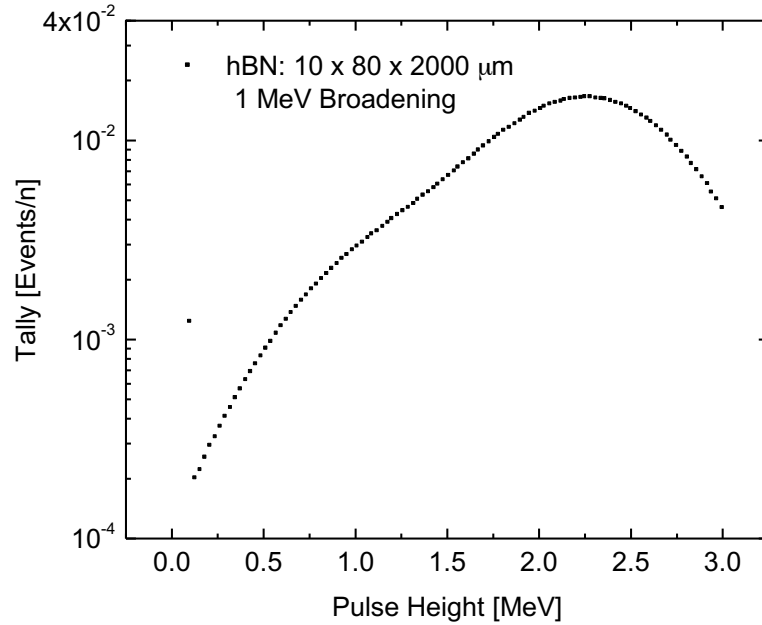


Figure 3.21: Simulated pulse height tally of an hBN slab with a thickness of $10 \mu\text{m}$ broadened by a 1 MeV Gaussian.

4. Solid-State Detector Testing at RPI

Numerous variations of detectors were tested in the Calibrated Neutron Laboratory—including the iterations of microstructured SSNDs developed at RPI. Measurements were performed in order to characterize the devices' intrinsic thermal neutron detection efficiency, gamma insensitivity, and scalability of individual devices to larger surface areas with a single channel of electronics. These properties must be measured accurately and precisely in order to determine a specific device's performance—and therefore—efficacy as a deployable neutron detector for various applications.

4.1 Neutron Detection with Solid-State Devices

The process of identifying a neutron event in a microstructured SSND begins with a nuclear reaction—e.g. thermal neutron absorption in ^{10}B —within the neutron converting region of the detector. The reaction products— α 's and Li ions—can escape to the semiconductor with high ionization energy. At this point, a microstructured SSND operates in the same way as a traditional semiconductor diode detector. Electron-hole pairs, which are the fundamental information carriers, are produced along the path of the energetic ions. The use of semiconductor materials results in a large number of carriers for a single radiation event. These electron-hole pairs can be considered analogous to the ion pairs produced in a biased, gas-filled detector [32]. Since the solid-state device has a fully depleted p-n junction, there is a large electric field where the electron-hole pairs are formed. Semiconductor diodes also have a high charge carrier velocity, so a well-designed device can have a fine timing resolution. The collection time for electron-hole pairs created in the fully depleted region of the device will be below 1 ns since the carriers only need to travel several μm . Figure 2.3 depicts the depletion region of a honeycomb SSNDs which surrounds each etched hexagonal hole. The width of this depletion region is controlled by the boron doping level and is optimized for the microstructure geometry. In this case, the depletion region thickness is approximately half of the Si wall thickness. Most of the electron-hole pairs will be produced in this region—above the depletion region edge—where collection is fast. However, some carriers can be produced below this region, where there is effectively no field. The charge collection in this region is slow, as the carriers diffuse to the junction. The timing of charge collection from events in this

region depend on the lifetime of the minority carriers. The timing of this process can take on the order of μs to ms . The migration of the electrons and holes to their respective contact produces a small current. Again, complete charge collection relies on a well-designed and fabricated device that is fully depleted with zero bias. Subsequent charge preamplification produces a pulse, which will have a time signature that heavily depends on the timing of the preamplifier. Since charge collection happens so rapidly in a well-designed semiconductor diode detector, the preamplifier and shaping amplifier typically limit the detector timing. Fast preamplifiers can generate pulses with sub- μs pulses. Slower preamplifiers, which produce a better signal, generate pulses with longer fall times—on the order of 10-100 μs . Subsequent spectroscopy amplification, pulse integration, and analog-to-digital conversion using standard nuclear instrumentation allows pulses to be recorded, individual neutron events to be identified, and a pulse height spectrum to be produced.

4.2 Development of Low-Noise Preamplifiers for RPI's SSNDs

Initially, the SSNDs developed at RPI were tested using commercially available preamplifiers and shaping amplifiers. Typically, an ORTEC 142AH, 142PC, or Cremat CR-110 preamplifier was employed in conjunction with an ORTEC 672 or Canberra Spectroscopy Amplifier. These backend electronics work well for laboratory testing; however, a major goal of this research project is the development of neutron detection systems for portable and hand-help applications. Thus, the back-end electronics should be compact, low-power, and inexpensive. Additionally, the electronics must be low-noise in order to optimize the device efficiency. The aforementioned commercial preamplifiers utilized for testing in the laboratory are not customized for the high capacitance of microstructured SSNDs developed at RPI. For example, the ORTEC 142AH preamplifier is designed to be compatible with detectors that have a capacitance in the range from zero to 100 pF [33]. Typically, the 2.5mm x 2.5 mm (6.25 mm²) microstructured SSNDs

¹This work was published in IEEE Transactions on Nuclear Science, Vol. 63, No. 1, February 2016. “Low-Noise Preamplifier Design Considerations for Large Area High Capacitance Solid-State Neutron Detectors.” E. English, A. Weltz, et al.

developed at RPI have significantly higher capacitance (~ 280 pF with zero bias voltage). A plot of the detector capacitance (area = 6.25 mm²) as a function of bias voltage is shown in Figure 4.1.

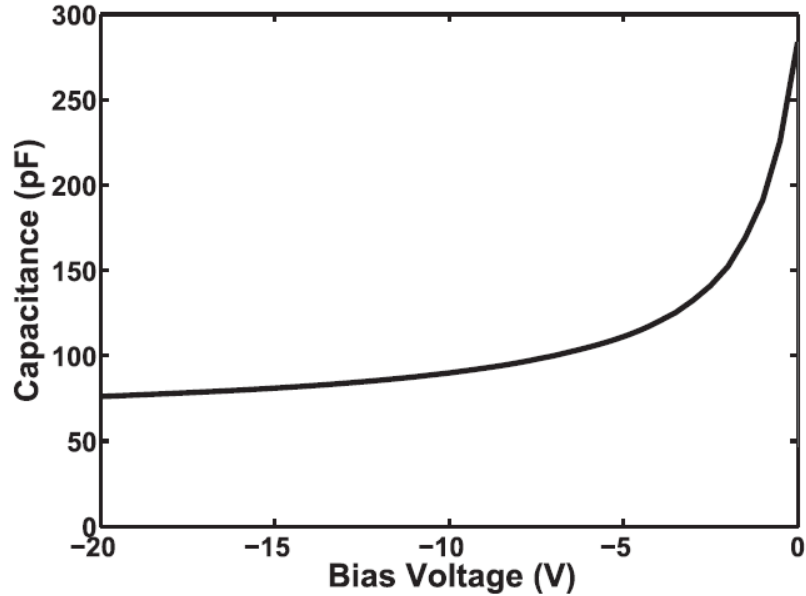


Figure 4.1: Capacitance vs. bias voltage for a 6.25 mm² honeycomb SSND developed at RPI.

The detector capacitance is significantly augmented when the individual devices are connected in parallel in order to increase the detector surface area. For example, a 1-cm² device is composed of 15 individual 6.25 mm² devices connected in parallel and typically has a capacitance of ~ 4480 pF with zero bias voltage. A schematic of an individual 1-cm² device can be seen in Figure 4.2. Note, one of the sixteen 6.25 mm² regions is inactive, so the active detection area of a “1 cm²” device is actually 0.9375 cm². An improved design of the contact fabrication will allow the full 1 cm² area to be active.

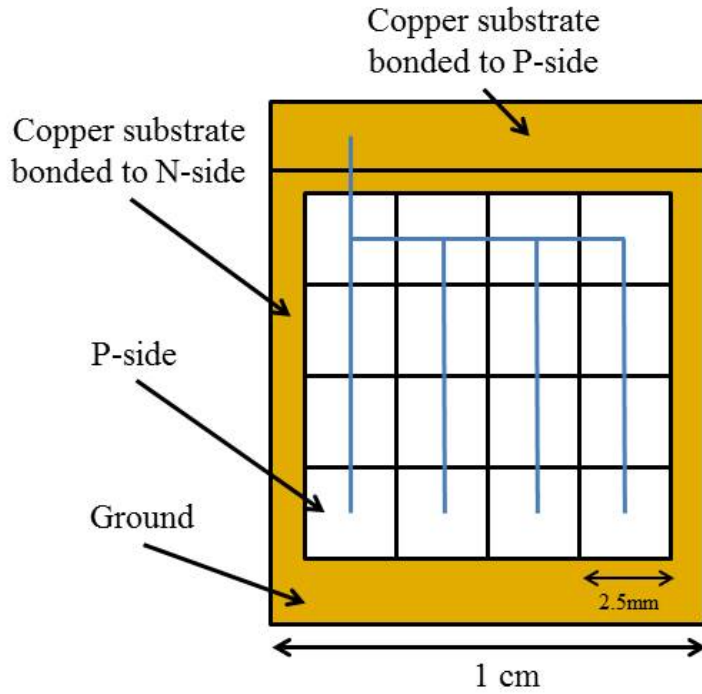


Figure 4.2: Schematic of a 1-cm² SSND mounted on a copper substrate.

The 1-cm² devices can be scaled to larger surface areas due to their extremely low leakage currents [13]. The leakage current of a 1-cm² honeycomb device can be seen in Figure 4.3.

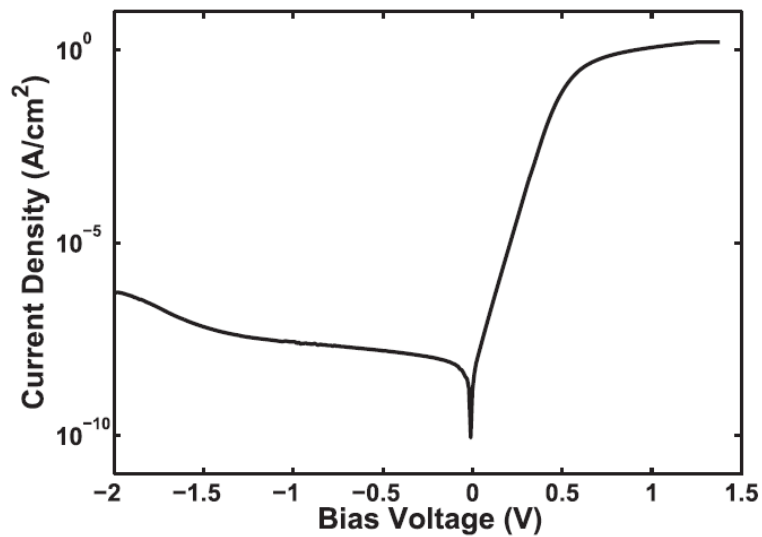


Figure 4.3: Leakage current as a function of bias voltage for a 1-cm² honeycomb SSND.

Typically the honeycomb SSNDs are packaged as 4 cm² units. A photograph of a 4 cm² device can be seen in Figure 4.4, and a schematic of a 4 cm² device can be seen in Figure 4.5, where the individual 6.25 mm² devices are connected in parallel and the 1 cm² devices are connected in series.

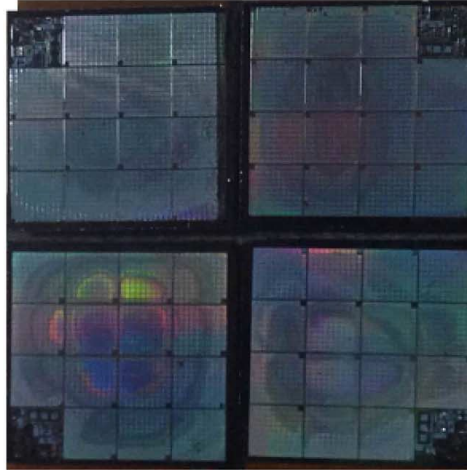


Figure 4.4: Photograph of a 4-cm² honeycomb SSND.

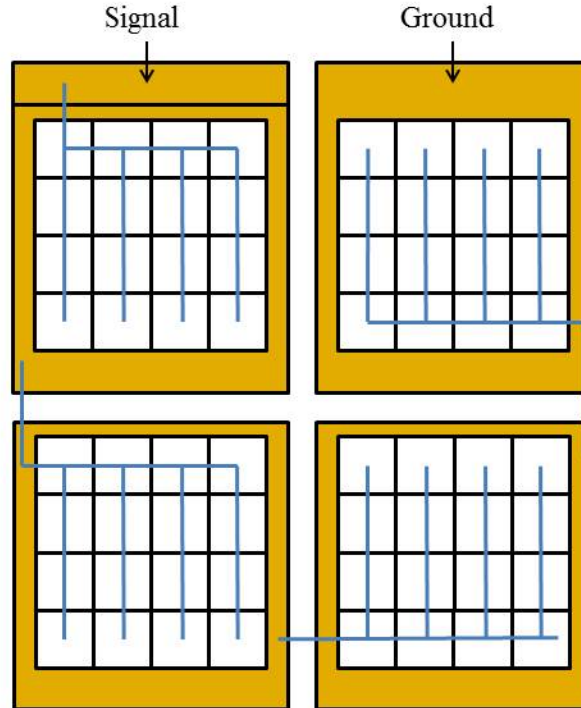


Figure 4.5: Diagram of a 4-cm² honeycomb detector comprised of individual 6.25 mm² devices.

Using preamplifiers that are optimized for devices with smaller capacitance leads to an increased electronic noise level. An increase in the noise level results in a higher LLD, which decreases the fraction of neutron events that are counted and decreases the measured intrinsic thermal neutron efficiency of the device. Commercial low-noise preamplifiers for high capacitance devices do exist, but they do not meet the aforementioned criteria for portable systems [34]-[35]. Therefore, a set of customized electronics—eight channels of preamplifiers and shaping amplifiers—were developed specifically for the honeycomb microstructured SSNDs and their associated device capacitance. However, the relatively large capacitance of the large area detectors SSNDs developed at RPI leads to a number of unique challenges corresponding to the design of charge preamplifiers.

The first working low-noise, low-power, and compact preamplifier prototype was produced during the scope of this work. The customized prototype, which was designed and built at RPI, can be seen in Figure 4.6. The custom electronics have 8 channels of preamplifiers, shaping amplifiers and discriminators, which are powered by ± 8 volts. The input and output channels utilize BNC connections.



Figure 4.6: Top view of the RPI custom electronics, including one preamplifier, one shaping amplifier, and one discriminator built on printed circuit boards.



Figure 4.7: Side view of the housing for the RPI custom electronics showing the 8 BNC inputs.

This set of electronics provide an enhanced signal-to-noise ratio (SNR) compared to their commercial counterparts due to a 15% reduction in the noise level [36]. This improved SNR is quantified by an increase in the intrinsic thermal neutron efficiency. This comparison is investigated in a subsequent section outlining the measurement of intrinsic thermal neutron efficiency, and the results can be seen in Figure 4.19 and Table 4.3.

4.3 Electronic Noise and the Low-Level Discriminator (LLD)

An LLD is needed in every measurement in order to reject noise in the signal. Noise can be picked up at any point from the detector to input of the Multi-Channel Analyzer (MCA), but its most significant when the source is before the preamplifier input. For these reasons, extra efforts are taken to ensure that detector housings are completely light sealed, the preamplifier circuitry is properly and completely grounded—often extra wires are soldered to the preamplifier PCBs—and detector cables are grounded and shielded from external electromagnetic fields (EMFs) or radiofrequency (RF).

Every measured signal has some noise level, which corresponds to an energy deposited in the device. Additionally, cables and connections along the channel can pick up further noise. In order to determine the neutron count rate, the background signal must be discriminated from the neutron response. Each time a neutron response was measured with a SSND, a background measurement was taken as well. An LLD was set above the

background level in order to measure the detector response to incident neutrons. The pulse height spectra in Figure 4.8 shows an example of an LLD, which corresponds to the channel where the SNR is ≥ 1000 —i.e. the count rate of the background response above the LLD is $\leq 0.1\%$ of the neutron response over the same region of interest.

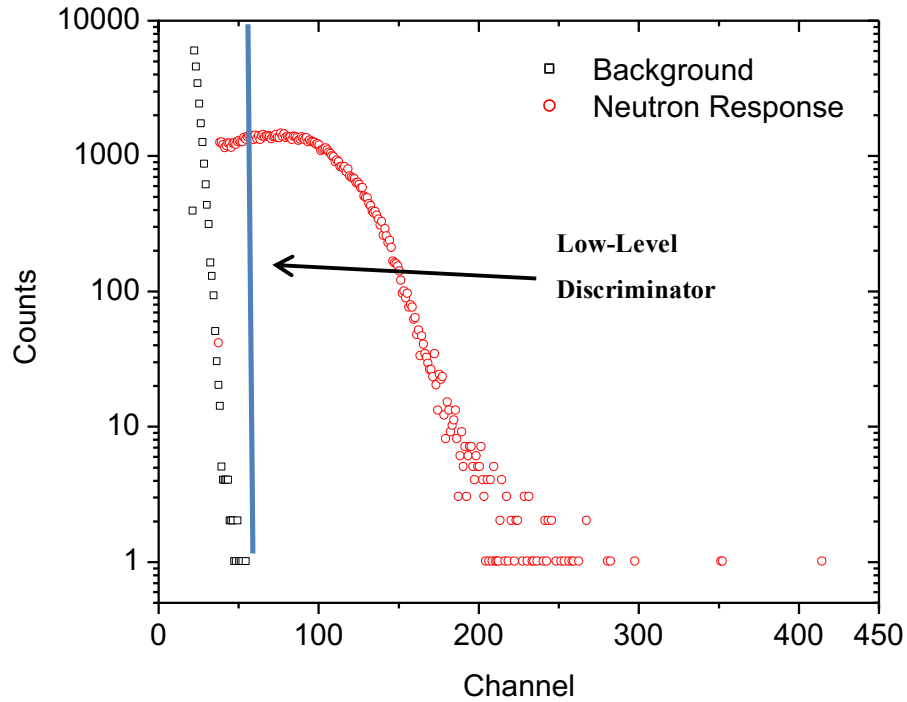


Figure 4.8: Background and neutron response of a SSND with an LLD set and labeled corresponding to a SNR of 1000.

4.4 Determining the Detector Efficiency

The following efficiency measurements refer specifically to the intrinsic thermal neutron efficiency, which is the probability that a thermal neutron is detected if it is incident on the active area of the detector. A thermal neutron resides in the thermal peak of a moderated neutron spectrum. For the purpose of these measurements, a thermal neutron is a neutron with kinetic energy below 0.5 eV, which is the cadmium (Cd) cutoff.

The intrinsic thermal neutron efficiency of the SSNDs was measured using a moderated ^{252}Cf spontaneous fission neutron source in the Calibrated Neutron Laboratory within

RPI's Nuclear Engineering and Science (NES) Building. The neutron emission rate of the source was calibrated to be 1.1×10^7 neutrons per second on February 16, 2009. The neutron source housing is a box of HDPE moderator, which serves as a shield when the source is stowed in the center hole and serves as a moderator when the source is placed in the exposure hole. Intrinsic thermal neutron efficiency measurements were performed once the thermal neutron flux at a well-defined position behind the exposure face was well characterized. A diagram of the HDPE housing—developed as part of a previous PhD thesis at RPI—can be seen in Figure 4.9 [14].

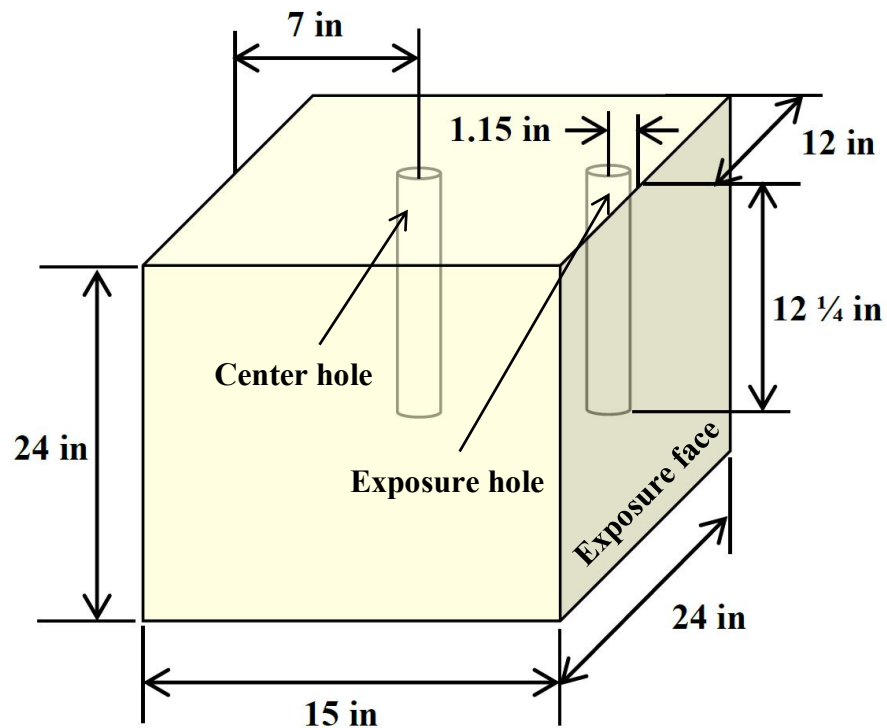


Figure 4.9: Diagram of the HDPE housing used to both store the ^{252}Cf source (center hole) and provide a moderated neutron flux when placed in the exposure hole [14].

An MCNP model of the experimental configuration shown in Figure 4.9 was created in order to simulate the neutron flux shape at the exposure face. The resulting moderated neutron spectrum can be seen in Figure 4.10, which labels the thermal region of the neutron spectrum and the Cd cutoff energy.

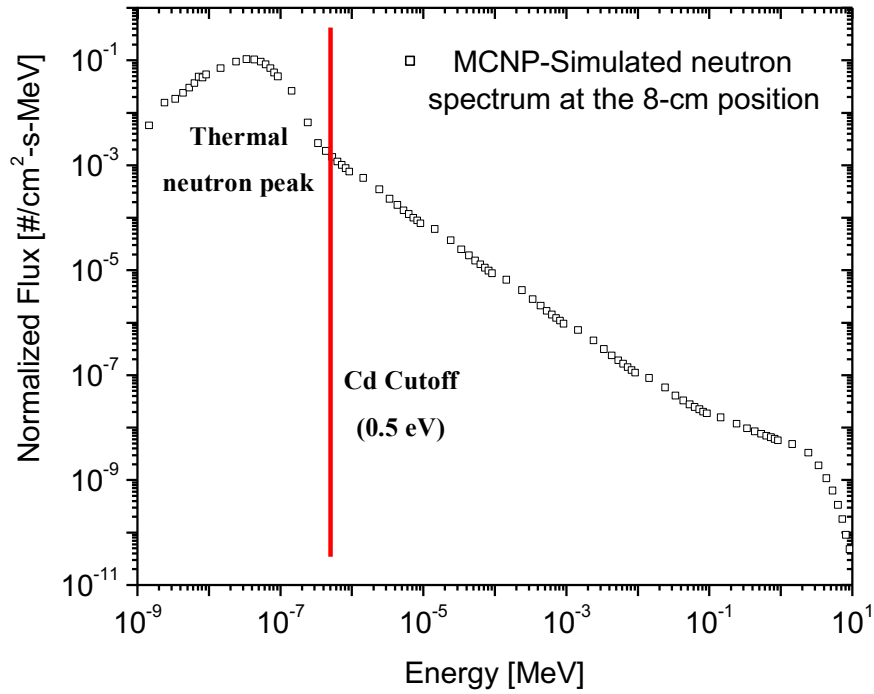


Figure 4.10: MCNP simulation of the neutron spectrum at the exposure face of the moderated ²⁵²Cf neutron source in RPI’s Calibrated Neutron Laboratory.

Cadmium effectively absorbs all neutrons below the Cd cutoff because of ¹¹³Cd’s large neutron absorption cross-section at thermal energies and a precipitous drop-off at 0.4-0.5 eV, which can be seen by the ENDF-VII ¹¹³Cd cross-section plot in Figure 4.11.

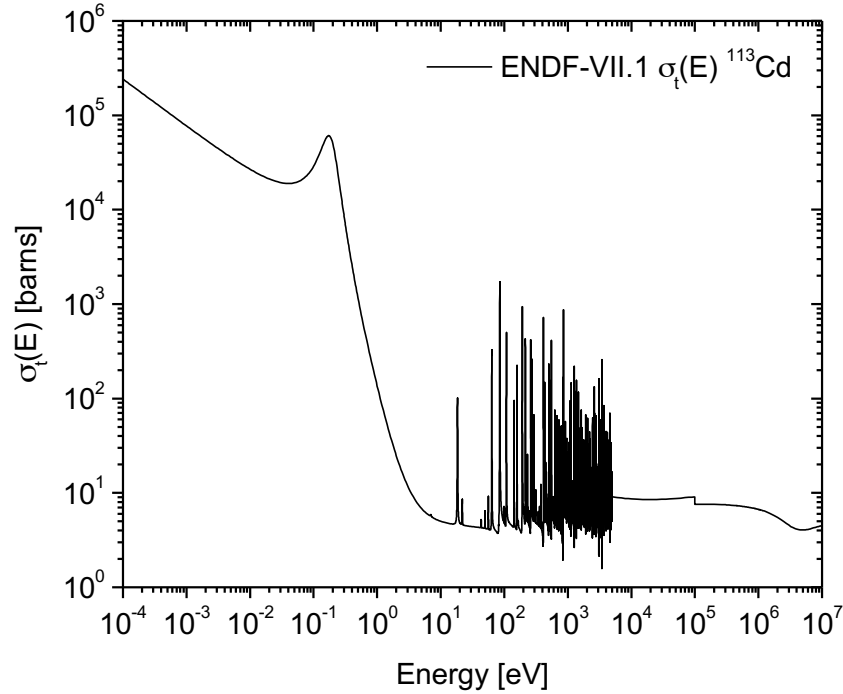


Figure 4.11: Total cross-section for ^{113}Cd according to ENDF-VII demonstrating the precipitous drop off at 0.4-0.5 eV.

Measurements of the intrinsic thermal neutron efficiency involve exposing the detector to a well-characterized neutron flux and, subsequently, exposing the Cd-covered detector to the same flux. The count rates corresponding to the bare and Cd-covered detector are called C_{bare} and C_{Cd} , respectively. Since the Cd effectively absorbs neutron below 0.5 eV, the difference of C_{bare} and C_{Cd} is approximately the count rate due to neutrons in the thermal peak. This count rate is defined as the thermal neutron response, which is used to determine the intrinsic thermal neutron efficiency (η_{th}) using equation (6). The active area of the detector (A) [cm^2] and the thermal neutron flux (Φ_{th}) [$\text{n}/\text{cm}^2\text{-s}$] are also required for this calculation.

$$\eta_{th} = \frac{C_{bare} - C_{Cd}}{A * \Phi_{th}} \quad (6)$$

4.4.1 Thermal Neutron Flux Measurements

Measurement of the intrinsic thermal neutron efficiency requires a well-characterized thermal neutron flux. Therefore, the thermal neutron flux was characterized at a well-defined position—8 cm behind the exposure face of the aforementioned moderated neutron source aligned axially and vertically with the source. Measurement of the thermal neutron flux at the 8-cm position provided a calibration position for the intrinsic thermal neutron efficiency measurements. Additionally, MCNP simulations representative of the experimental setup were performed for comparative purposes. Three independent detection methods and the MCNP simulations provided reasonable agreement. The three experimental measurements used to calibrate the thermal neutron flux are as follows:

- A Li glass scintillator
- A gold (Au) activation foil
- An indium (In) activation foil

4.4.1.1 Lithium Glass Scintillator

The Li glass scintillator used for the measurements presented here is a GS-20 scintillator with 6.6% Li by weight, 95% ^6Li enrichment, and a density of 2.5 g/cm^3 [37]. The scintillating crystal is cylindrical with a diameter and height of 2.5 cm. The detector was surrounded by boron carbide B_4C blocks enriched to 99% ^{10}B in order to ensure that only neutrons incident on the front face of the detector were counted. A picture of the collimated detector and the experimental setup at the 8-cm position are depicted in Figure 4.12.

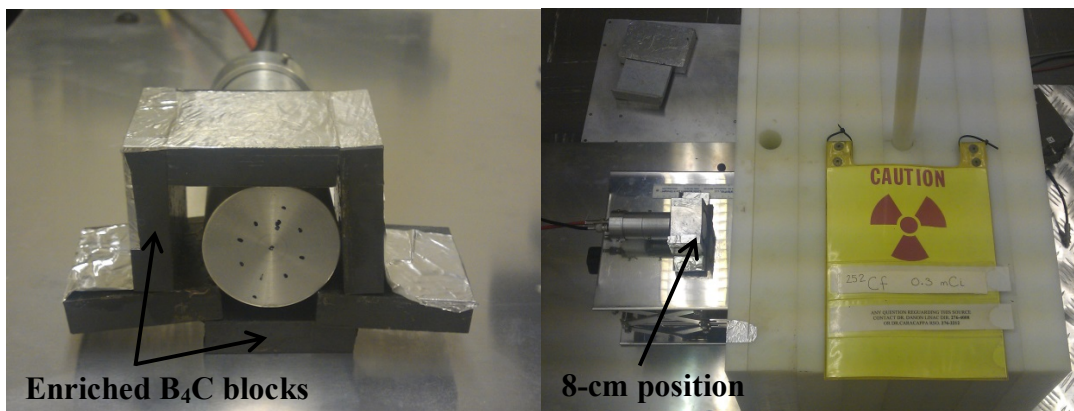


Figure 4.12: (Left) Li glass scintillator surrounded by enriched B₄C blocks. (Right) Experimental setup used to measure the thermal neutron flux at the 8-cm position using the Li glass detector.

The collimated Li glass scintillator was aligned at the 8-cm position—as shown in Figure 4.12 (Right)—and was exposed to the ²⁵²Cf source in the exposure hole. The detector was operated with a bias of +700 volts, and the detector signal was input into an ORTEC shaping amplifier with an integration time of 1.0 μs and a gain of 160. A pulse height spectrum was collected for 300 seconds for this bare detector measurement. Subsequently, the entire face of the Li glass detector was covered with 1.0 mm of Cd, and data was collected with the same configuration. The resulting pulse height spectra of these two 300 second measurements can be seen by Figure 4.13.

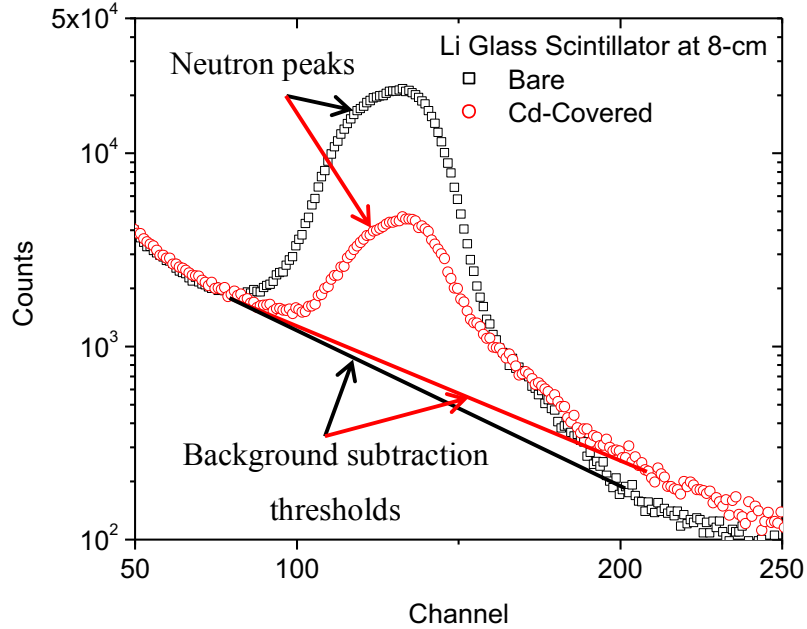


Figure 4.13: Pulse height spectra collected with the bare and Cd-covered Li glass scintillator for 300 seconds at the 8-cm position.

The counts under the neutron peaks—corresponding to the bare and Cd-covered detector—are called $C_{Li,Bare}$ and $C_{Li,Cd}$, respectively. The background of each measurement was estimated by fitting a background-subtraction threshold line below the two neutron peaks, which are labeled in Figure 4.13. The background counts corresponding to the same two measurements are termed $B_{Li,Bare}$ and $B_{Li,Cd}$, respectively. Since ${}^6\text{Li}$ has a large thermal neutron cross-section (941 barns at 0.0253 eV) and the scintillator is 2.5 cm-thick, the efficiency of the detector is assumed to have an intrinsic thermal neutron efficiency of 100% [14]. Therefore, the thermal neutron flux is calculated using equation (7).

$$\Phi_{th} = \frac{(C_{Li,bare} - B_{Li,bare}) - (C_{Li,cad} - B_{Li,cad})}{A * t} \quad (7)$$

The thermal neutron flux below the Cd cutoff (0 to 0.5 eV) is called Φ_{th} . C_{bare} and C_{Cd} are the counts below the neutron peaks corresponding to the bare and Cd-covered detector, respectively. B_{bare} and B_{Cd} are the counts under the background subtraction threshold for their respective measurements. The area of the 2.5cm-diameter scintillator is 4.91 cm²

and is labeled as A. The measurement time, t , was 300 seconds. The thermal neutron flux was measured to be 386.6 ± 22.3 [n/cm²-s] at the 8-cm position using the Li glass scintillator. The error in the net counts under the two neutron peaks was assumed to be the square root of the counts, so the uncertainty in the measured thermal neutron flux was calculated using equation (8).

$$\Delta\Phi = \Phi \sqrt{\frac{1}{(C_{bare} - B_{bare})} + \frac{1}{(C_{Cd} - B_{Cd})}} \quad (8)$$

4.4.1.2 Gold Activation Foil

Gold foils have long been used to calibrate neutron fluxes [38]-[40]. At RPI, a thin gold activation foil was used to calculate the thermal neutron flux at the aforementioned 8-cm position. The foil has a mass of 1.24 g, dimensions of 25 mm x 25 mm x 0.1 mm, and a purity of 99.95%. Exposing the natural gold foil (100% ¹⁹⁷Au) to a moderated neutron source induces radiative capture reactions, which activate the foil. The total neutron reaction cross-section of ¹⁹⁷Au according to the Evaluated Nuclear Data File (ENDF) VII.1 can be seen in Figure 4.14.

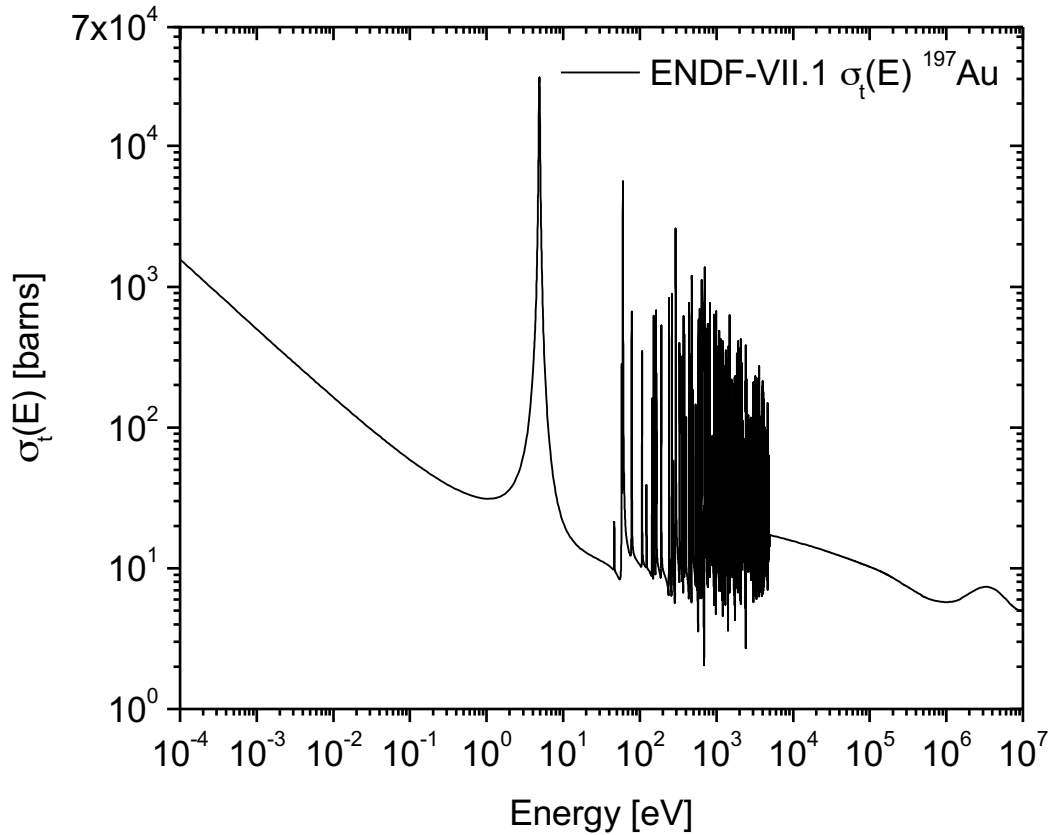
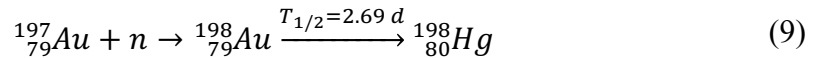


Figure 4.14: Total cross-section for ^{197}Au according to ENDF-VII.

Although Figure 4.14 plots the total neutron cross-section, the radiative capture reaction accounts for nearly the entirety of this cross-section, including the resonance structure at moderate energies and the thermal neutron cross-section at low energies. The neutron activation reaction of gold shown in equation (9) results in ^{198}Au , which decays via beta emission with a half-life of 2.69 days and is accompanied by a γ with energy of 411.8 keV.



The 1.24 g Au foil was exposed to the moderated ^{252}Cf source at the 8-cm position for just under four days (329,820 seconds). Subsequently, gamma spectroscopy was performed on the activated foil using a sodium iodide (NaI) scintillation detector. The foil was situated 5 cm from the detector face and data was collected for 12,275 seconds. The resulting pulse height spectra can be seen in Figure 4.15, where the photopeak from the ^{198}Au decay and background subtraction threshold are labeled.

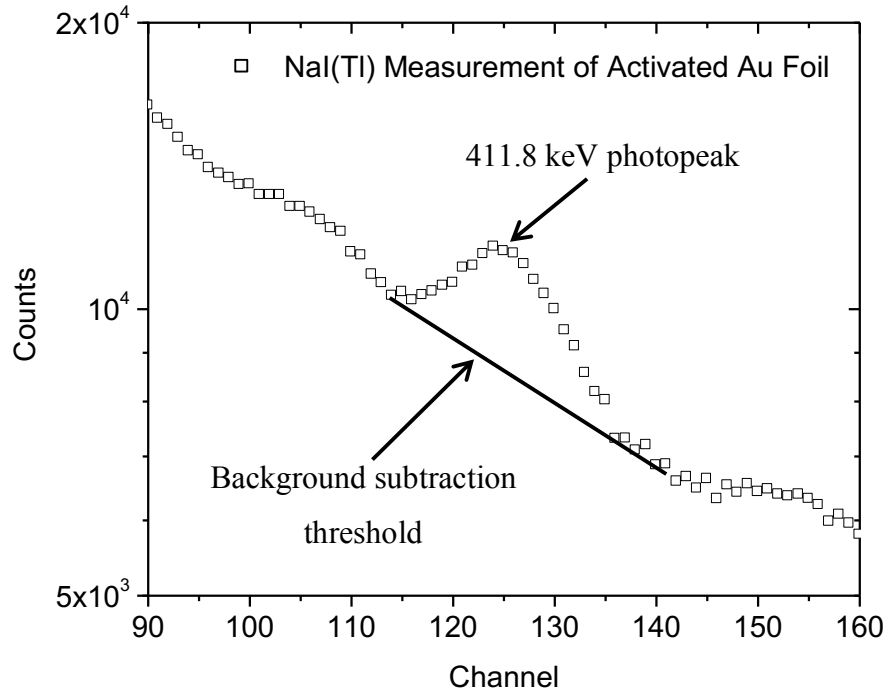


Figure 4.15: Au foil activated at 8-cm position measured with NaI(Tl) scintillator at a distance of 5 cm.

The foil was allowed to decay for multiple half-lives and was subsequently exposed at the same 8-cm position with a Cd covering. Gamma spectroscopy was performed under the same conditions. The net counts under the photopeaks (C_{bare} and C_{Cd}) associated with the 411.8 keV γ from the decay of ^{198}Au corresponding to the bare and Cd-covered measurement were calculated using the background subtraction threshold.

The flux-averaged cross-section, which is required in order to calculate the thermal neutron flux, was calculated for the neutron capture of ^{197}Au below the Cd cutoff energy of 0.5 eV. A Maxwellian flux shape was assumed, which is a good approximation for the moderated neutron source at RPI's Calibrated Neutron Laboratory. The flux-averaged cross-section for is represented by equation (10) and was determined to be 87 barns for ^{197}Au .

$$\sigma_{av} = \frac{\int_0^{0.5 \text{ eV}} \sigma_a(E) \Phi(E) dE}{\int_0^{0.5 \text{ eV}} \sigma_a(E) dE} \quad (10)$$

The solid-angle of the experimental configuration corresponding to the gamma spectroscopy measurement with the NaI scintillator was determined using equation (11).

$$\Omega \approx 2\pi \left(1 - \frac{d}{\sqrt{d^2 + r^2}}\right) \quad (11)$$

The distance between the activation foil and scintillation detector is d (5 cm), and r is the radius of the scintillator (3.81 cm). The intrinsic efficiency of the NaI scintillator was determined using two calibration γ sources— ^{137}Cs (661.7 keV) and ^{22}Na (511 keV). An exponential trend line was created, and the efficiency associated with the 411.8 keV photopeak was determined to be 0.377. The thermal neutron flux was calculated using equation (12).

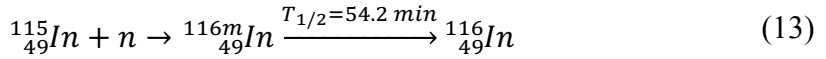
$$\Phi_{th} = \frac{\lambda}{N\sigma_{av}V} \frac{4\pi}{\Omega} \frac{1}{\epsilon f} \left[\frac{C_{bare} - C_{Cd} - C_{res}}{(1 - e^{-\lambda t})(e^{\lambda(t-t_1)} - e^{\lambda(t-t_2)})} \right] \quad (12)$$

The decay constant for ^{198}Au is λ [s^{-1}], N is the number density of the activation foil [atoms/ cm^3], σ_{av} is the flux-averaged cross-section for neutron capture in ^{197}Au [barns], V is the volume of the foil [cm^3], Ω is the solid-angle, ϵ is the intrinsic efficiency of the gamma spectrometer corresponding to the 411.8 keV photopeak, f is the branching ratio for the same photopeak, C_{res} is the residual count rate from the previous activation measurement, t is the irradiation time [s], t_1 is the time between the end of the irradiation and the beginning of the gamma spectroscopy [s], and t_2 is the time between the end of the irradiation and the end of the gamma spectroscopy [s]. The thermal neutron flux was calculated to be 387 ± 22 [$\text{n}/\text{cm}^2\text{-s}$] using the aforementioned gold foil analysis.

4.4.1.3 Indium Activation Foil

An indium activation foil was also used to determine the thermal neutron flux at the 8-cm position. Indium has two stable isotopes (^{113}In and ^{115}In), but the isotope of interest for this activation analysis is ^{115}In , which accounts for 95.7% of natural In. The activation of

^{113}In is negligible due to its low abundance (4.3%) and small thermal neutron cross-section [41]. The neutron capture reaction of interest for ^{115}In can be seen by equation (13).



The decay of ^{116m}In has a half-life of 54.2 minutes and has a complex decay scheme with multiple, discrete γ 's. The γ 's with significant branching ratios are shown in Table 4.1.

Table 4.1: Gamma energy and branching ratios associated with the decay of ^{116m}In according to ENDF/B-VII.1.

E_{γ} [keV]	Branching Ratio [%]
416.9	27.2
818.7	12.1
1097.3	58.5
1293.6	84.8
1507.6	9.9
2112.3	15.1

A natural In activation foil with dimensions of 2 cm x 2 cm x 0.76 mm, a mass of 2.49 g, and a purity of 99.99% was irradiated by the moderated neutron source at the 8-cm position. This foil was activated for more than ten half-lives, reaching the equilibrium activity.

Gamma spectroscopy of the activated In foil was performed with a lanthanum bromide (LaBr) scintillator. This detector has a better resolution than the NaI scintillator which was used for the Au foil activation measurement; the resolution of the LaBr detector was measured to be 3.1% for a ^{137}Cs calibration source ($E_{\gamma}=661.7$ keV). However, the LaBr has a lower intrinsic efficiency (0.33 corresponding to the 416.9 keV γ) and a smaller solid-angle due to its smaller size; this LaBr scintillator is a cylindrical crystal with a diameter of 2.54 cm. The employment of the LaBr scintillator allows for the resolution of individual γ 's corresponding to the decay of ^{116m}In . An example of a pulse height spectrum

resulting from an activated In sample collected on the face of the LaBr can be seen in Figure 4.16, where the individual photopeaks are labeled with their energy and branching ratio.

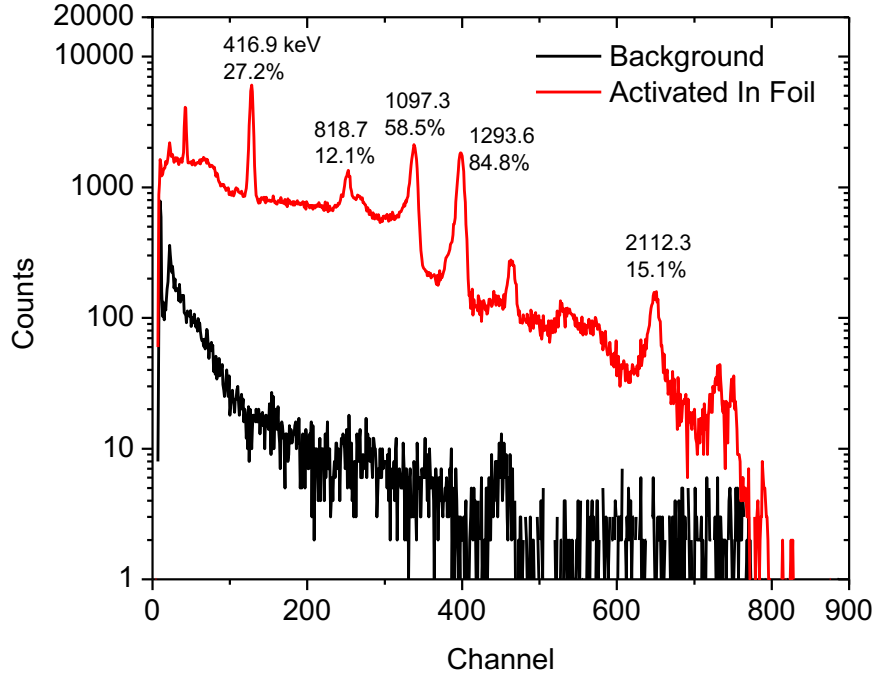


Figure 4.16: LaBr pulse height spectrum collected with an activated In foil and background.

The gamma spectroscopy of the In foil irradiated at the 8-cm position was performed with the aforementioned LaBr scintillator at a source-detector distance of 3.5 cm, a bias voltage of +630 volts, an integration time of 250 ns, and a gain of 60. The counts under the 416.9 keV photopeak were recorded after 5,000 seconds of gamma spectroscopy. The net count rate under the 416.9 keV photopeak was determined using the same background subtraction threshold shown in Figure 4.15. The gamma spectroscopy measurement of the In foil activated at the 8-cm position (both bare and Cd-covered) can be seen in Figure 4.17.

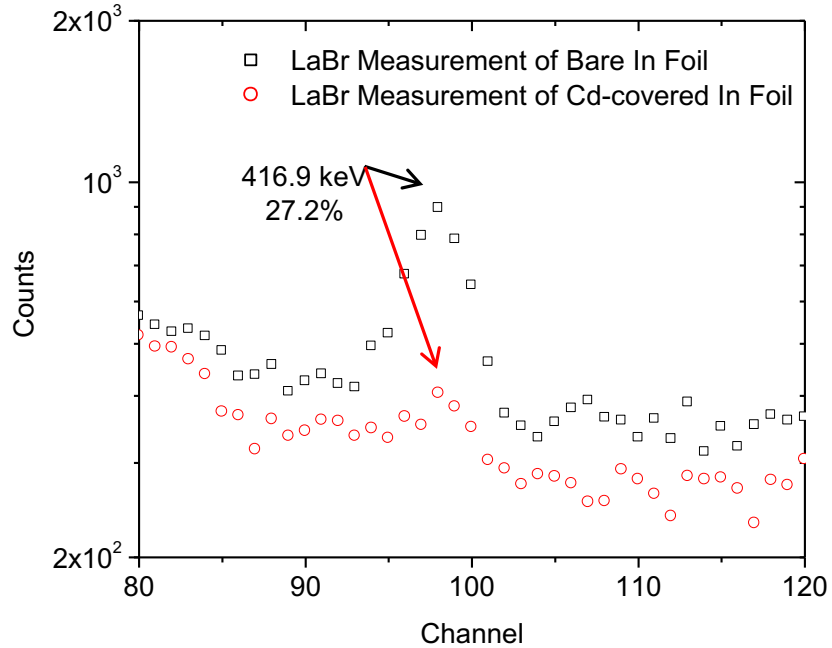


Figure 4.17: Gamma spectroscopy of the 2.49g indium foil activated at the 8-cm position collected with a LaBr scintillator for 5,000 seconds 3.5 cm from the foil.

The decay constant (λ) [s^{-1}], the number density of the foil (N) [$atoms/cm^3$], the flux-averaged cross-section (σ_{av}) [barns], the foil volume (V) [cm^3], solid-angle (Ω), intrinsic efficiency (ϵ), and branching ratio (f) were calculated for the In foil and the decay of ^{116m}In . The flux-averaged cross-section for the production of ^{116m}In for the given neutron spectrum was determined to be 111 barns. The thermal neutron flux at the 8-cm position at the time of the experiment was calculated using equation (12) to be 380 ± 24 [$n/cm^2 \cdot s$].

4.4.1.4 Thermal Neutron Flux Comparisons

The resulting thermal neutron flux values corresponding to the 8-cm position behind the moderated ^{252}Cf neutron source measured by the three aforementioned methods are shown in

Table 4.2. These flux values were measured between July and September 2015, but the listed values were corrected in order to represent the flux on September 1, 2015. During subsequent experiments, the averaged thermal neutron flux was decay corrected corresponding to the experiment date using the 2.54 year half-life of ^{252}Cf ($\lambda=0.394 \text{ a}^{-1}$). Additionally, results of a representative MCNP simulation are included in

Table 4.2. This simulation was performed by modeling the aforementioned HDPE housing with the ^{252}Cf source in the exposure hole. The source was modeled as a Watt fission spectrum with parameters corresponding to ^{252}Cf spontaneous fission. The source was encapsulated in metal and attached to a long HDPE rod. The MCNP simulations also included the major laboratory features, including the walls, floor, and ceiling, which can reflect emitted neutrons back towards the detector. A detector tally was collected at the 8-cm position using an F4 flux tally. Since MCNP simulations provide the neutron flux per emitted source particle per cm^2 , the flux tally was multiplied by the instantaneous ^{252}Cf neutron emission rate in order to determine the incident thermal neutron flux [$\text{n}/\text{cm}^2\text{-s}$]. The flux tally was segmented by energy bins, and neutrons with energy below the Cd cutoff ($E_n < 0.5 \text{ eV}$) were counted since it is the thermal neutron flux that is of interest. The ^{252}Cf neutron emission rate on September 1, 2015 was calculated to be approximately $1.98 \times 10^6 \text{ n/s}$, which was calculated using the calibrated neutron emission rate of $1.1 \times 10^7 \text{ n/s}$ on February 1, 2009 and the 2.646 y half-life of ^{252}Cf . Multiplication of the resulting F4 flux tally at the 8-cm position by the calculated neutron emission rate, provides a simulated thermal neutron flux of approximately 397 [$\text{n}/\text{cm}^2\text{-s}$] on September 1, 2015. The reasonable agreement between the thermal neutron flux averaged among the three

experimental methods and the MCNP simulations provide confidence that the results are reliable. The averaged thermal neutron flux of 384.5 [n/cm²-s] measured on September 1, 2015 was decay corrected with the ²⁵²Cf half-life for every subsequent measurement in order to calibrate the intrinsic thermal neutron detection efficiency of many devices.

Table 4.2: Calculated thermal neutron flux corresponding to the 8-cm position on 9/1/2015.

Method	Thermal Neutron Flux [n/cm ² -s]
Lithium Glass Scintillator	386.6±22.3
Gold Foil	387±18.0
Indium Foil	380±24.4
Average	384.5±12.5
MCNP Simulation	396.5

While these experimentally measured thermal neutron flux values demonstrate consistency and reliability, there is some discrepancy with previously measured values using the same ²⁵²Cf source and HDPE housing. On March 16, 2010 Justin Clinton measured the thermal neutron flux at the aforementioned 8-cm position. These measurements determined that the thermal neutron flux was 1868±58 [n/cm²-s] [14]. Using the radioactive decay equation and the half-life of 2.646 years, the flux on September 1, 2015 (~1,995 days later) should be approximately 421±13 [n/cm²-s]. This value is slightly higher than the 386.6±22.3 [n/cm²-s] measured with the Li glass scintillator. This discrepancy was puzzling, and was the major reason for this in-depth flux investigation with multiple activation foils. After investigating Clinton's original

measurements and comparing them to the new measurements, there was no clear explanation for the discrepancy. There are a number of possible reasons for the inconsistency, including errors in the determination of the gamma detectors' intrinsic efficiency or solid angle efficiency, mischaracterization of the activated foils' gamma spectra and/or background spectra, or a small uncertainty in the position of the measured flux. Additionally, it is possible that Clinton's experimental configuration was slightly different. For example, placing the HDPE housing closer to the corner of the laboratory would increase the measured thermal neutron flux at the 8-cm position due to neutrons reflected by the walls. It is even possible that two independent researchers consistently defined the 8-cm position slightly differently. For example, if Clinton consistently placed his detectors and foils at 7.75 cm, while the new measurements were performed at 8.25 cm, there would be a statistically significant discrepancy. However, as long as the exact location of the 8-cm position was consistently chosen for the flux calibration and efficiency measurements, the measured thermal neutron efficiencies will be accurate. Therefore, since the neutron flux measurements performed during the scope of this thesis were reproducible, consistent among the three methods, reasonably agree with MCNP simulations, and resulted in experimentally measured neutron detector efficiencies that were consistent with other experimenters, the values were considered reliable and accurate. After this investigation, there is no sound explanation of the discrepancy. It is this researcher's opinion that slightly different experimental configurations led to the differences.

4.5 Intrinsic Thermal Neutron Efficiency Measurements

The intrinsic thermal neutron efficiency of the SSNDs was determined by exposing a device to the thermal neutron flux at the aforementioned 8-cm position corresponding to the moderated neutron source diagramed in Figure 4.9. In this context, thermal neutrons refer to neutrons below the Cd cutoff of 0.5 eV. The best 1-cm² honeycomb SSND ($A=0.9375$ cm²) was exposed to this flux and the neutron response of the bare and Cd-covered device was collected for 100 seconds along with a 100-second background

measurement. These responses, which were taken with the customized preamplifier, are displayed in Figure 4.18.

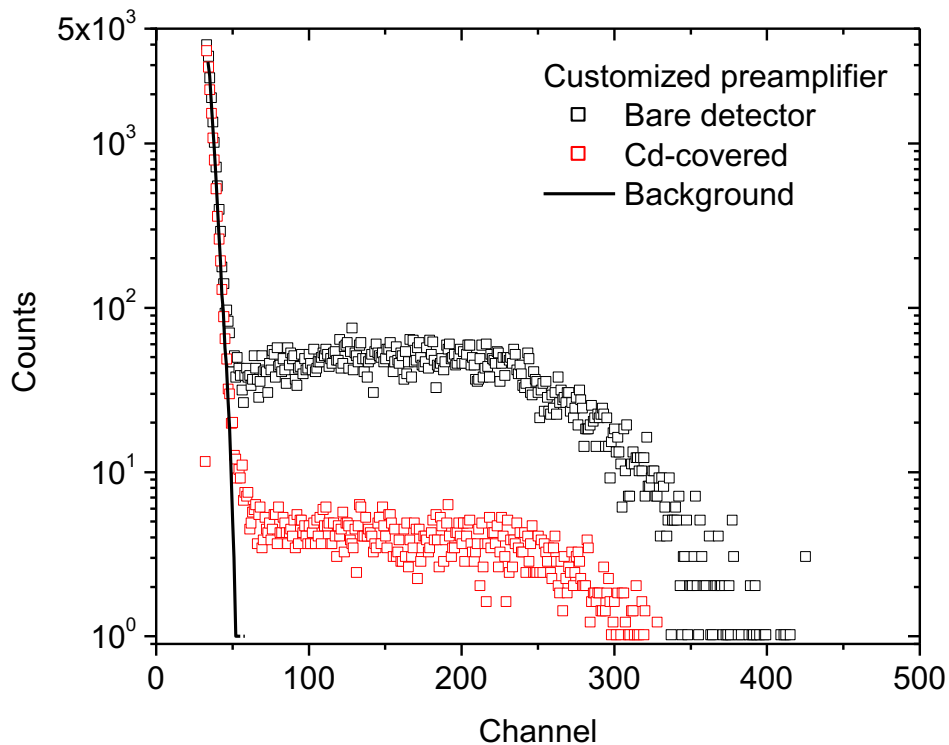


Figure 4.18: Detector responses (bare, Cd-covered, and background) of the best 1-cm² honeycomb SSND at the 8-cm² position.

The neutron count rates corresponding to the bare and Cd-covered measurements (Figure 4.18) were determined by summing the counts in the channels above the LLD and dividing by the measurement time. The LLD channel was set corresponding to a SNR of 1000. In other words, the bare measurement PHS had 1000x more counts above the LLD channel than the background measurement. Importantly, the count rate induced by incident thermal neutrons ($E_n < 0.5$ eV) is the difference of the two measured count rates, $C_{\text{Bare}} - C_{\text{Cd}}$. The intrinsic thermal neutron efficiency was determined using the aforementioned count rates, the detector area, and the thermal neutron flux at the 8-cm position. The intrinsic thermal neutron efficiency of the best 1-cm² honeycomb microstructured device taken with the customized preamplifier is 28.4%.

The same efficiency measurements were performed with a commercial ORTEC 142AH preamplifier instead of the aforementioned customized preamplifier. These measurements demonstrate that the customized preamplifier results in significantly increased performance of the best 1-cm² honeycomb device. The efficiency corresponding to the commercial preamplifier measurements with the same SNR is 24.0%. This decrease in efficiency (24.0% vs. 28.4%) is due to the lower noise level of the customized preamplifier corresponding to the best 1-cm² honeycomb device. The pulse height spectra corresponding to the commercial ORTEC preamplifier are compared to the customized preamplifier in Figure 4.19.

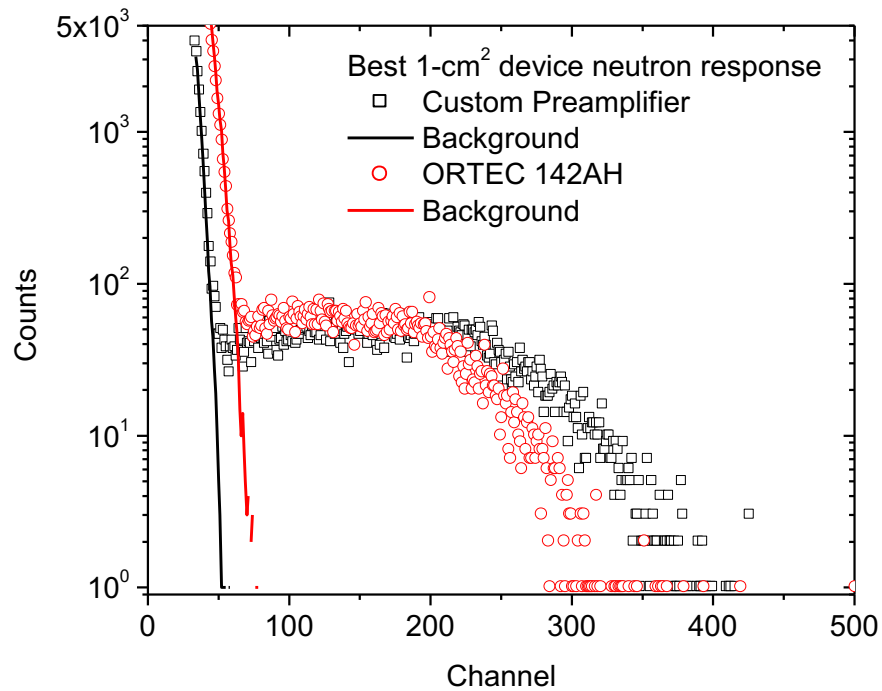


Figure 4.19: Detector responses (bare, Cd-covered, and background) of the best 1-cm² honeycomb SSND at the 8-cm² position corresponding to the customized and commercial preamplifiers.

Table 4.3: Results of the intrinsic thermal neutron efficiency measurements performed with two amplifiers.

Preamplifier	C_{Bare}	C_{Cd}	η_{th}
Customized electronics	109.0	10.4	28.4%
ORTEC 142AH	92.7	9.3	24.0%

4.6 Gamma Discrimination

Since these microstructured SSNDs detect neutrons via energetic ions produced by neutron absorption in ^{10}B , the maximum signal from a neutron event is significantly above the background level. These SSNDs reject the background signal and incident gammas (γ 's) with an adjustable low-level discriminator (LLD). The γ response of the honeycomb detectors was evaluated by exposing a 4-cm² to incremental exposure rates from a 1.3 Curie (Ci) ^{137}Cs γ source (E=661.7 keV). The response of these experiments can be seen in Figure 4.20.

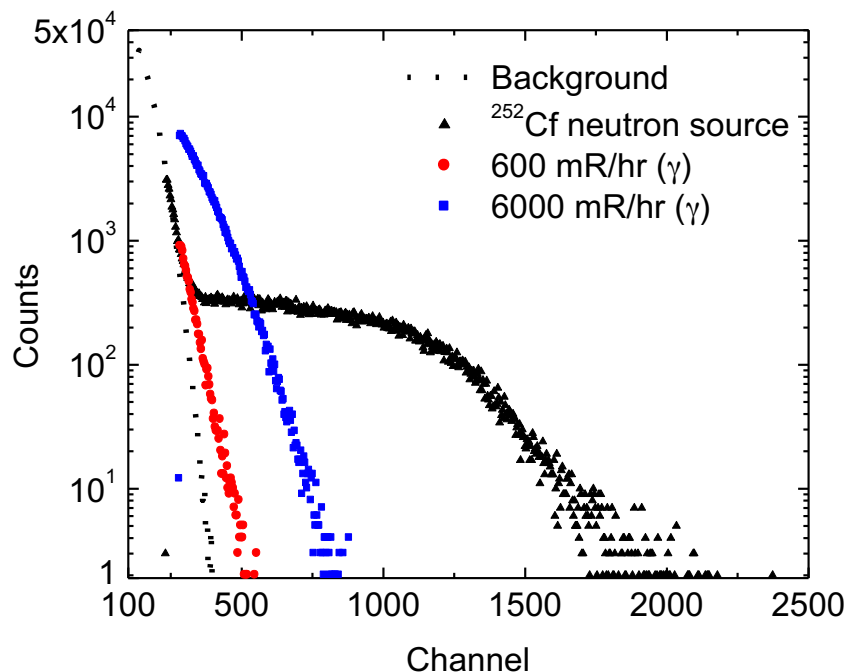


Figure 4.20: Response of a 4-cm² honeycomb device exposed to a calibrated ¹³⁷Cs source compared to the response to a moderated ²⁵²Cf neutron source and the device background.

The honeycomb SSND responds γ 's when the exposure rate is high because multiple γ 's are likely to interact in coincident. However, even large exposure rates of 600 MilliRoentgen (mR)/hour or 6 R/hr can be rejected using the adjustable LLD. Exposure of the detector to lower γ exposure rates produces a signal indistinguishable from the device's background. Overall, the γ -discrimination of the honeycomb SSNDs achieves a ratio better than the PNNL recommendation for a well-designed neutron detector (10^{-6} for a 10 mR/hr exposure rate from a ⁶⁰Co source) [42].

4.7 Detector Scalability

Since each detector unit requires preamplification, pulse shaping, and a low-level discriminator, electronic instrumentation accounts for a significant portion of a neutron detection system's cost and size. The ability to scale detection units to larger surface areas can reduce the cost and volume of a neutron detection system with the same absolute sensitivity. The honeycomb SSNDs—which are initially configured into 1-cm²

modules—have demonstrated scalability to larger surface areas using a series connection due to an extremely low leakage current [13].

Scaling the detector area by connecting devices in series causes the device capacitance—and therefore electronic noise—to decrease; however, the amount of charge captured by the preamplifier also decreases. The signal level decreases faster than the noise level, so the net effect is a degradation of the signal-to-noise ratio (SNR) with an increasing device area. Conversely, the connection of devices in parallel causes the device capacitance to increase which leads to higher electronic noise as the area is increased. Overall, a parallel connection degrades the SNR significantly faster than a series connection. A set of four 4-cm² devices were connected in series in order to produce devices with areas 4, 8, 12, and 16-cm². The pulse height spectra of these devices can be seen in Figure 4.21.

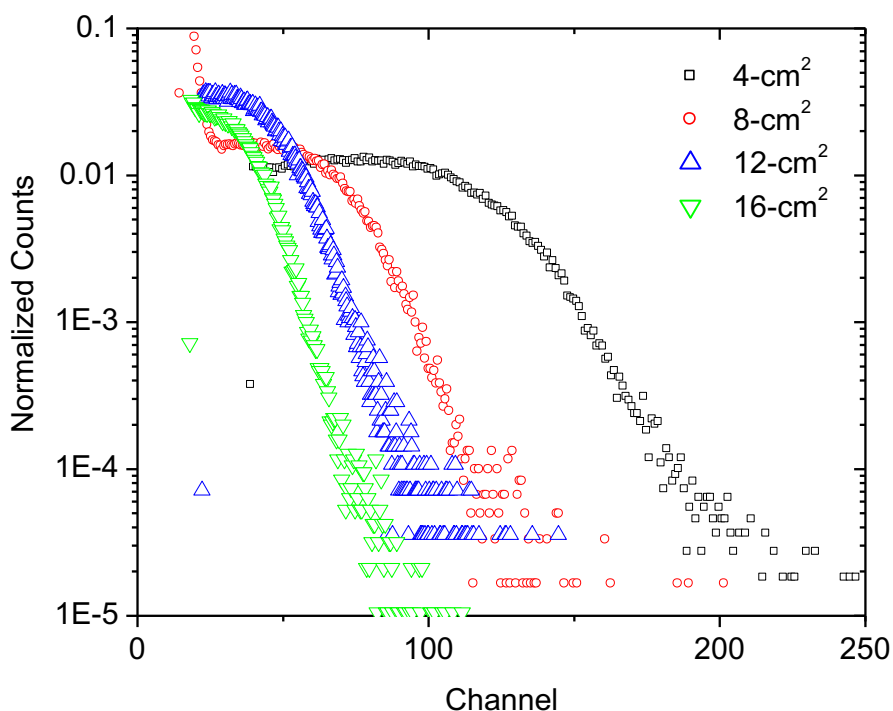


Figure 4.21: Pulse height spectra for honeycomb SSNDs with surface areas of 4, 8, 12, and 16-cm² exposed to a moderated ²⁵²Cf neutron source.

The pulse height spectra in Figure 4.21 demonstrate that the signal is compressed as the device area is increased. As discussed, increasing the device area leads to a degradation of the SNR. In order to quantify the effect of scaling the devices to larger areas, the

efficiency of each scaled device—relative to the individual 4-cm² units—was determined. In order to determine the relative efficiency of the scaled devices, a background measurement was taken for each 4-cm² device, as well as the 8, 12, and 16-cm² devices. Subsequently, each device was exposed to a moderated neutron source at a well-defined position with the same electronic amplification and integration time. The appropriate LLD for each detector configuration was determined using the background and neutron pulse height spectra.

The count rate of each detector configuration when exposed to the calibrated neutron source at the well-defined test location was determined using the aforementioned LLD and the corresponding collection time. The count rates of the four 4-cm² devices—previously labeled D1, D3, D5, and D6—and the larger devices are shown in Table 4.4. The relative efficiencies were determined by

Table 4.4: Relative efficiency associated with scaling the individual 4-cm² honeycomb devices to larger detection areas.

Detector Configuration	Detector Area [cm²]	Count Rate [cps]	Relative Efficiency
D1	4	371.3	1
D3	4	352.9	1
D5	4	342.8	1
D6	4	331.6	1
D1+D6	8	694.8	0.987
D1+D6+D3	12	941.3	0.89
D1+D6+D3+D5	16	1152.6	0.823

5. Applications of SSNDs

Microstructured SSNDs achieve adequate detection efficiency, good gamma discrimination, and scalability to large areas. Additionally, these devices—as opposed to their gas-filled counterparts—are flat, compact, require no bias voltage, and are thus easier to embed in different moderated configurations. These advantageous characteristics provide the opportunity to improve and even reinvent numerous neutron detection systems which implement gas-filled neutron detectors. The goal of this section is to develop the ground work and provide a proof of principle for some of the applications. Additionally, this thesis provides insight into the challenges and considerations involved with applying microstructured SSNDs for these applications.

5.1 A Modular Directional and Spectral Neutron Detection System (DSNDS)

A neutron detection system with the ability to provide positional and spectral information about an unknown neutron source was developed at RPI for the scope of this thesis. This DSNDS is composed of a stack of five high-density polyethylene (HDPE) disks with a thickness of 5 cm and a diameter of 30 cm. The middle disk contains 16 of the honeycomb-microstructure SSNDs fabricated at RPI, each with an area of four cm². These detectors are arranged as one internal (moderated) and one external (unmoderated) ring of SSNDs. These two detector rings provide the ability to determine the directionality of a neutron source. The system gathers spectral information about a neutron source in two ways: by measuring the relative responses of the internal ring of detectors as well as measuring the ratio of the internal-to-external detector responses.

The DSNDS can be seen in Figure 5.1 with eight (four internal and four external) of the 16 total detectors. As constructed, the DSNDS—including 16 detectors—has a mass of about 16 kg. The central hole was used to house the ²⁵²Cf source during detector calibration, a process to determine the relative detector efficiencies in order to normalize the individual detector responses. This hole can be plugged if needed.

This chapter previously appeared as: A. Weltz *et al.*, “Development of a modular directional and spectral detection system using solid-state detectors,” *Nucl. Instruments and Methods in Physics Res. A*, vol. 792, pp. 28-37, May 2015.

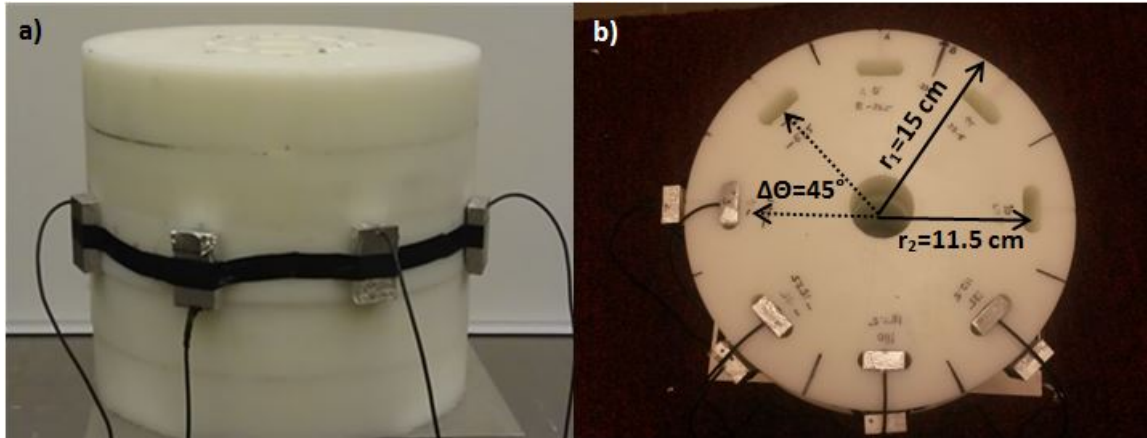


Figure 5.1: a) Front view of the system showing the external ring of detectors mounted on 5.08 cm (2") thick center HDPE disk, b) Top view of the system showing 4 internal and 4 external detectors.

5.1.1 DSND Design Optimization

The DSND was simulated using MCNP6 in order to determine the appropriate dimensions of the system. Since the solid-state detectors respond to thermal neutrons, the internal detectors should be positioned where the thermal neutron flux peaks due to an incident fission neutron spectrum. This optimal radial position of the internal detectors was determined by simulating a fission neutron spectrum and tallying the ^{10}B neutron absorption rate at different radii inside the HDPE cylinder with a radius of 15 cm and height of 25 cm. The results of this simulation, which were run until 2×10^7 histories were completed, show that the internal detectors should be positioned at a radius which is about 3.5 cm smaller than the radius of the cylinder, as seen in Figure 5.2a. Simulations were performed in order to determine the appropriate height and radius of the HDPE cylinder. First, the height of the large HDPE cylinder was varied in order to investigate how changes in the cylindrical height affect the response of the internal detectors at the optimal radius. The results of these simulations can be seen in Figure 5.2b, which are displayed as a

relative response compared to the effectively infinite cylinder. This simulation demonstrated that a height of 25 cm provides enough neutron moderation to achieve a detector response which is >99% of the response associated with the effectively infinite cylinder. Similarly, the radius of the cylinder was varied in order to determine the response of the internal detectors as a function of the cylindrical radius. Figure 5.2c shows that a cylindrical radius of 15 cm provides enough moderation to achieve an internal detector response which is >95% of the response associated with an effectively infinite cylinder.

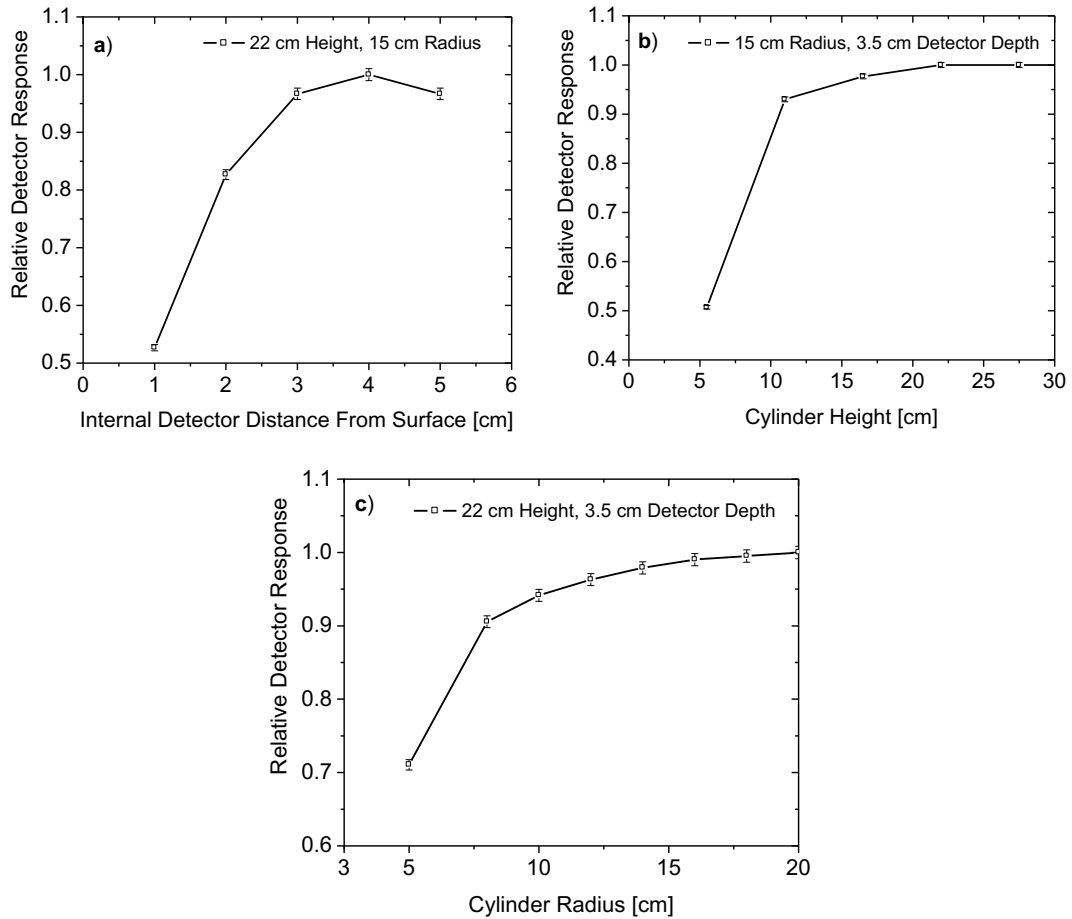


Figure 5.2: MCNP-simulated detector responses used to optimize the system’s dimensions. a) was used to determine the internal detector location ($r=11.5$ cm), b) the cylindrical height (15 cm), and c) the cylindrical radius (15cm).

5.1.2 Experiments with Different Neutron Spectra

Experiments were performed in order to demonstrate that the DSNDS can determine the relative angle of the source location and collect information about the energy spectrum of an unknown neutron source. The experimental configuration is represented by Figure 5.3, where RPI's DSNDS was positioned along with a ^{252}Cf source, which was suspended in the laboratory in one of three configurations: bare (no moderator), reflected, and moderated, which were created using a 5.08 cm (1") HDPE disk as a moderator and reflector. These three source configurations result in neutron spectra with decreasing fractions of fast neutrons. After these three measurements were performed and an empirical relationship was formed, a fourth spectrum was created in order to test the system's ability to measure an unknown neutron spectrum. The test source configuration was created by moderating the ^{252}Cf source with 1.27 cm (0.5") of HDPE. A final experiment was performed with a 5-cm Pb shield in front of the source in order to investigate the effect of a high-Z shield on the neutron spectrum.

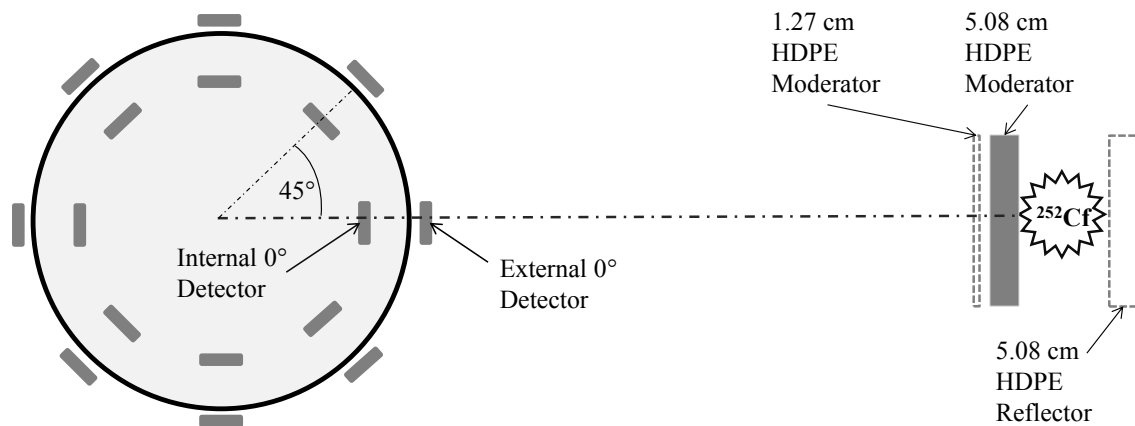


Figure 5.3: Experimental configuration used to represent laboratory experiments where the ^{252}Cf source was aligned with the 0° detectors of the DSNDS in one of four different source configurations: bare, moderated (5.08 cm HDPE), lightly moderated (1.27 cm HDPE), or reflected.

Each of the aforementioned measurements was performed with the source positioned 1.15 m away from the cylinder, aligned axially and laterally with the 0° detector. This source-detector distance was chosen to represent a survey measurement taken in a real-world situation, e.g. within a shipping container.

The source-detector distance affects the response of the DSND; for instance, increasing the distance increases the contribution of scattered neutrons from the surroundings, resulting in softer measured neutron spectra. This effect is difficult to account for because the DSND is sensitive to externally-scattered neutrons and it should be considered when interpreting the spectral results of the DSND. Additionally, when the distance between the source and the DSND is small, the external detectors become significantly closer to the source than the internal detectors, overestimating the hardness of the source. MCNP 6.1 simulations verified that the DSND would perform as designed when the source-detector distance is greater than 0.5 m.

Measurements performed with the DSND included a single detection disk (one internal and one external ring) and were not designed to investigate the system's ability to determine the relative height of a neutron source. However, MCNP simulations verify that varying the height of the source from $z=-1.0$ m to $z=1.0$ m does not change the calculated two-dimensional angle or hardness of the source spectrum when the source-detector distance is >0.5 m. Changing the height will decrease the absolute count rate due to the small solid-angle, which can be overcome by a longer counting time. Stacking multiple detection disks would provide the ability to gather information and quantify the relative height of the neutron source in a similar fashion to the method of determining the two-dimensional angle proposed in the subsequent section.

5.1.3 Determining the Source Spectrum

The neutron energy spectra of the three initial experimental source configurations were simulated with MCNP6.1 using a typical fission neutron energy spectrum. The MCNP inputs included the surrounding features of the laboratory, i.e. the concrete walls and floor, in order to represent external neutron scattering. The three source spectra represented in

Figure 5.4 were used to determine the fast neutron factor (FNF), which is defined as the fraction of neutrons above 1.0 eV, as seen in Table 5.1. The cutoff of 1.0 eV was chosen in order to effectively separate the neutron spectrum into two regions: the fast neutron region where neutrons are not fully moderated and the thermal neutron region where the neutron energy is defined by the Maxwell-Boltzmann distribution. The response of the DSNDs to the three characterized neutron spectra was used as a benchmark to characterize the system.

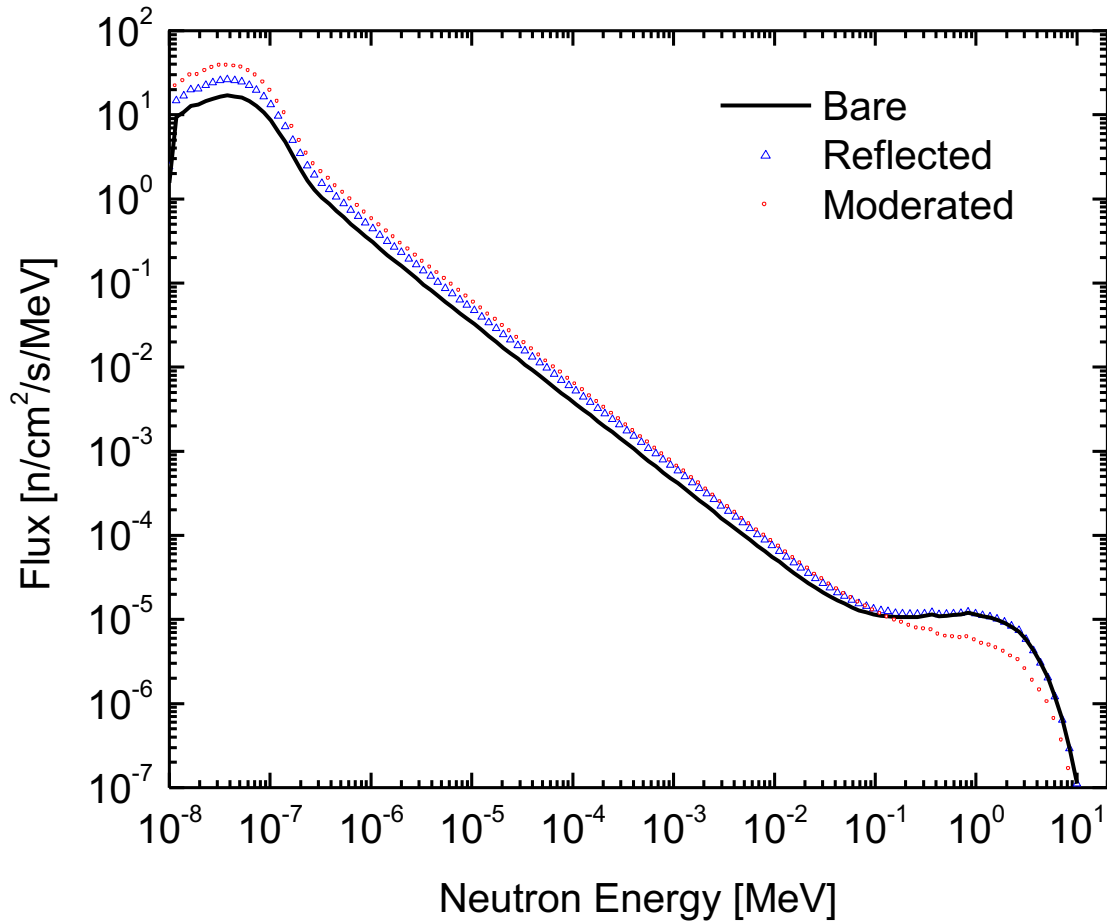


Figure 5.4: MCNP-simulated neutron flux per source neutron incident on the DSNDs corresponding to three ²⁵²Cf source configurations.

Table 5.1: Three source configurations characterized by the FNF: the fraction of neutrons above 1.0 eV.

Source	FNF (>1.0 eV)
Bare	0.95
Reflected	0.93
Moderated	0.85

The measured responses of the internal detectors were normalized to the 0° detector and are plotted as a function of the detector angular position in Figure 5.5.

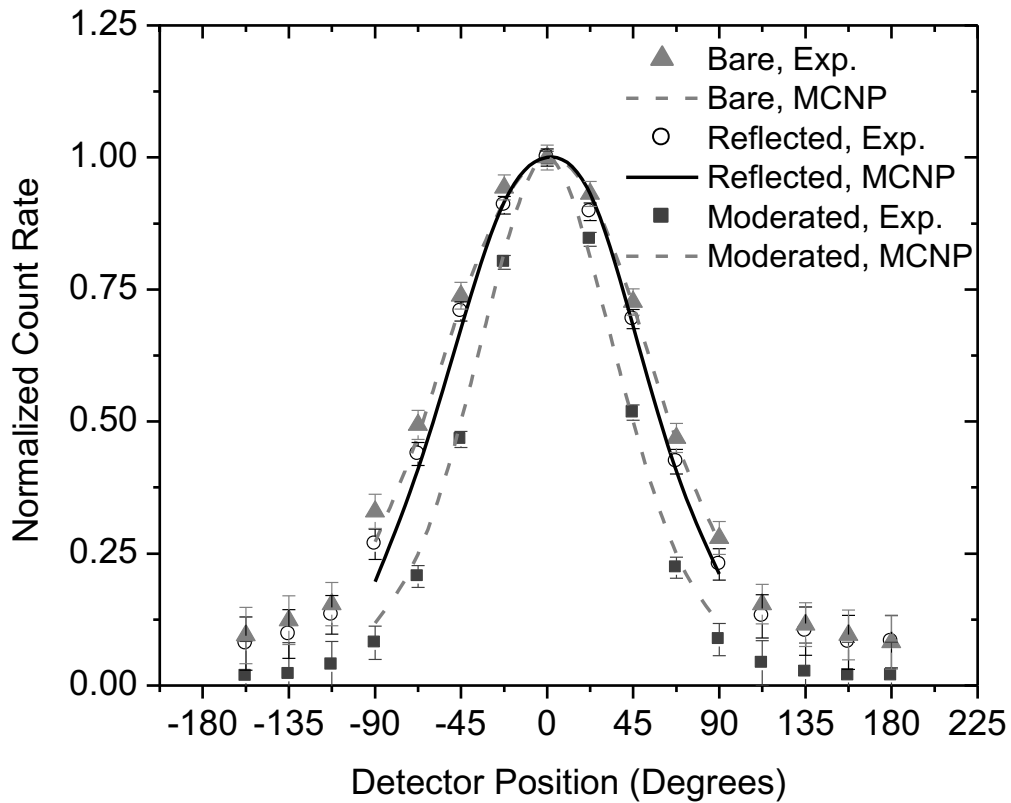


Figure 5.5: Experimental and MCNP-simulated distribution of the relative count rates of the internal ring of detectors corresponding to three source spectra.

The moderated source configuration has the softest energy spectrum and results in the narrowest distribution. Conversely, the bare source has the hardest spectrum and results in the broadest angular distribution. The reflected source, which has an intermediate spectrum, has a shape which lies between the moderated and bare source configurations,

evident in Figure 5.5. The normalized internal detector responses from Figure 5.5 were characterized by measuring the full width at half maximum (FWHM), which are shown in Table 5.2. This parameter provides useful information about the incident source spectrum; however, the distribution cannot be created immediately, as it requires statistically significant counts from multiple detectors. The measurements shown in Figure 5.5 were collected for 300 seconds with a distance of 1.15 m between the DSNDs and the ^{252}Cf source, resulting in 3,650 counts by the 0° internal detector and an average of 2,410 counts by the five highest-counting detectors (located at $\pm 90^\circ$, $\pm 45^\circ$, and 0°). The uncertainty of the measurements assumes Gaussian statistics, where the standard error is the square root of the counts for each data point.

A calculation was performed in order to determine the count time required to achieve an average uncertainty of $<15\%$ for each of the five detectors located at $\pm 90^\circ$, $\pm 45^\circ$, and 0° when the system is deployed 1.15 m from a given sample of SNM. Arbitrarily, a sample of 0.5 kg of weapons grade plutonium (93% ^{239}Pu and 7% ^{240}Pu) was chosen, which has a neutron emission rate of 3.6×10^4 n/s due to the spontaneous fission of ^{239}Pu and ^{240}Pu [43]. Based upon the count rates measured with the ^{252}Cf source and the relative strength of the arbitrary Pu sample, a measurement time of 830 seconds (13.8 minutes) would be required to achieve an uncertainty of $<15\%$ for each the five detectors between -90° and 90° .

A second spectral measurement involving the internal and external detectors was performed in order to provide an immediate analysis for real-time surveys. The internal-to-external ratio was calculated by dividing the summed response of the internal detectors by the summed response of the external detectors. The measured ratios of the internal-to-external detector responses with and without a Cd decoupler are shown in Table 5.2, along with the simulated FNF and the measured FWHM. The use of a Cd decoupler improves the system's sensitivity to variations in the hardness of the neutron spectrum. The FWHM for the three sources is shown in Figure 5.6a, and the internal-to-external ratio corresponding to the three sources is depicted in Figure 5.6b. The steep increase in the measured parameters (FWHM and Internal-to-External Ratio) above a FNF of 0.94 shows the sensitivity of the system to small changes in the neutron spectrum in this region; however, additional data would produce a smoother curve and provide a more accurate spectral quantification for an unknown neutron source.

Table 5.2: Simulated fast neutron factor (FNF) for three source configurations and the associated measured FWHM of the detector system’s normalized response and the internal-to-external detector ratios with and without the Cd decoupler.

Source	FNF	FWHM [°]	Internal-to-External Ratio with Cd	Ratio without Cd Decoupler
Bare ^{252}Cf	0.95	135±4	26.1±1.1	5.8±0.5
Reflected ^{252}Cf	0.93	120±4	11.9±0.3	4.1±0.4
Moderated ^{252}Cf	0.85	89±4	7.3±0.2	1.2±0.2

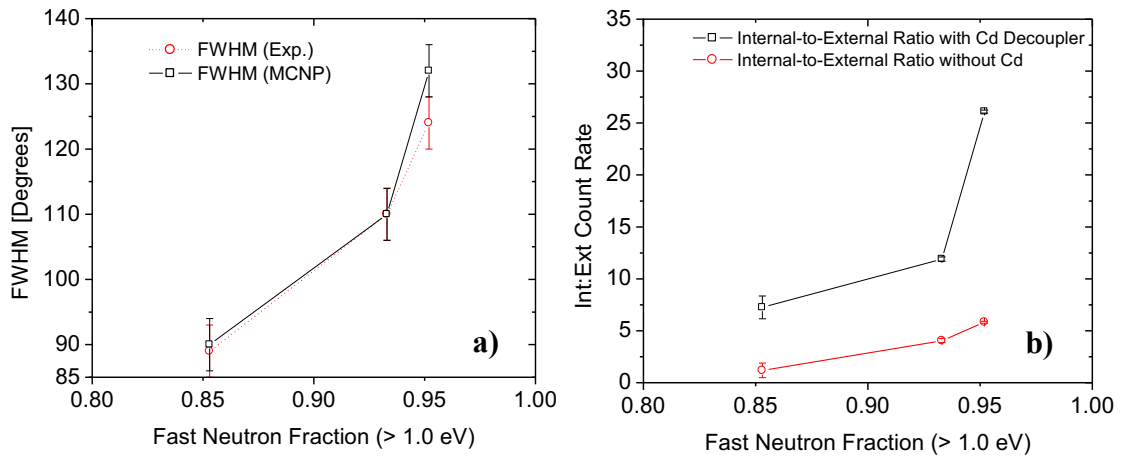


Figure 5.6: Empirical relationship between (a) the measured FWHM and FNF and (b) the measured Internal-to-External ratio and FNF.

A fourth neutron spectrum was measured with the DSNDS in order to test the sensitivity of the DSNDS to small changes in the neutron spectra and simulate the process of measuring an unidentified source. The measurement was performed with a Cd sheet surrounding the DSNDS in similar fashion to the three benchmark experiments. This test source configuration was created by moderating the ^{252}Cf source with a large, 1.27 cm (0.5”)-thick HDPE sheet (Figure 5.3). The FNF of this neutron spectrum was determined by MCNP simulation to be 0.94. This spectrum has a FNF, which lies between the bare ^{252}Cf and reflected ^{252}Cf source configuration (0.95 and 0.93, respectively); the simulated neutron spectra of the test source configuration and bare source configuration are shown in Figure 5.7.

The response of the internal detectors of the DSNDs corresponding to the test source configuration can be seen in Figure 5.8. This configuration yields a FWHM of $126^{\circ}\pm 4^{\circ}$ and an Internal-to-External ratio of 15.1 ± 0.2 ; both fall between the bare ^{252}Cf source and the reflected ^{252}Cf source. The empirical relationships created by the three original source configurations shown in Figure 5.6 were interpolated in order to quantify the FNF using the FWHM and Internal-to-External ratio measured from the DSNDs. The results are shown in Table 5.3, which demonstrates the relationship between the FNF determined by MCNP simulation and the Internal-to-External ratio and FWHM.

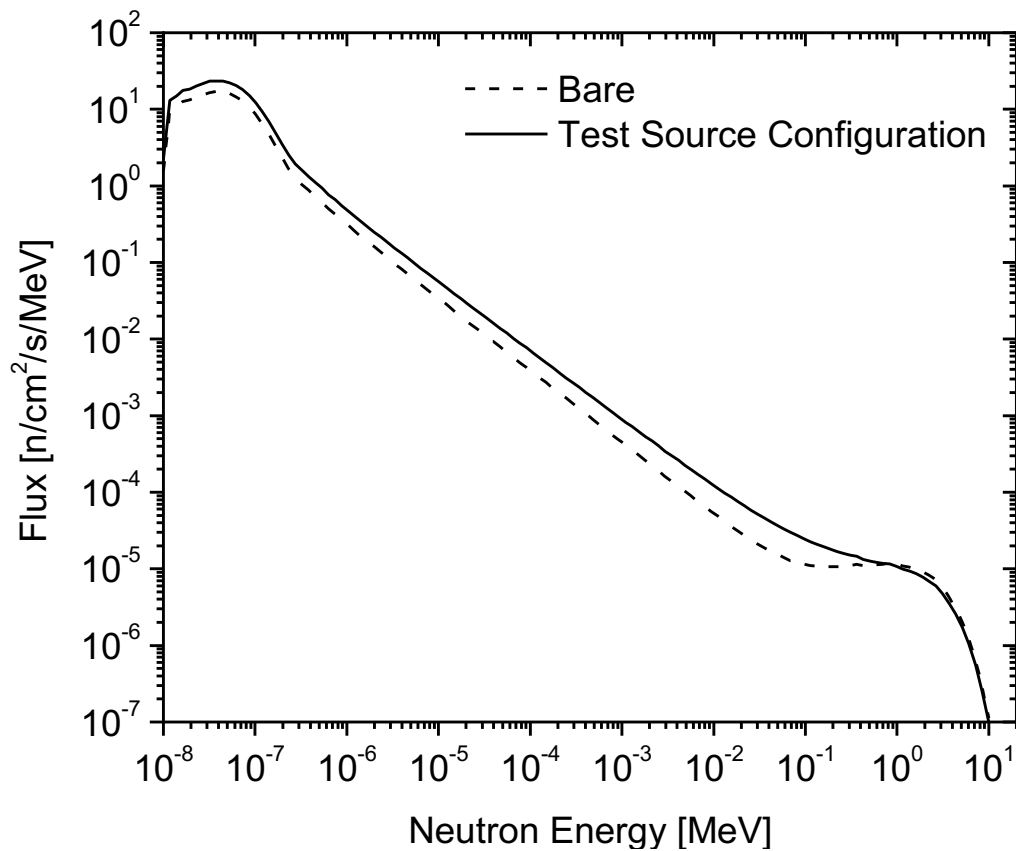


Figure 5.7: MCNP-simulated neutron flux per source neutron incident on the DSNDs corresponding to the bare source configuration and the test source configuration in which a ^{252}Cf source was moderated by 0.5” of HDPE.

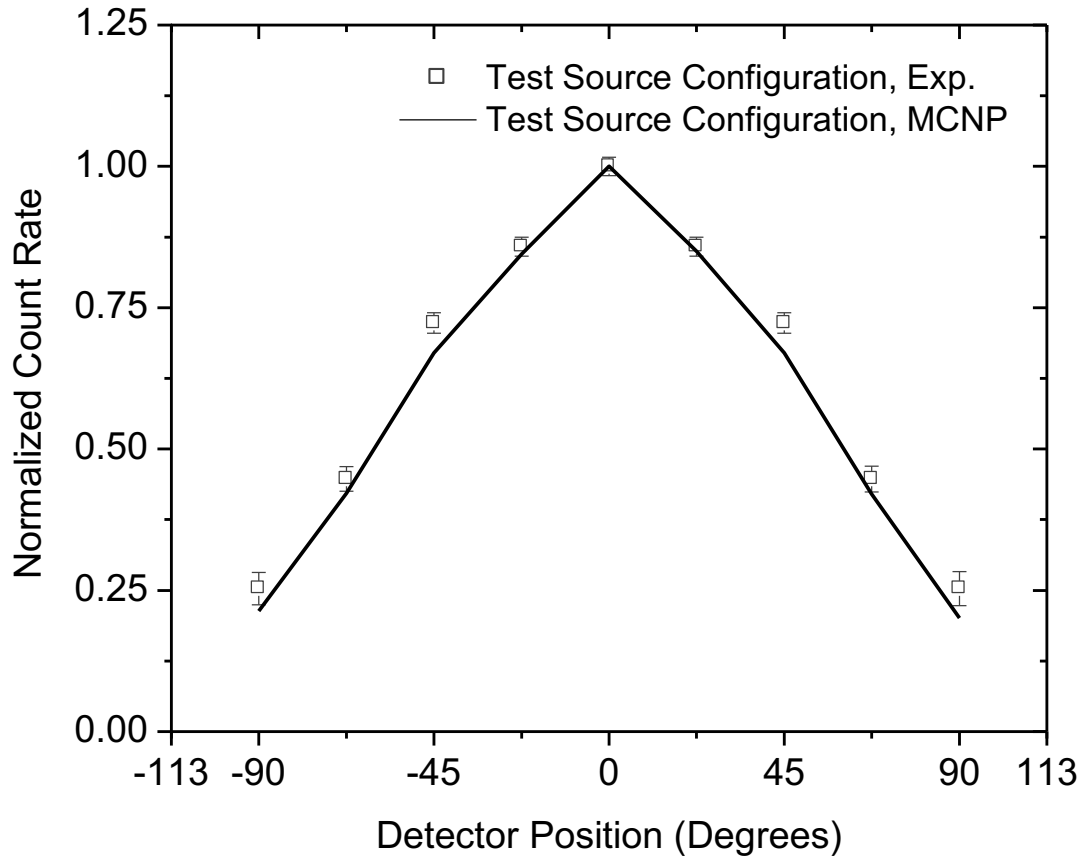


Figure 5.8: Experimental and simulated distribution of the relative count rates of the internal ring of detectors corresponding to the test source configuration.

Table 5.3: DSNDS response to a test neutron source configuration.

Source	Simulated FNF	Measured FWHM [°]	Interpreted FNF from Figure 7a	Measured Internal to External ratio	Interpreted FNF from Figure 7b
Test	0.94	126±4	0.94	15.1±0.2	0.94

These results demonstrate that the DSNDS is sensitive to small changes in a neutron energy spectrum by the determination of the FWHM and Internal-to-External ratio. Additionally, the information provided by the DSNDS can be used to determine the FNF of an unknown neutron spectrum by the interpolation of an empirical relationship created

from measurements with multiple known neutron spectra. Determining the FNF of a source using the DSNDs provides information about a potentially hidden neutron source. For instance, a large FWHM confirms that the source has a fast neutron fraction near unity, which indicates that a neutron source is relatively unmoderated. Conversely, a smaller fast neutron fraction indicates that a source is moderated.

An additional experiment was performed in order to investigate the effect of shielding a neutron source with a high-Z material. This experiment models the scenario where a sample of diverted SNM is shielded to prevent the discovery of the diverted material by gamma detection. This source configuration involved shielding the ^{252}Cf source with a 5-cm-thick Pb slab. The simulated spectrum corresponding to this configuration is normalized and compared to the bare ^{252}Cf source spectrum and can be seen Figure 5.9.

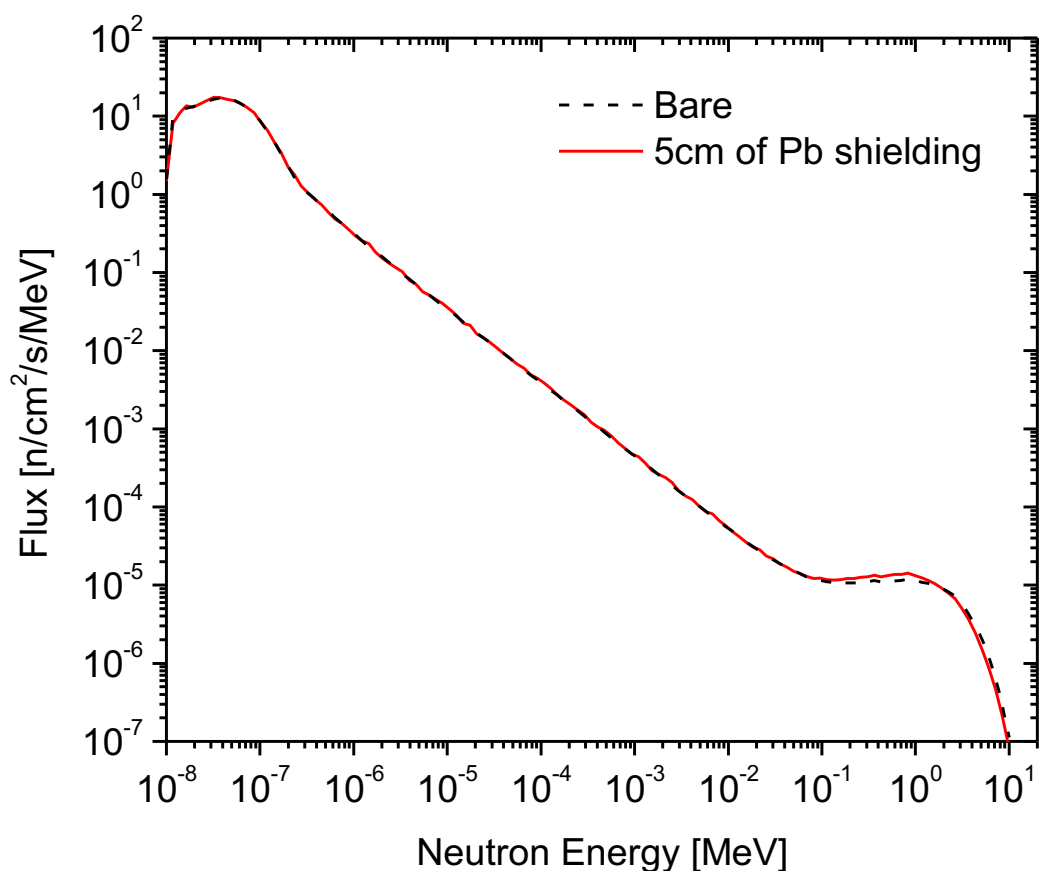


Figure 5.9: MCNP-simulated neutron flux per source neutron incident on the DSNDs corresponding to the ^{252}Cf source shielded with 5 cm of Pb, which is compared to the bare ^{252}Cf neutron spectrum.

The Pb-shielded spectrum is nearly indistinguishable to the bare ^{252}Cf source spectrum. The FNF was determined from the spectrum in Figure 5.9 to be 0.95. The FWHM and Internal-to-External ratio were determined experimentally, and Table 5.4 shows a comparison of the Pb-shielded source and the bare source spectra and the DSNDs-measured parameters. As expected, the Pb-shielded source results in similar values for the FWHM and Internal-to-External ratio since high-Z materials are poor neutron moderators.

Table 5.4: Comparison of Pb-shielded and bare ^{252}Cf source spectra and DSNDs-measured FWHM and Internal-to-External Ratio with the Cd decoupler.

Source	Simulated FNF	Measured FWHM [°]	Measured Internal-to-External Ratio with Cd Decoupler	Interpreted FNF from Figure 7a	Interpreted FNF from Figure 7b
Bare ^{252}Cf	0.95	132±4	26.1±1.1	0.95	0.95
Pb-shielded ^{252}Cf	0.95	130±4	25.4±1.3	0.95	0.95

5.1.4 Determination of the Source Angle and Resolution

The data collected from the DSNDs can be used to determine the angle between the detector system and the source, which can be used in order to determine the location of a hidden neutron source. The angle is determined by first identifying the detector with the greatest calibrated count rate; the angular position of this detector and its associated count rate are denoted Θ and $R(\Theta)$, respectively. Similarly, the detectors adjacent to Θ are termed $\Theta+\Delta\Theta$ and $\Theta-\Delta\Theta$, where $\Delta\Theta$ is the angular spacing between adjacent detectors. A linear interpolation given in equation 1 was performed on the normalized count rates to approximate the source angle corresponding to the peak of the count rate distribution. This angle indicates the direction of the neutron source. The linear interpolation uses the normalized count rates of the detectors adjacent to the detector with maximum count rate, $R(\Theta)$, which are denoted as $R(\Theta+\Delta\Theta)$ and $R(\Theta-\Delta\Theta)$.

$$Angle[^\circ] = \frac{R(\theta + \Delta\theta) - R(\theta - \Delta\theta)}{2 - [R(\theta + \Delta\theta) + R(\theta - \Delta\theta)]} * \frac{\Delta\theta[^\circ]}{2} + \theta[^\circ] \quad (14)$$

The angular resolution of the system is dependent on the incident neutron spectrum, the angular spacing of the detectors, the counting statistics of the system, and the empirical model used to quantify the angle. The angular resolution is impacted by the incident neutron spectrum because the spectral hardness affects the width of the distribution of the internal detectors' relative responses, as discussed in section 3.1 and seen in Figure 5.5. The wider distribution corresponding to a hard neutron spectrum will have a poorer angular resolution than the narrower distribution of a soft neutron spectrum. The angular spacing of the detectors in this system is 45°, but additional detectors could be used to reduce the spacing. Additional detection disks could also be stacked and offset by an angle of $\Delta\theta/n$, where n is the number of stacked disks, to improve the angular resolution of the DSND. The counting statistics of the system depend on the strength of the neutron source, the distance between the source and the DSND, the efficiency of the system, and the counting time.

Previous Monte Carlo simulations using MCNP6.1 modeled three source configurations of a fission neutron source at a distance of 1.15 m, aligned axially with the 0° detector. These simulations were described in detail in section 3.1, which demonstrated agreement with the experimentally-measured detector responses shown in Figure 5.5. The MCNP6.1 input files corresponding to the bare and moderated source configurations were used to model an internal ring of sixteen detectors with a symmetric angular spacing of 22.5°. Since the internal ring of detectors is symmetric, a shift in the distributed detector responses by 22.5° simulates a change in the source position of the same angle. These simulations were used to demonstrate the sensitivity of the DSND to a change in the relative source angle for the bare and moderated neutron source configuration and can be seen in Figure 5.10. The simulations were run with 10^8 histories with the source modeled 1.15 m from the DSND, which results in a maximum relative uncertainty of 5% for the five detectors between -90° and 90°.

In order to demonstrate the resolution of the DSNDs in a real-world scenario, the uncertainty of each detector response was calculated corresponding to the neutron emission of the SNM sample previously mentioned in section 3.1. The hypothetical 0.5 kg sample of weapons grade Pu emits 3.6×10^4 n/s, and it was previously determined that the measurement would take 830 seconds in order to achieve $<15\%$ uncertainty in the 5 detectors between -90° and 90° , resulting in 3×10^7 emitted neutrons. Previous experiments with the 0.13 mCi ^{252}Cf source at the same position for 300 seconds provided detector responses corresponding 3.6×10^8 emitted fission neutrons. The internal detector responses of these experiments were scaled in order to calculate the same detector responses associated with the Pu sample, which emits 3×10^7 neutrons in the aforementioned timeframe. The absolute uncertainty of each detector was calculated using the scaled detector responses, which are depicted by the error bars in Figure 5.10.

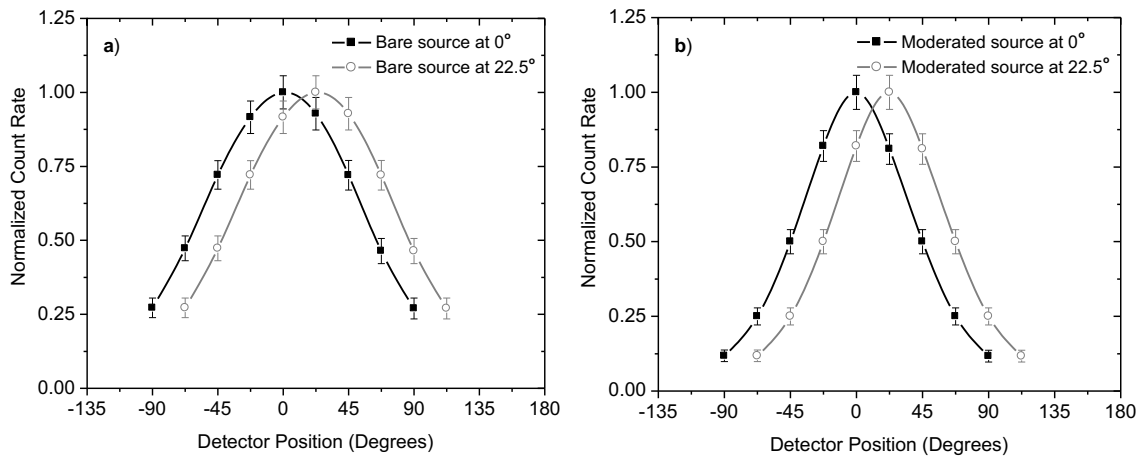


Figure 5.10: MCNP simulations demonstrating the sensitivity of the DSNDs to a 22.5° shift in the source angle with error bars corresponding to the ^{252}Cf source emitting 3×10^7 neutrons at the 1.15 m position for: a) the bare ^{252}Cf source and b) the ^{252}Cf source moderated by 5 cm of HDPE.

The shifted distributions in Figure 5.10a and Figure 5.10b show that the DSNDs is more sensitive to changes in the source position corresponding to the softer (moderated) neutron spectrum shown in Figure 5.10b. Table 5.5 contains the simulated detector responses corresponding to the bare and moderated source configuration with uncertainties calculated for two source strengths. The data demonstrates that the angular resolution of

the DSND is heavily dependent on the counting statistics of the individual detector responses.

Table 5.5: Tabulated results of the normalized, MCNP6.1-simulated internal detector responses used to determine the relative source angle using the linear interpolation of equation 1 and uncertainties corresponding to 3×10^7 emitted neutrons 1.15 m from the DSND.

Bare Source at 1.15m and 22.5°			Moderated Source at 1.15 m and 22.5°		
Detector Angle [°]	Uncertainties for SNM Sample (3×10^7 neutrons)	Uncertainties for ^{252}Cf Source (7.2×10^8 neutrons)	Detector Angle [°]	Uncertainties for SNM Sample (3×10^7 neutrons)	Uncertainties for ^{252}Cf Source (7.2×10^8 neutrons)
-45	0.47±0.06	0.47±0.01	-45	0.25±0.05	0.25±0.01
0	0.92±0.08	0.92±0.02	0	0.82±0.09	0.82±0.02
45	0.93±0.08	0.93±0.02	45	0.81±0.09	0.81±0.02
90	0.46±0.06	0.46±0.01	90	0.25±0.05	0.25±0.01
Predicted Source Angle	24°±26°	24°±8°	Predicted Source Angle	23°±12°	23°±3°

The angular resolution of the DSND using the linear interpolation model, eight internal detectors with an angular spacing of 45°, and counting statistics corresponding to 3×10^7 emitted neutrons at a distance of 1.15 m from the DSND results in a prediction of the source angle with a relatively large uncertainty: $\pm 26^\circ$ for a bare fission source and $\pm 12^\circ$ for a fission moderated by 5 cm of HDPE. This resolution is low, but the measurement still provides useful information about the position of a hidden neutron source. Experimental results corresponding to 7.2×10^8 emitted neutrons at a distance of 1.15 m from the DSND result in an angular uncertainty of $\pm 8^\circ$ and $\pm 3^\circ$ for the bare and moderated source configurations, respectively. The angular resolution and overall efficiency of the system can be improved by the addition of more detectors with reduced angular spacing. The modularity of this design allows for the DSND to be improved in order to meet specific target criteria, e.g. efficiency and angular resolution.

5.1.5 DSNDS Conclusions

The DSNDS has demonstrated the ability to provide information about the location and energy of an unidentified, hidden neutron source. This information is in the form of the relative source angle, which narrows down the location of a neutron source. This angle may provide adequate information to locate the source; however, more information may be useful if the source is not exposed. In this case, the spectral information can be used to determine how heavily the source is moderated. The level of moderation can provide information related to the amount of moderating material covering the source. The DSNDS is sensitive to shielding with hydrogenous material and relatively insensitive to high-Z attenuation. The system can provide spectral information with as few as two detectors, but the system has a modular design allowing for increased detection efficiency and angular granularity at the expense of increased cost.

The DSNDS was designed for, but not limited to, the effort to survey shipping containers for diverted SNM. This system was tested with a reasonable source-detector distance of 1.15 m, but simulations demonstrate that the system can operate at as calibrated at distances greater than 1.0 m. Additionally, it was demonstrated that the DSNDS can provide a spectral and positional analysis of an unidentified neutron source in minutes—depending on the source strength, source-detector distance, and source attenuation. A quicker measurement can be made using a supplementary spectral analysis utilizing the internal-to-external detector response ratio. The DSNDS could reduce the time associated with the process of surveying containers for diverted SNM, reducing the unwanted economic effects of monitoring millions of shipping containers for SNM annually. Further development of the DSNDS should include an investigation of the system's effectiveness and time-requirements with variable source strengths and in environments with background neutron radiation.

5.2 A Real-Time Personal Neutron Dosimeter

Neutron dosimetry involves the process of employing a neutron detection system in the presence of neutrons in order to determine the localized neutron dose rate, which is measured as the neutron dose equivalent in units of Sieverts/second (mrem/hour). A number of passive dosimeters have been widely used for personal neutron dosimetry,

including the solid-state track detector, the film badge, the neutron bubble dosimeter, and the thermo-luminescent dosimeter (TLD) [44]. These dosimeters are passive instruments because they do not provide any immediate feedback. Instead, these passive dosimeters are worn for a set period and are subsequently analyzed in order to determine the integrated personal neutron dose equivalent for the period which they were worn to ensure that the user does not exceed their annual dose limits. The need for a real-time, personal neutron dosimeter prompted the development of a commercially-available real-time neutron dosimeter which uses two solid-state diodes coated with a single layer of thermal and fast neutron-converting materials, respectively [45]-[46]. The low efficiency of planar solid-state detectors limits the sensitivity of such a dosimeter. The conception and recent improvements to microstructured SSNDs enable the development of a real-time personal neutron dosimeter with improved sensitivity.

A well-designed neutron dosimeter has an energy-dependent neutron response which is proportional to the ambient dose equivalent conversion factors reported in International Commission on Radiological Protection (ICRP) Publication 21 and 74 (Figure 5.11). These factors provide flux-to-dose conversion factors for neutrons of a wide energy range. A neutron dosimeter which has an energy-dependent response that is proportional to the flux-to-dose conversion factors has an ideal rem response and can accurately predict the neutron dose equivalent for the corresponding neutron energy range.

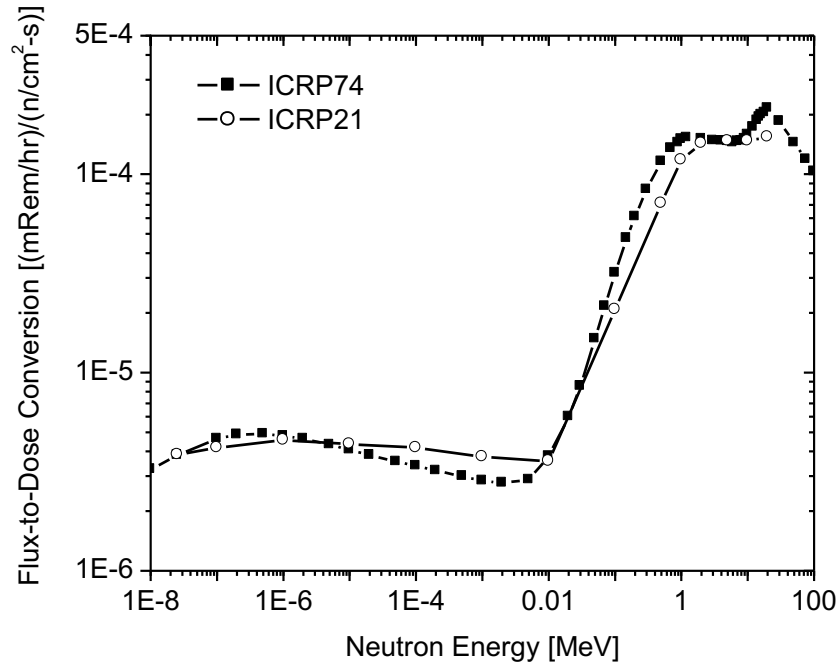


Figure 5.11: The neutron flux-to-dose equivalent conversion factors from ICRP Publications 21 (1973) and ICRP 74 (1996).

5.2.1 Dosimeter Simulation and Design

The real-time personal neutron dosimeter was designed using MCNP6.1 with the goal of achieving an energy-dependent response which matches the shape of the ideal rem response while maintaining adequate sensitivity and remaining compact enough to be worn on the body. The dosimeter uses both thermal and fast microstructured SSNDs, which were simulated as repeated lattice structures as outlined in previous sections.

This dosimeter is an albedo neutron dosimeter because it is designed to be worn on the body, which acts as a neutron moderator. Thus, the simulated dosimeter was positioned on the chest of an adult male computational human phantom. Simulations were performed with incremental, monoenergetic neutron sources placed 1.0 m from the dosimeter. The response of the fast detector was measured using a proton pulse-height (F8) tally, which recorded neutron events leading to a detectable signal in the charge-collecting Si. Similarly, the response of the thermal neutron detector was simulated using an alpha and heavy ion (lithium) pulse-height tally. In both cases, 200 keV was used as the lower level

of detection, which was previously determined by calibration of an experimental pulse height spectrum [13].

The thermal detector was surrounded by a small volume of high density polyethylene (HDPE)—a neutron moderator—and thin films of boron nitride—a thermal neutron absorber. These materials depressed the thermal neutron response of the dosimeter to better match the aforementioned ideal rem response. A schematic of the simulated dosimeter, as described, can be seen in Figure 5.12.

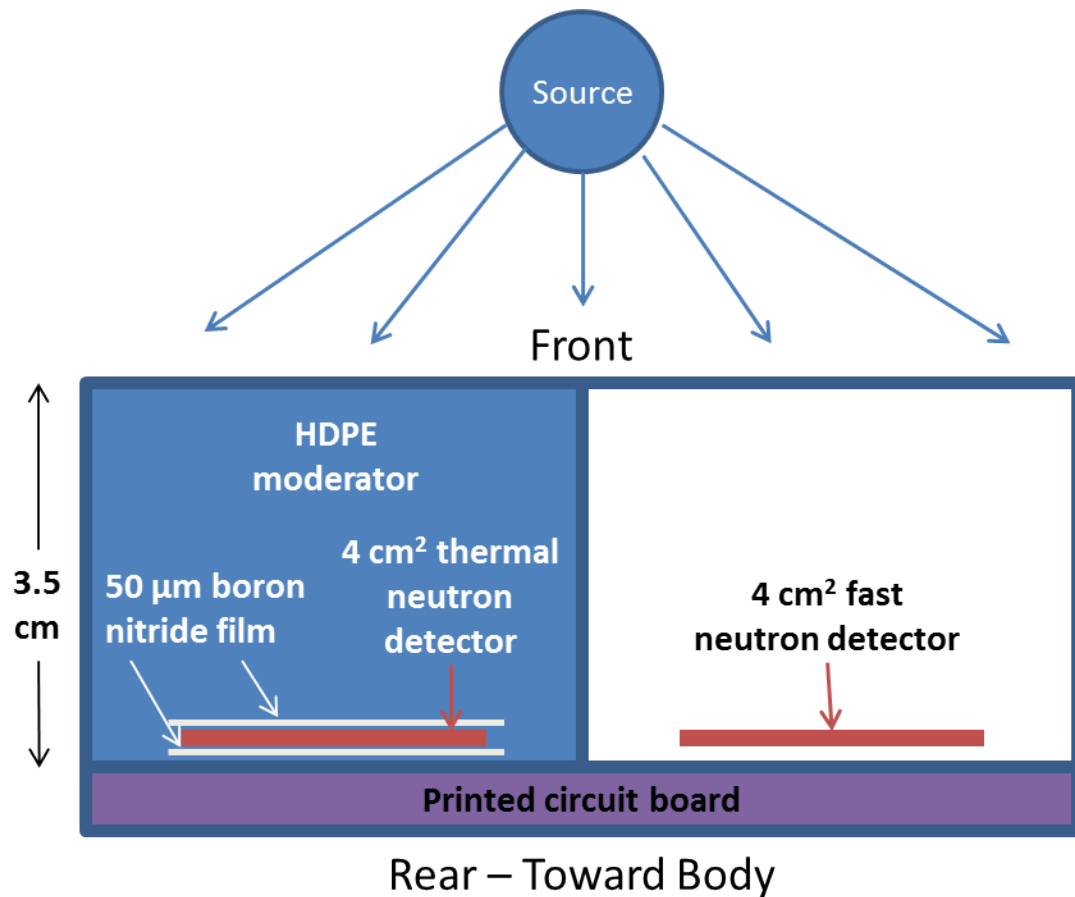


Figure 5.12: Top-view diagram of the simulated real-time personal neutron dosimeter using a fast and thermal microstructured SSND.

The individual MCNP-simulated responses of the fast and thermal microstructured detectors to incremental, monoenergetic neutron sources in the configuration illustrated by Figure 5.12 are shown in Figure 5.13. These responses demonstrate the hybrid design

of the dosimeter, which will use a combination of the fast and thermal detector responses to best match the ideal rem response.

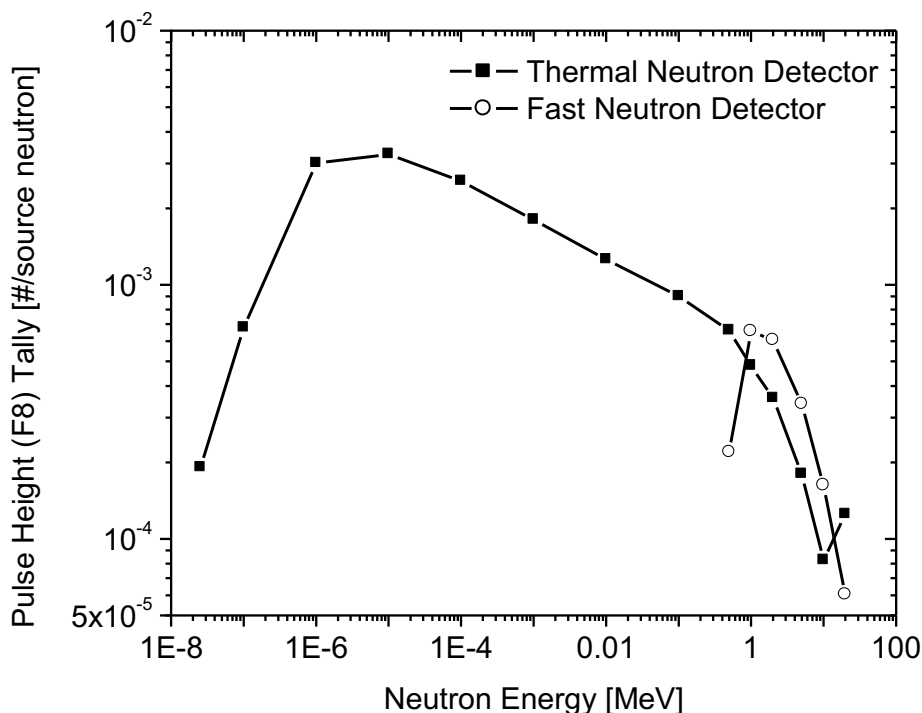


Figure 5.13. Simulated energy-dependent responses of the two detectors comprising the real-time dosimeter.

Three additional simulations were performed with incremental neutron spectra, including: a bare ^{252}Cf fission neutron source, a fission source moderated by 10 cm of HDPE, and a fission source moderated by 20 cm of HDPE in front of the source. These sources were chosen to represent typical neutron spectra a radiation worker would encounter and can be seen in Figure 5.14. The three source spectra were used in order to determine the appropriate scaling factors for the individual detector responses, which provide the most accurate dose equivalent response over a wide neutron energy range.

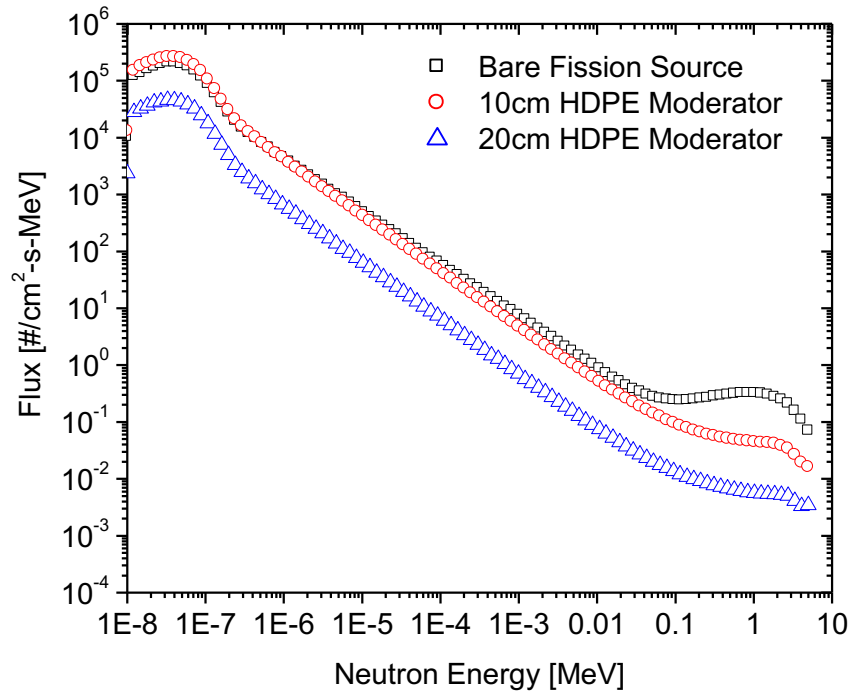


Figure 5.14. Simulated spectra of three sources used to calibrate the real-time personal neutron dosimeter.

The neutron dose equivalent incident on the face of the detector was simulated for the three aforementioned source spectra using MCNP's dose energy and dose function (DE and DF) modifier referencing ICRP 74; additionally, the responses of the individual detectors to the same spectra were tallied. A least squares fit was performed in order to determine the scaling factor for the fast and thermal detector. Figure 5.15 shows the shape of the scaled dosimeter response using the least squares analysis, which is compared to the aforementioned ideal rem response. Table 5.6 shows the accuracy of the dosimeter response to the three simulated source spectra.

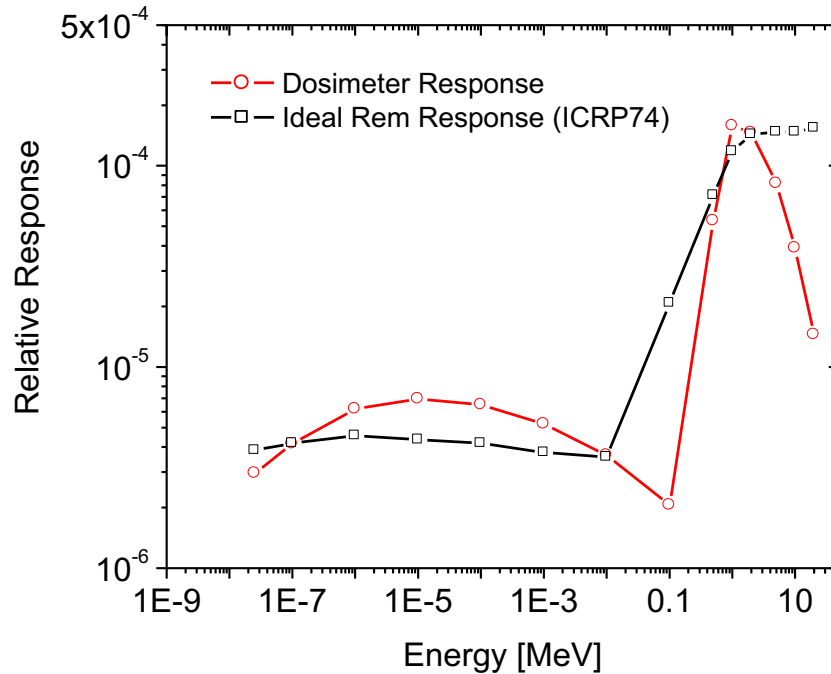


Figure 5.15. Response of the simulated real-time dosimeter compared to the ideal rem response according to ICRP 74.

Table 5.6. Comparison of the simulated real-time dosimeter response to the actual tallied dose.

Fission Source Configuration	Tallied Dose (ICRP 74) [mrem/n]	Dosimeter Response [mrem/n]	Simulated Dosimeter Accuracy
Bare	1.44×10^{-4}	1.41×10^{-4}	-2%
10 cm HDPE	8.56×10^{-6}	7.88×10^{-6}	-8%
20 cm HDPE	1.04×10^{-6}	1.16×10^{-6}	11%

The responses in Figure 5.15 illustrate that the designed dosimeter will over-estimate the dose to neutrons below 0.01 MeV. This is verified by the response of the simulated dosimeter to the fission source moderated by 20 cm of HDPE, which is 11% higher than the tallied dose. Conversely, the dosimeter measures a neutron dose equivalent, which is 2% and 8% lower than the actual tallied dose for the bare and 10cm-moderated source, respectively.

5.2.2 Real-Time Dosimeter Conclusions and Future Work

The fabrication of both fast and thermal microstructured SSNDs at RPI enables the development of a real-time personal neutron dosimeter which—according to MCNP simulations—can measure the neutron dose equivalent with reasonable accuracy for a wide range of neutron energies. The microstructured detectors have been experimentally characterized, and provide improved sensitivity compared to their planar detector counterparts.

Future work will involve constructing the real-time personal neutron using two 4 cm² detectors mounted on a printed circuit board with custom amplifiers, pulse shapers, and counters, which will communicate with an external application in order to calculate the measured dose equivalent. Experimental sensitivity measurements will be taken using a calibrated neutron source and calibrated neutron dosimetry instruments.

5.3 Pulsed Neutron Detectors

A solid-state pulsed neutron detector using silicon carbide diodes and a silver (Ag) activation foil was constructed. The first iteration of this device can be seen in Figure 5.16.

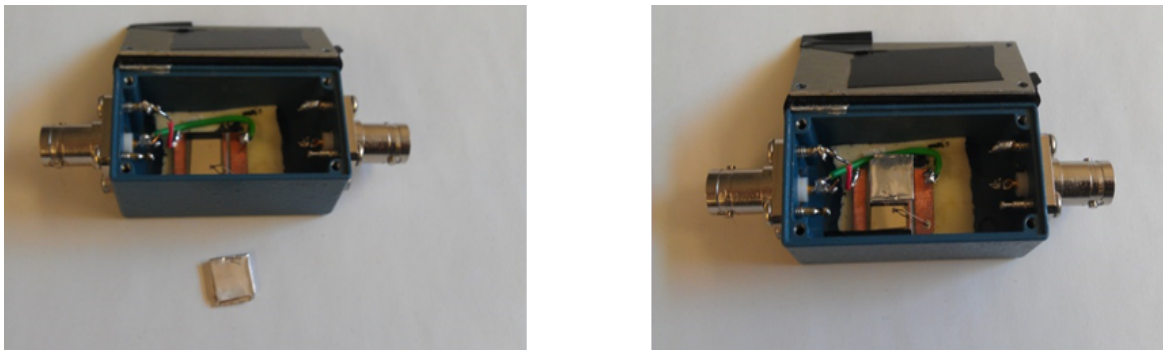
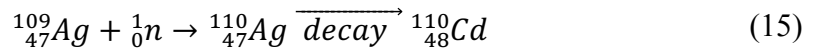


Figure 5.16: First SiC-Ag SSND used to measure neutrons from high-intensity pulsed neutron sources.

An Ag foil—which becomes activated in a neutron field—was sandwiched between two compact silicon carbide (SiC) charged particle detectors. The juxtaposition of the activation foil and the solid-state detectors allows for immediate detection of charged particle emission from the activated nuclei. The direct replacement of conventional

activation foils with this hybrid configuration is made possible by the use of SiC radiation detectors, which are compact and have demonstrated performance and robustness in high radiation conditions [47]-[50]. Packaging the activation foil and solid-state detectors into a single apparatus eliminates the need to remove the foil after activation for subsequent analysis. Instead, the SiC devices are in position for immediate measurement of the activation product's activity after irradiation, eliminating the delay between activation and subsequent analysis. This design allows data to be collected in real-time immediately following neutron activation. Additionally, the dramatic reduction in delay time allows for the utilization of Ag foils, which have a short-lived activation product. Therefore, Ag foils reach their saturation activity faster and require less counting time after activation to achieve similar sensitivity.

The isotope of interest in Ag activation foils is ^{109}Ag , which makes up 48.2 % of naturally occurring Ag. This isotope has a thermal capture cross section of 87 barns which results in isomeric ^{110}Ag . The isomeric state of ^{110}Ag undergoes beta decay with a half-life of 24.6 seconds. The maximum energy of the emitted electron is 2.89 MeV ($E_{\text{avg}}=1.17$ MeV) [43]. The reaction is shown in Equation 13.



Measurement of high-intensity neutron pulses—which has important applications in fields such as radiation protection, accelerator systems, and criticality excursion measurements—were taken with two sources. A moderated ^{252}Cf spontaneous fission neutron source was used to calibrate the sensitivity of the detection system, and an accelerate-driven pulsed neutron source was used to test the feasibility of the system to LINAC conditions.

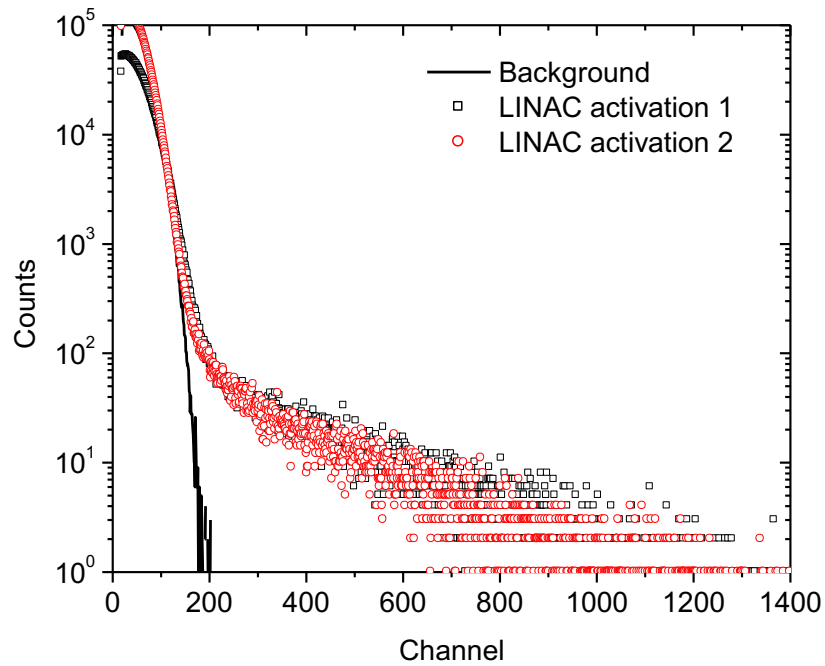


Figure 5.17: SiC-Ag detector response to two activation measurements taken with the RPI LINAC at $F=180$ Hz, $I=5$ μ A.

Research will continue to calibrate the sensitivity of the device, develop to apply the system to dosimetry and spectroscopy measurements, and look for opportunities to continue to develop a real-time pulsed neutron detection system with silver and silicon carbide.

6. Conclusions

Multiple, novel applications of microstructured SSNDs are presented in this thesis. The Directional and Spectral Neutron Detection System demonstrates the capability to gather real-time spectral and positional information about an unidentified neutron source. The compact size and zero bias requirement of the microstructured SSNDs provide the system with modularity and enhanced portability. The scalability of the SSNDs allows for the detectors' angular spacing and total area to be customized for specific design goals. Additionally, a real-time personal neutron dosimeter—relying on a fast and thermal microstructured SSND—can be used to accurately monitor neutron dose rates for a wide energy range. This system relies on the improved sensitivity of microstructured SSNDs and demonstrates the portability and versatility of neutron systems using these devices.

These microstructured SSNDs, which were developed at RPI in multiple design iterations, provided novel and cost-effective neutron detectors for the aforementioned applications. Well-designed SSNDs with continuous p-n junctions operated at zero bias with low noise levels. Honeycomb microstructured SSNDs achieved an intrinsic thermal neutron efficiency of 29% with adequate gamma insensitivity because of customized preamplifiers and improved microstructure designs determined using Monte Carlo simulations. MCNP simulations optimized the microstructure sizing for different detector applications based on detector noise levels. For example, the optimal design of a honeycomb SSND with a noise level of 200 keV results in an optimal simulated intrinsic thermal neutron efficiency ($E_n=0.0253$) of 43% with a hexagonal diameter of 4 μm and a Si wall thickness of 1 μm . Increasing the noise level to 500 keV will significantly reduce the simulated efficiency of this device to 27%. However, optimizing the microstructure for this 500 keV noise level, results in an efficiency of 37% corresponding to a hexagonal diameter of 2.5 μm and a Si wall thickness of 1.25 μm . The microstructure optimization demonstrates the benefit of customizing the design for various applications based on the noise level. Additionally, the development of customized preamplifiers further reduced the noise level of the devices, which significantly improved the detection efficiency. Furthermore, trench microstructured SSNDs were designed and fabricated with more cost-effective processes and materials, resulting in less expensive thermal neutron detectors with high efficiency

and adequate—yet elevated—gamma insensitivity. Overall, the development and customization of microstructured SSNDs for neutron detection applications demonstrates tremendous potential to reduce the cost and expand the capabilities of current neutron detection systems.

REFERENCES

- [1] United States Nuclear Regulatory Commission, "Transportation of spent nuclear fuel," 2012. [Online]. Available: <http://www.nrc.gov/waste/spent-fuel-transp.html>, Accessed on: Aug. 3, 2014.
- [2] T. W. Crane and M. P. Baker, "Neutron detectors," in *Passive Nondestructive Assay of Nuclear Materials*. Los Alamos National Laboratory, Los Alamos, NM, USA, LA-UR-90-732, 1991, pp. 379-406. [Online]. Available: http://www.lanl.gov/orgs/n/n1/FMTTD/neut_mc/pdfs/LA_UR_90_0732.pdf, Accessed on: Jun. 13, 2015.
- [3] C. Petrillo, F. Sacchetti, O. Toker and N. J. Rhodes, "Solid state neutron detectors," *Nucl. Instruments and Methods in Physics Res. A*, vol. 378, pp. 541-551, Aug. 1996. [Online]. Available: <http://www.sciencedirect.com/science/article/pii/S0168900296004871>, Accessed on: Nov. 11, 2015.
- [4] A. Rose, "Sputtered boron films on silicon surface barrier detectors," *Nucl. Instruments and Methods in Physics Res. A*, vol. 52, pp. 166-170, June 1967. [Online]. Available: <http://www.sciencedirect.com/science/article/pii/S0029554X67905769>, Accessed on: Dec. 1 2015.
- [5] R. Jeter and M. Kennison, "Recent improvements in helium-3 solid state neutron spectrometry," *IEEE Trans. on Nucl. Sci.*, vol. 4, pp. 422-427, June 1967.
- [6] K. Velbeck *et al.* "A solid state neutron detector," *IEEE Trans. on Nucl. Sci.*, vol. 31, pp. 360-361, Feb. 1984.
- [7] F. Shiraishi *et al.*, "A new type personnel neutron dosimeter with thin Si detectors," *IEEE Trans. on Nucl. Sci.*, vol. 35, pp. 575-578, Feb. 1988.
- [8] A. Miresghi *et al.*, "Amorphous silicon position sensitive neutron detector," *IEEE Trans. on Nucl. Sci.*, vol. 39, pp. 635-640, Aug. 1992.
- [9] S. Harrison, "Semiconductor-based thermal neutron detectors," Stanford University, Feb. 2013. [Online]. Available: <http://large.stanford.edu/courses/2013/ph241/harrison1/>, Accessed on: Jan. 14, 2017.

- [10] R. A. Rydin, "Design considerations for a semiconductor sandwich fast neutron spectrometer," *IEEE Trans. on Nucl. Sci.*, vol. 14, pp. 377-392, Feb. 1967.
- [11] D. McGregor, S. Bellinger and K. Shultis, "Present status of microstructured semiconductor neutron detectors," *J. of Crystal Growth*, vol. 379, no. 15, pp. 99-110, Sept. 2013. [Online]. Available: <http://www.sciencedirect.com/science/article/pii/S0022024812009864>, Accessed on: Mar. 29, 2016.
- [12] R. Nikolic, C. Cheung, C. Reinhardt and T. Wang, "Future of semiconductor based thermal neutron detectors," Lawrence Livermore National Lab, CA, USA, UCRL-PROC-219274, 2006. [Online]. Available: <http://digitalcommons.unl.edu/cgi/viewcontent.cgi?article=1013&context=chemistrycheung>, Accessed on: Feb. 11, 2015.
- [13] K.-C. Huang, R. Dahal, J. Lu, A. Wertz, Y. Danon and I. Bhat, "Scalable large-area solid-state neutron detectors with continuous p-n junction and extremely low leakage current," *Nucl. Instruments and Methods in Physics Res. A*, no. 763, pp. 260-265, Nov. 2014.
- [14] J. Clinton, "Optimization and characterization of a novel self powered solid state neutron detector", Ph.D. dissertation, MANE Dept., RPI, Troy, NY, 2011.
- [15] F. Wald and J. Bullitt, *Semiconductor Neutron Detectors*. Waltham, MA, USA: Defense Technical Information Center, 1973, pp 11-24.
- [16] S. Adenwalla, P. Welsch, A. Harken, J. I. Brand and A. Sezer, "Boron/n-silicon carbide heterojunction diodes," *Applied Physics Lett.*, vol. 79, no. 26, pp. 4357-4359, 2001.
- [17] D. S. McGregor, T. C. Unruh and W. J. McNeil, "Thermal neutron detection with pyrolytic boron nitride," *Nucl. Instruments and Methods in Physics Res. A*, vol. 591, no. 3, pp. 530-533, 2008.
- [18] F. P. Doty, "Advanced digital detectors for neutron imaging," Sandia National Laboratories, Livermore, NM, USA, SAND2003-8796, 2003. [Online]. Available: <http://prod.sandia.gov/techlib/access-control.cgi/2003/038796.pdf>, Accessed on: Nov. 1, 2015.

- [19] P. Lunca-Popa *et al.*, "Evidence for multiple polytypes of semiconducting boron carbide (C₂B₁₀) from electronic structure," *J. of Physics D: Applied Physics*, vol. 38, pp. 1248-1252, 2005.
- [20] S. Majety *et al.*, "Metal-semiconductor-metal neutron detectors based on hexagonal boron nitride epitaxial layers," *SPIE Hard X-Ray, Gamma-Ray, and Neutron Detector Physics*, vol. 8507, Oct. 2012, doi:10.1117/12.940748, [Online]. Available: <https://pdfs.semanticscholar.org/8999/4efd33e263d3c1243c03e9e55ef988583c83.pdf>, Accessed on: Aug. 11, 2015.
- [21] Boron nitride solid state neutron detector, by P. F. Doty. (2004, April 11). US Patent 6727504, Apr. 2004. [Online]. Available: <https://www.google.com/patents/US6727504>, Accessed on: Oct. 14, 2016.
- [22] J. Yazbeck, "Investigations of hexagonal boron nitride as a semiconductor for neutron detection," M.S. thesis, Kansas State Univ., Manhattan, KS, 2009.
- [23] J. H. Edgar and T. Hoffman, "Synthesis of large single crystals of boron nitride for electronic and photonic applications," *SPIE Newsroom*, Mar. 2016. Accessed on: April 29, 2016, doi: 10.1117/2.1201602.006302, [Online]. Available: <http://spie.org/newsroom/6302-synthesis-of-large-single-crystals-of-boron-nitride-for-electronic-and-photonic-applications>, Accessed on: Sept. 4, 2016.
- [24] T. C. Doan, J. Li, J. Y. Lin and H. X. Jiang, "Growth and device processign of hexagonal boron nitride epilayers for thermal neutron and deep ultraviolet detectors," *Amer. Inst. of Physics Advances*, vol. 6, no. 7, Jul. 2016. [Online]. Available: <http://aip.scitation.org/doi/full/10.1063/1.4959595>, Accessed on: Dec. 13, 2016.
- [25] R. Dahal *et al.*, "Anisotropic charge carrier transport in free-standing hexagonal boron nitride thin films," *Appl. Physics Express*, vol. 9, no. 6, May 2016. [Online]. Available: <http://iopscience.iop.org/article/10.7567/APEX.9.065801>, Accessed on: Dec. 19, 2016.
- [26] A. Maity, T. Doan, J. Y. Li, J. Lin and H. X. Jiang, "Realization of highly efficient hexagonal boron nitride neutron detectors," *Appl. Physics Lett.*, vol 109, no. 7, Aug. 2016. [Online]. Available: <http://aip.scitation.org/doi/abs/10.1063/1.4960522?journalCode=apl>, Accessed on: Dec. 12, 2016.

- [27] K. Ahmed *et al.*, "Growth of hexagonal boron nitride on (111) Si for deep UV photonics and thermal neutron detection," *Appl. Physics Lett.*, vol. 109, no. 11, Sept. 2016. [Online]. Available: <http://aip.scitation.org/doi/abs/10.1063/1.4962831?journalCode=apl>, Accessed on: Jun. 13, 2017.
- [28] K.-C. Huang, R. Dahal, J. Lu, Y. Danon and I. Bhat, "High detection efficiency micro-structured solid-state neutron detector with extremely low leakage current fabricated with continuous p-n junction," *Appl. Physics Lett.*, vol 102, no. 15, Apr. 2013. [Online]. Available: <http://aip.scitation.org/doi/abs/10.1063/1.4802204?journalCode=apl>, Accessed on: Dec. 3, 2014.
- [29] F. Laermer, A. Urban and R. Bosch, "Milestone in deep reactive ion etching," presented at 2005 Proc. of the Int. Conf. on Solid-State Sensors, Actuators and Microsystems. [Online]. Available: <http://ieeexplore.ieee.org/document/1497272/>, Accessed on: Jan. 23, 2016.
- [30] J.-W. Wu *et al.*, "Boron-10 nanoparticles filled silicon trenches for thermal neutron detection applications," *Appl. Physics Lett.*, vol. 110, no. 19, May 2017. [Online]. Available: <http://aip.scitation.org/doi/abs/10.1063/1.4983289?journalCode=apl>, Accessed on: Aug. 7, 2016.
- [31] J. Goorley *et al.*, "Initial MCNP6 release overview - MCNP6 version 1.0" Los Alamos National Laboratory, Los Alamos, NM, USA, LA-UR-13-22934, 2013. [Online]. Available: <http://permalink.lanl.gov/object/tr?what=info:lanl-repo/lareport/LA-UR-13-22934>, Accessed on: Dec. 13, 2013.
- [32] G. F. Knoll, "Semiconductor diode detectors," in *Radiation Detection and Measurement*, 4th ed., Hoboken, NJ, USA: John Wiley & Sons, Inc., 2010, ch. 11, pp. 365-411.
- [33] ORTEC. (2002). *Model 142AH Preamplifier Operating and Service Manual*. [Online]. Available: <https://www.ortec-online.com/-/media/ametekortec/manuals/142abc-mnl.pdf>, Accessed on: Apr. 15, 2015.
- [34] AMETEK. *142A/B/C Preamplifier Datasheet*. [Online]. Available: <http://www.ortec-online.com/products/electronics/preamplifiers/142a-b-c>, Accessed on May 1, 2016.

- [35] Mirion Technologies. (2007). *Model 2004 Semiconductor Detector Preamplifier Datasheet*. [Online]. Available: http://www.canberra.com/products/radiochemistry_lab/pdf/Model-2004-SS.pdf, Accessed on May 13, 2016.
- [36] E. English *et al.*, "Low-noise preamplifier design consideration for large area high capacitance solid-state neutron detectors," *IEEE Trans. on Nucl. Sci.*, vol. 63, no. 1, pp. 304-315, Feb. 2016.
- [37] Saint Gobain. (2006). *Lithium Glass Scintillators*. [Online]. Available: http://www.crystals.saint-gobain.com/Lithium_Glass_Scintillators.aspx, Accessed on: May 13, 2016.
- [38] O. L. Andreev, A. E. Kochin, G. M. Stukov and I. A. Yaritsyna, "Absolute measurement of the yield of a neutron source by the gold-foil activation method," *Atomic Energy*, vol. 16, no. 3, pp. 304-305, 1964.
- [39] Y. A. Prokof'ev, P. E. Spivak, E. V. Rogov and L. N. Bondarenko, "Error analysis in reactor-core neutron beam density measurement by gold-foil activation," *Atomic Energy*, vol. 60, no. 3, pp. 205-208, Mar. 1986.
- [40] K. R. Kase *et al.*, "Neutron fluence and energy spectra around the varian clinac 2100C/2300C medical accelerator," *Health Physics*, vol. 74, no. 1, pp. 38-47, Jan. 1998.
- [41] S. Vaughn, "Investigation of a passive, temporal, neutron monitoring system that functions within the confines of START I", M.S. thesis, "Air Force Inst. of Technol., Wright-Patterson Air Force Base, Ohio, 2003.
- [42] R. Kouzes *et al.*, "Alternative neutron detection testing summary," Pacific Northwest National Laboratory, Richland, WA, USA, PNNL-19311, 2010. [Online]. Available: http://www.pnl.gov/main/publications/external/technical_reports/PNNL-19311.pdf, Accessed on: Nov. 25, 2016.
- [43] R. B. Firestone, *Table of Isotopes*, 8th ed., Berkeley, CA, USA: John Wiley & Sons, Inc., 1996.
- [44] J. A. B. Gibson, "Individual neutron dosimetry," *Radiation Protection Dosimetry*, vol. 23, pp. 109-115, Jun. 1988.

- [45] M. Sasaki, T. Nakamura, N. Tsujimura, O. Ueda and T. Suzuki, "Development and characterization of real-time personal neutron dosimeter with two silicon detectors," *Nucl. Instruments and Methods in Physics Res. A*, vol. 418, no 2-3, pp. 465-475, Dec. 1998.
- [46] T. Nakamura, M. Horiguchi, T. Suzuki and T. Yamano, "A real time wide energy range personal neutron dosimeter with two silicon detectors," *Radiation Protection Dosimetry*, vol. 27, no. 3, pp. 149-156, May 1989.
- [47] A. Dulloo *et al.*, "Simultaneous measurement of neutron and gamma-ray radiation levels from a TRIGA reactor core using silicon carbide semiconductor detectors," *IEEE Trans. on Nucl. Sci.*, vol. 46, no. 3, pp. 275-279, Jun. 1999.
- [48] S. Metzger, H. Henschel, O. Kohn and W. Lennartz, "Silicon carbide radiation detector for harsh environments," *IEEE Trans. on Nucl. Sci.*, vol. 49, no. 3, pp. 1351-1355, Dec. 2002.
- [49] F. Nava *et al.*, "Radiation tolerance of epitaxial silicon carbide detectors for electrons, protons, and gamma-rays," *Nucl. Instruments and Methods in Physics Res. A*, vol. 505, no. 3, pp. 645-655, Jun. 2003.
- [50] F. Nava, G. Bertuccio, A. Cavallini, and E. Vittone, "Silicon carbide and its use as a radiation detector material," *Measurement Sci. and Technol.*, vol. 19, no. 10, Aug. 2008.

Appendix A: Contour plots used to optimize the geometry of microstructured devices with various design and neutron-converting materials.

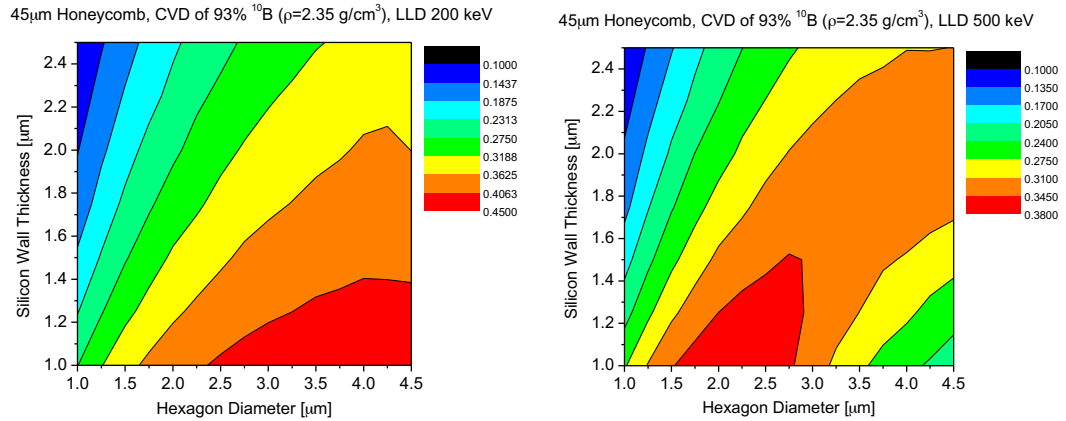


Figure A.1: Contour plot showing the simulated thermal neutron efficiency as a function of the hexagonal diameter and silicon wall thickness of a 45 μm-deep honeycomb device filled via CVD of boron (ρ=2.35 g/cm³) and an LLD of 200 keV (left) and 500 keV (right).

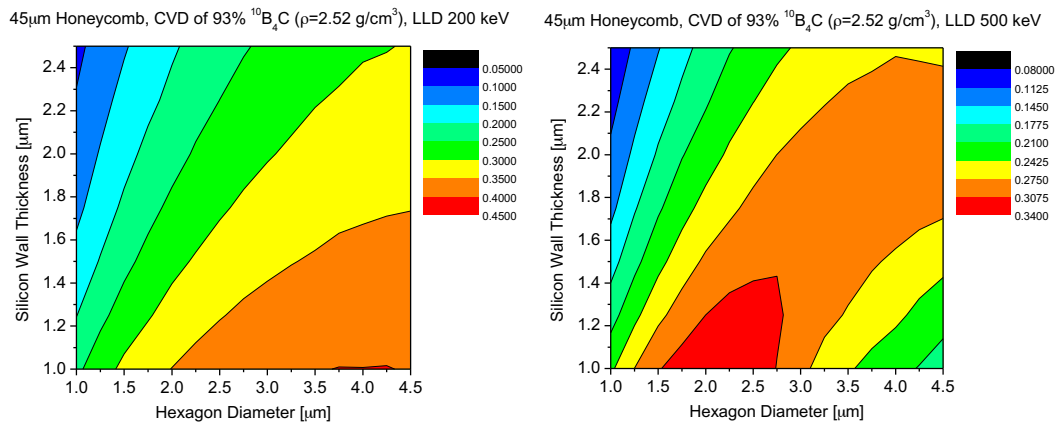


Figure A.2: Contour plot showing the simulated thermal neutron efficiency as a function of the hexagonal diameter and silicon wall thickness of a 45 μm-deep honeycomb device with CVD boron carbide (ρ=2.52 g/cm³) and an LLD of 200 keV (left) and 500 keV (right).

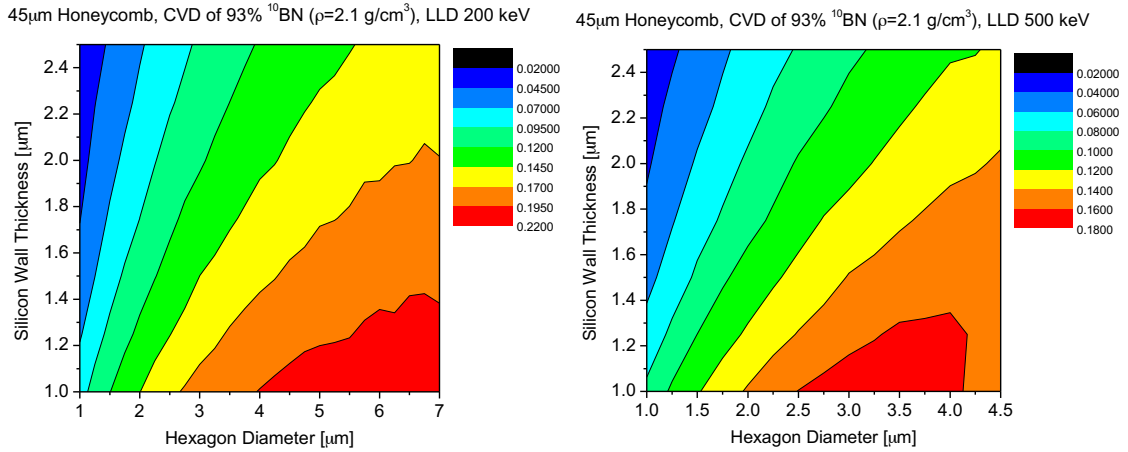


Figure A.3: Contour plot showing the simulated thermal neutron efficiency as a function of the hexagonal diameter and silicon wall thickness of a 45 μm-deep honeycomb device filled via CVD of boron nitride (ρ=2.1 g/cm³) and an LLD of 200 keV (left) and 500 keV (right).

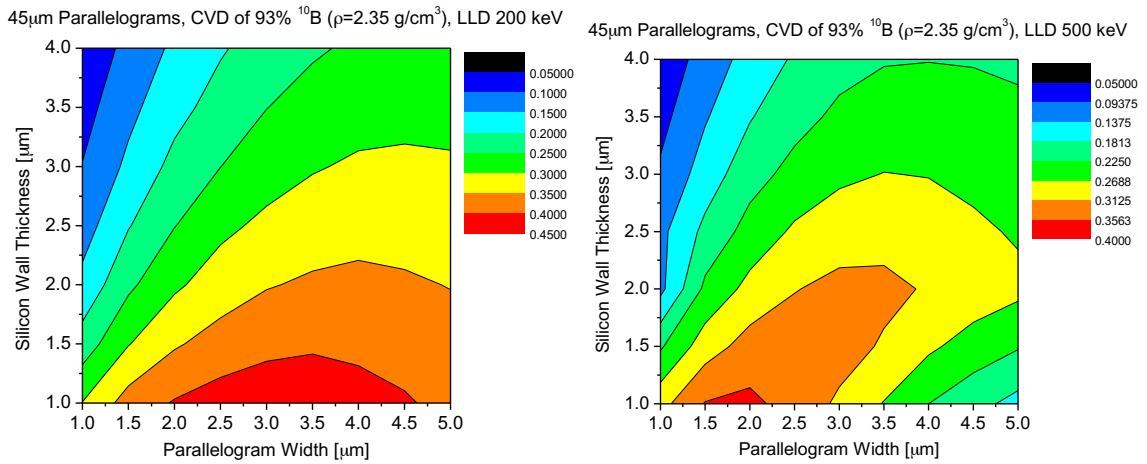


Figure A.4: Contour plot showing the simulated thermal neutron efficiency as a function of the parallelogram width and silicon wall thickness of a 45 μm-deep parallelogram device filled via CVD of boron (ρ=2.35 g/cm³) and an LLD of 200 keV (left) and 500 keV (right).

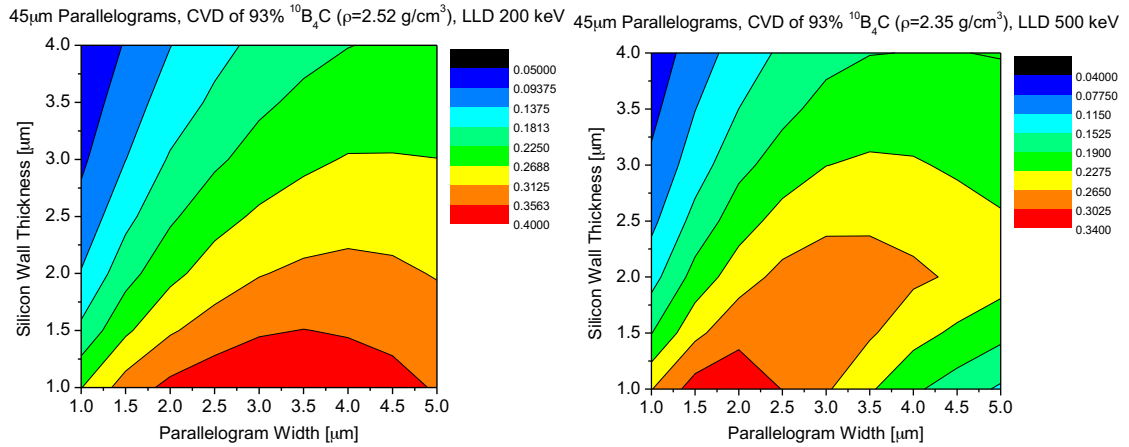


Figure A.5: Contour plot showing the simulated thermal neutron efficiency as a function of the parallelogram width and silicon wall thickness of a 45 μm-deep parallelogram device filled via CVD of B_4C ($\rho=2.52 \text{ g/cm}^3$) and an LLD of 200 keV (left) and 500 keV (right).

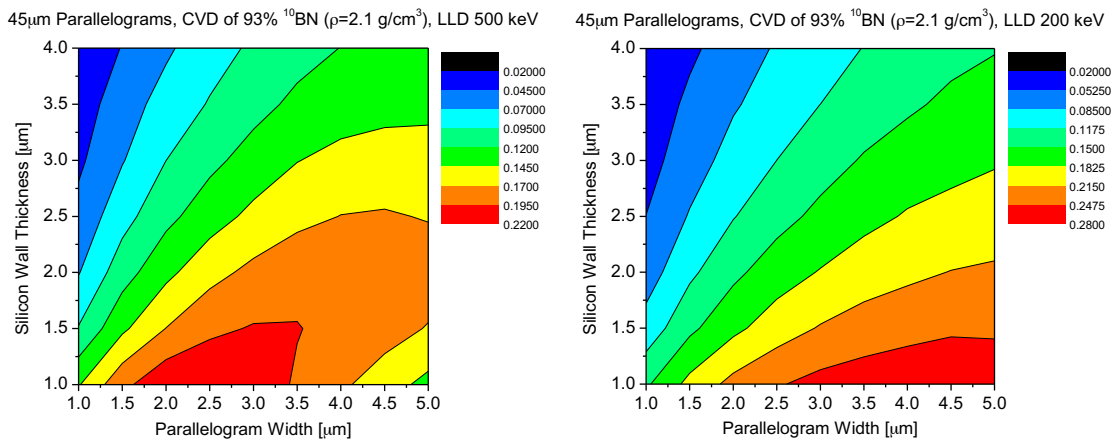


Figure A.6: Contour plot showing the simulated thermal neutron efficiency as a function of the parallelogram width and silicon wall thickness of a 45 μm-deep parallelogram device filled via CVD of BN ($\rho=2.1 \text{ g/cm}^3$) and an LLD of 200 keV (left) and 500 keV (right).

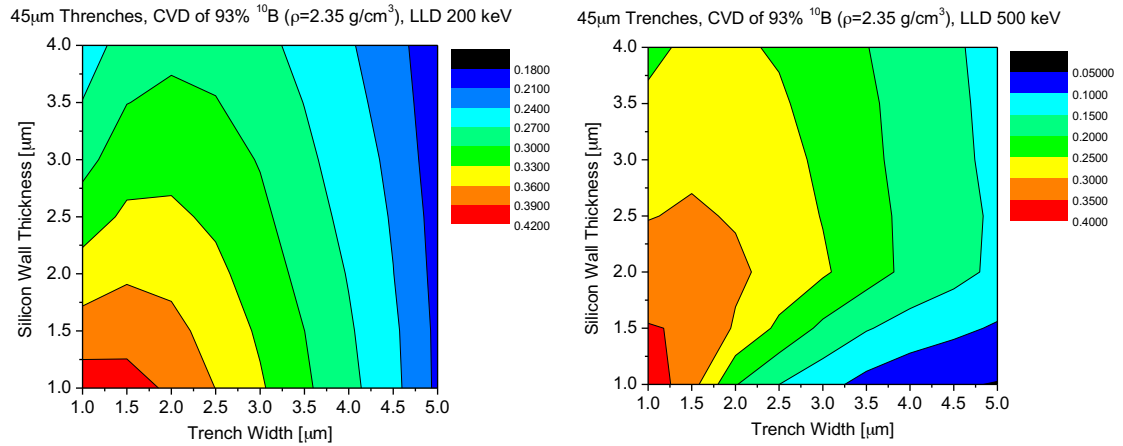


Figure A.7: Contour plot showing the simulated thermal neutron efficiency as a function of the trench width and silicon wall thickness of a 45 μm-deep trench device filled via CVD of boron ($\rho=2.35 \text{ g/cm}^3$) and an LLD of 200 keV (left) and 500 keV (right).

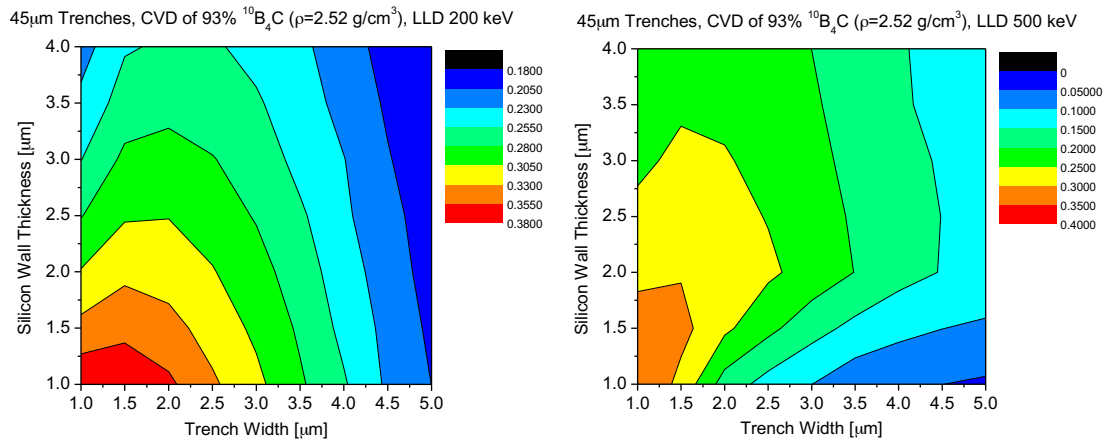


Figure A.8: Contour plot showing the simulated thermal neutron efficiency as a function of the trench width and silicon wall thickness of a 45 μm-deep trench device filled via CVD of B_4C ($\rho=2.52 \text{ g/cm}^3$) and an LLD of 200 keV (left) and 500 keV (right).

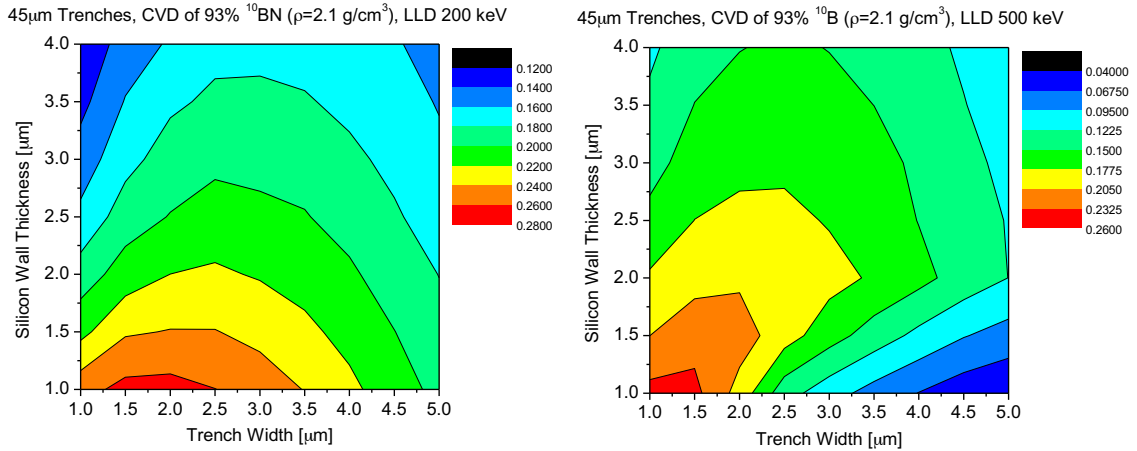


Figure A.9: Contour plot showing the simulated thermal neutron efficiency as a function of the trench width and silicon wall thickness of a 45 μm -deep trench device filled via CVD of BN ($\rho=2.1 \text{ g/cm}^3$) and an LLD of 200 keV (left) and 500 keV (right).

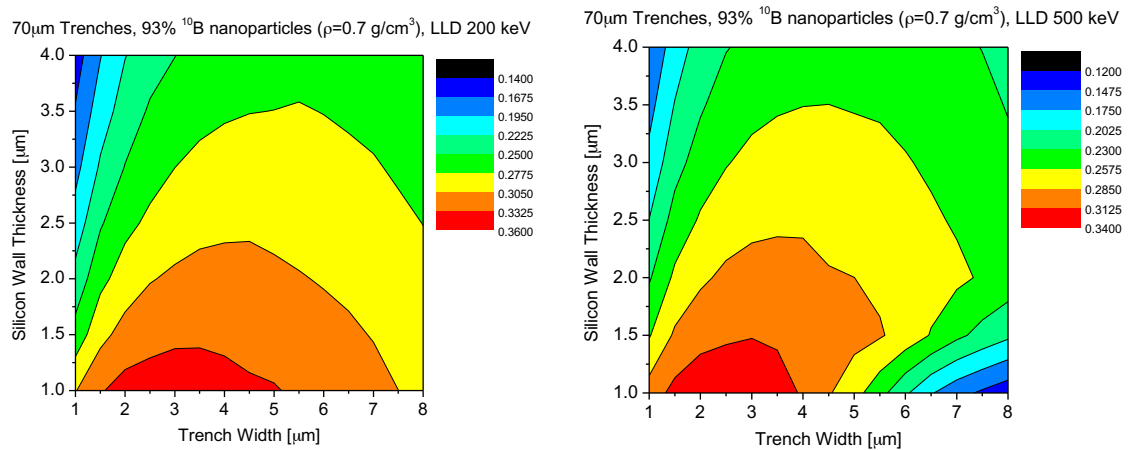


Figure A.10: Contour plot showing the simulated thermal neutron efficiency as a function of the trench width and silicon wall thickness of a 70 μm -deep trench device filled with boron nanoparticles ($\rho=0.7 \text{ g/cm}^3$) and an LLD of 200 keV (left) and 500 keV (right).

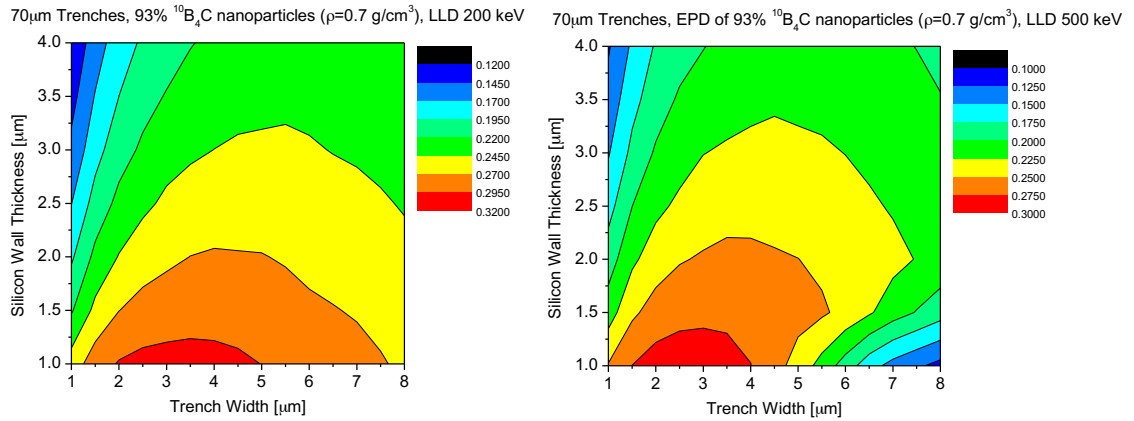


Figure A.11: Contour plot showing the simulated thermal neutron efficiency as a function of the trench width and silicon wall thickness of a 70 μm -deep trench device filled with B_4C nanoparticles ($\rho=0.7\text{ g/cm}^3$) and an LLD of 200 keV (left) and 500 keV (right).

Appendix B: Examples of MCNP6 inputs used to determine the optimal device microstructure corresponding to various neutron converting materials, discrimination levels (LLDs), and device depths.

Hexagonal structure, 45um deep, boron converter (2.35 g/cm³), LLD 200 keV

```

1 0 -1 fill=1
2 0 -2 u=1 lat=2 fill=2
3 3 -2.35 -3 5 u=2
4 4 -2.329 3 u=2
5 0 -5 u=2
99 0 4
100 2 -0.00001 -4 1 #90
90 0 90 -91 92 -93 94 -95

1 box 0 0 0 0.2 0 0 0 0.2 0 0 0 0.0045 $etched surface
2 rhp 0 0 0 0 0 0.0045 0.000179903810567666 0 0
3 rhp 0 0 0 0 0 0.0045 0.000129903810567666 0 0
4 so 1
5 c/z 0 0 5.28308861658862E-05
90 px 0
91 px .2
92 py 0
93 py .2
94 pz 0.0046
95 pz 0.0047

```

c ***** BLOCK M: MATERIAL CARDS *****

```

M1 1001.72c 4 6000.72c 2
M2 $Air
    6000.72c -0.000122 $C
    8016.72c -241123 $O
    7014.72c -.744518 $N
    1001.72c -0.001290 $H
M3 $B-10
    5010.72c 0.93
    5011.72c 0.07
M4 $Silicon
    14000 1
M10 $B4C
    5010 3.72
    5011 0.28
    6000 1
    nlib=70c

```

c ***** BLOCK 3: DATA CARDS *****

```

MODE N P a #
DBCN 8j 1e-7

```

```
PHYS:N 100 0 0 j j j 3 -1
PHYS:a 100 3j 0 5j 3j 0.917
PHYS:# 100 3j 0 5j 3j 0.917
CUT:N 10e9 0.009e-6
CUT:a j 0.000001
CUT:P j 0.001
CUT:E j 0.000001
CUT:# j 0.000001
print -128 100
NPS 3e4
IMP:N,P,a,# 1 4r 0 1 1
c
c
sdef POS=0.1 0.1 0.04 ERG=2.53e-8
c
c
c Tallies
FC18 Energy Deposition Tally in Si - Alphas and Lithium
F18:a# 4
E18 0.2 10
c
F4:n 90
```

c

Parallelogram structure, 45um deep, B₄C converter (2.52 g/cm³), LLD 200 keV

```
c
99 0 3      $Void
2  3 -0.0001 -3 #8 #90  $Air
3  10 -2.52 4 -5 6 -7 #55 u=10  $Boron Parallelogram
4  2 -2.329 -4:5:-6:7 u=10  $Silicon Around Boron
55 0 -55 u=10
c
5  0 4 -15 6 -8 lat=1 u=11 fill=-499:0 -499:0 0:0 10 249999r
8  0 24 -25 16 -17 18 -19 fill=11
90 0 90 -91 92 -93 94 -95
```

c Surface Cards

```
3  SO  2.5  $Outside of Problem
4  P 1 -0.334 0 0  $Boron, Si Parallelogram left
5  P 1 -0.334 0 0.0003 $Boron Parallelogram right wall
6  PY 0          $Boron, Si Parallelogram bottom wall
7  PY 0.0003      $Boron Parallelogram top wall
8  PY 0.0004      $Si top
15 P 1 -0.334 0 0.0004  $Si right wall
16 PY 0          $Lattice Area y1
17 PY 0.2
18 PZ 0
19 PZ 0.0045
24 P 1 -0.334 0 0
25 P 1 -0.334 0 0.2
55 c/z 0.000200071028885066 0.000141396223663827 6.55529058355247E-05
90 py 0
91 py 0.2
92 p 1 -0.334 0 0
93 p 1 -0.334 0 0.2
94 pz 0.0046
95 pz 0.0047
```

c Material Specifications

c Boron

```
M1  5010      0.93
    5011      0.07
```

c

c Silicon

```
M2  14000     1
```

c Air

```
M3  6000      0.000125
    7014      0.6869
    8016      0.301248
```

```

18000 0.011717
nlib=70c
M10 $B4C
5010 3.72
5011 0.28
6000 1
nlib=70c
M11 $BN
5010 0.93
5011 0.07
7000 1
nlib=70c
c
c Source Specification etc.
c
MODE N P a #
DBCN 8j 1e-5
PHYS:N 100 0 0 j j j 3 -1
PHYS:a 100 3j 0 5j 3j 0.917
PHYS:# 100 3j 0 5j 3j 0.917
CUT:a j 0.000001
CUT:P j 0.001
CUT:E j 0.000001
CUT:# j 0.000001
nps 1e5
print -128 100
c
IMP:N,P,a,# 0 1 6r
c
c
sdef POS=0.1 0.1 0.04 ERG=2.53e-8
c Tallies
FC18 Energy Deposition Tally in Si - Alphas and Lithium
F18:a# 4
E18 0.2 10
c
F4:n 90
C

```

Trench, 70um deep, Boron nanoparticle converter (0.7 g/cm³), LLD 200 keV

c
99 0 3 \$Void
1 2 -2.329 -1 #8 \$Silicon Box on bottom
2 3 -0.0001 -3 #8 #1 \$Air
3 1 -0.7 4 -5 6 -7 u=10 \$Boron Trench
4 2 -2.329 -4:5:-6:7 u=10 \$Silicon Around Boron
c
5 0 14 -15 6 -8 lat=1 u=11 fill=0:0 -570:0 0:0 10 570r
8 0 14 -15 16 -17 18 -19 fill=11

c Surface Cards

1 BOX 0 0 -0.0002 0.20 0 0 0 0.2 0 0 0 0.0073 \$Silicon Box
3 SO 2.5 \$Outside of Problem
4 PX 0 \$Boron Trench
5 PX 0.2000 \$Boron Trench
6 PY 0 \$Boron Trench

c
7 PY 0.00025
8 PY 0.00035
14 PX 0 \$Lattice Area x1
15 PX 0.2000
16 PY 0 \$Lattice Area y1
17 PY 0.19985
18 PZ 0
19 PZ 0.0070

c Material Specifications

c Boron Carbide

M1 5010 0.93
5011 0.07

c

c Silicon

M2 14000 1

c Air

M3 6000 0.000125
7014 0.6869
8016 0.301248
18000 0.011717
nlib=70c

M10 \$B4C

5010 3.72
5011 0.28
6000 1
nlib=70c

```

M11 $BN
    5010 0.93
    5011 0.07
    7000 1
    nlib=70c
c
c Source Specification etc.
c
MODE N P a #
DBCN 8j 1e-6
PHYS:N 100 0 0 j j j 3 -1
PHYS:a 100 3j 0 5j 3j 0.917
PHYS:# 100 3j 0 5j 3j 0.917
CUT:a j 0.000001
CUT:P j 0.001
CUT:E j 0.000001
CUT:# j 0.000001
nps 2e5
print -128 100
c
IMP:N,P,a,# 0 1 5r
c
c
sdef POS=0.1 0.1 0.04 ERG=2.53e-8 $Thermal neutron source above the detector
c
c Tallies
FC18 Energy Deposition Tally in Si - Alphas and Lithium
F18:a# 4
E18 0.2 3
c
F2:n 1.5
C

```

Appendix C: Example of an MCNP6 input used to simulate the pulse height spectrum of a 45 μ m-deep honeycomb device ($D_H=3 \mu$ m, $W_w=1 \mu$ m) with 100 evenly-spaced energy bins.

45um-Deep HoneyComb (85% fill) Device-Pulse Height Spectrum

```

1 0 -1 fill=1
2 0 -2 u=1 lat=2 fill=2
3 3 -2.35 -3 5 u=2
4 4 -2.329 3 u=2
5 0 -5 u=2
99 0 4
100 2 -0.00001 -4 1

1 box 0 0 0 0.2 0 0 0 0.2 0 0 0 0.0045 $etched surface
2 rhp 0 0 0 0 0 0.005 0.0002 0 0 $Unit cell of boron surrounded by Si
3 rhp 0 0 0 0 0 0.005 0.00015 0 0 $Single boron-filled hexagonal hole
4 so 1
5 c/z 0 0 5.28308861658862E-05 $Cylindrical hole to model 85% fill factor

```

c ***** BLOCK M: MATERIAL CARDS *****

```

M1 1001.72c 4 6000.72c 2
M2 $Air
    6000.72c -0.000122 $C
    8016.72c -241123 $O
    7014.72c -.744518 $N
    1001.72c -0.001290 $H
M3 $B-10
    5010.72c -0.93 5011.72c -0.07
M4 $Silicon
    14000 1
M10 $B4C
    5010 3.72
    5011 0.28
    6000 1
    nlib=70c

```

c ***** BLOCK 3: DATA CARDS *****

```

MODE N P a #
DBCN 8j 1e-5
PHYS:N 100 0 0 j j j 3 -1
PHYS:a 100 3j 0 5j 3j 0.917
PHYS:# 100 3j 0 5j 3j 0.917
c CUT:N 10e9 0.009e-6
CUT:a j 0.000001
CUT:P j 0.001
CUT:E j 0.000001

```

```
CUT:# j 0.000001
print -128 100
NPS 5e7
IMP:N,P,a,# 1 4r 0 1
sdef x=d2 y=d3 z=0.04 ERG=d1
sp1 -5 0.033e-6
SI2 0 0.2
SP2 0 1
SI3 0 0.2
SP3 0 1
c Tallies
FC18 Energy Deposition Tally in Si - Alphas and Lithium
F18:a# 4          $Pulse Height Tally
E18 0.05 99i 3.5  $100 evenly-spaced energy bins
F2:n 1.5          $Flux Tally
```

Appendix D: Example of an MCNP6 input used to simulate the pulse height spectrum of a 70 μ m-deep trench device ($W_T=5\ \mu$ m, $W_w=3\ \mu$ m) with 100 evenly-spaced energy bins.

70um-Deep Trench (0.7 g/cm3) Device-Pulse Height Spectrum

```

c
99  0 3      $Void
1   2 -2.329 -1 #8 $Silicon Box on bottom
2   3 -0.0001 -3 #8 #1 $Air
3   1 -0.7 4 -5 6 -7 u=10 $Boron Trench
4   2 -2.329 -4:5:-6:7 u=10 $Silicon Around Boron
c
5   0 14 -15 6 -8 lat=1 u=11 fill=0:0 -249:0 0:0 10 249r
8   0 14 -15 16 -17 18 -19 fill=11

c Surface Cards
1   BOX 0 0 -0.0002 0.20 0 0 0 0.2 0 0 0 0.0120 $Silicon Box
3   SO 2.5      $Outside of Problem
4   PX 0        $Boron Trench
5   PX 0.2000   $Boron Trench
6   PY 0        $Boron Trench
c
7   PY 0.0005
8   PY 0.0008
14  PX 0        $Lattice Area x1
15  PX 0.2000
16  PY 0        $Lattice Area y1
17  PY 0.2
18  PZ 0
19  PZ 0.0070

c Material Specifications
c Boron Carbide
M1  5010      0.93
    5011      0.07
c
c Silicon
M2  14000     1
c Air
M3  6000      0.000125
    7014      0.6869
    8016      0.301248
    18000     0.011717
    nlib=70c
M10 $B4C

```

```

5010 3.72
5011 0.28
6000 1
nlib=70c
M11 $BN
5010 0.93
5011 0.07
7000 1
nlib=70c
c
c Source Specification etc.
c
MODE N P a #
DBCN 8j 1e-6
PHYS:N 100 0 0 j j j 3 -1
PHYS:a 100 3j 0 5j 3j 0.917
PHYS:# 100 3j 0 5j 3j 0.917
CUT:a j 0.000001
CUT:P j 0.001
CUT:E j 0.000001
CUT:# j 0.000001
nps 5e7
print -128 100
c
IMP:N,P,a,# 0 1 5r
c
sdef x=d2 y=d3 z=0.04 ERG=d1
sp1 -5 0.033e-6
SI2 0 0.2
SP2 0 1
SI3 0 0.2
SP3 0 1
c
c Tallies
FC18 Energy Deposition Tally in Si - Alphas and Lithium
F18:a# 4
E18 0.05 99i 3.5
c
F2:n 1.5
C

```

Appendix E: Individual MCNP inputs and factors used to create the simulated pulse height spectrum in Figure 3.12.

Table E1: Individual MCNP inputs and the corresponding factors used to build an MCNP simulation to model the complex geometry of a honeycomb microstructured device.

Honeycomb Diameter [μm]	Si Wall Thickness [μm]	Fill Factor [%]	Factor
3	1	100	8.9×10^{-5}
3	1	85	0.119
3	1	70	0.019
3	1	55	0.056
3	1	40	0.034
2.75	1.25	100	0.128
2.75	1.25	85	0.024
2.75	1.25	70	0.114
2.75	1.25	55	0.031
2.75	1.25	40	0.022
2.5	1.5	100	0.026
2.5	1.5	85	0.024
2.5	1.5	70	0.039
2.5	1.5	55	0.052
2.5	1.5	40	0.040
2.25	1.75	100	0
2.25	1.75	85	0.06
2.25	1.75	70	0.027
2.25	1.75	55	0.045
2.25	1.75	40	0.021
2	2	100	0
2	2	85	0.006

2	2	70	0.003
2	2	55	0.022
2	2	40	0.038
1.5	2.5	100	0.072
1.5	2.5	85	0.066
1.5	2.5	70	0.017
1.5	2.5	55	0.003
1.5	2.5	40	0.024